MIT/WHOI

Massachusetts Institute of Technology
Woods Hole Oceanographic Institution

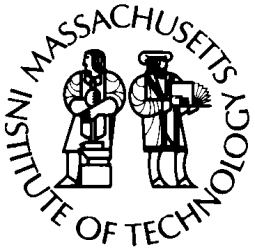

Joint Program in Oceanography/ Applied Ocean Science and Engineering

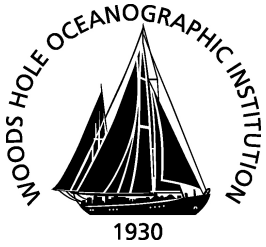

DOCTORAL DISSERTATION

Equatorial Ocean Dynamics Impacting Upwelling West of the Galápagos Archipelago

by

Julie K. Jakoboski

September 2019

Equatorial Ocean Dynamics Impacting Upwelling West of the Galápagos Archipelago

by

Julie K. Jakoboski
B.S.M.E., Bucknell University (2007)
B.A., Bucknell University (2007)

Submitted to the Joint Program in Physical Oceanography
in partial fulfillment of the requirements for the degree of
Doctor of Philosophy
at the
MASSACHUSETTS INSTITUTE OF TECHNOLOGY
and the
WOODS HOLE OCEANOGRAPHIC INSTITUTION
September 2019

Author .....
Joint Program in Physical Oceanography
Massachusetts Institute of Technology
& Woods Hole Oceanographic Institution
August 16, 2019

Certified by .....
Dr. W. Brechner Owens
Emeritus Research Scholar, Woods Hole Oceanographic Institution
Thesis Supervisor

Certified by .....
Dr. Robert E. Todd
Associate Scientist, Woods Hole Oceanographic Institution
Thesis Supervisor

Certified by .....
Prof. Kristopher B. Karnauskas
Associate Professor, University of Colorado - Boulder
Thesis Supervisor

Accepted by .....
Prof. Glenn R. Flierl
Chair, Joint Committee for Physical Oceanography
Massachusetts Institute of Technology & Woods Hole Oceanographic Institution

Equatorial Ocean Dynamics Impacting Upwelling West of the Galápagos Archipelago

by Julie K. Jakoboski

Submitted to the Massachusetts Institute of Technology & Woods Hole Oceanographic Institution on August 16, 2019, in partial fulfillment of the requirements for the degree of Doctor of Philosophy

Abstract

The Galápagos Cold Pool (GCP) is a region of anomalously cold sea surface temperature (SST) just west of the Galápagos Archipelago. Modeling studies have shown that the GCP is maintained by wind- and current-driven upwelling. The Galápagos Archipelago lies on the equator, in the path of the Pacific Equatorial Undercurrent (EUC) as it flows eastward across the Pacific at the depth of the thermocline. It is hypothesized that the EUC upwells into the GCP as it reaches the topographical barrier of the Galápagos Archipelago. The path of the EUC in the vicinity of the archipelago is not well understood. The 'Repeat Observations by Gliders in the Equatorial Region' (ROGER) program deployed a fleet of Spray autonomous underwater gliders in the region just west of the Galápagos Archipelago from 2013 – 2016 with the goal of continuously occupying three transects that form a closed area, with the archipelago as the eastern boundary. Gliders obtained subsurface measurements of temperature, salinity, and velocity with unprecedented temporal and spatial resolution. These measurements are used to observe the path of the EUC as it bifurcates into a north and south branch around the Galápagos Archipelago. Net horizontal transport into the volume defined by the closed area formed by the glider transects is used to estimate an average vertical velocity profile in the region of the GCP, indicating upwelling in the upper 300 m. The bifurcation latitude of the EUC, estimated to be approximately 0.4°S from volume transport as a function of salinity, is coincident with the meridional center of the archipelago, suggesting the bifurcation latitude is topographically controlled. Ertel potential vorticity and a Bernoulli function are qualitatively conserved, supporting an inertial model of the EUC. Average spectral variance from Argo profiling float observations is used to show that tropical instability waves propagate with frequency and wavelength consistent with linearized, equatorial β-plane model results and may impact the GCP, according to their vertical structure.

Thesis Supervisor: Dr. W. Brechner Owens
Title: Emeritus Research Scholar, Woods Hole Oceanographic Institution

Thesis Supervisor: Dr. Robert E. Todd
Title: Associate Scientist, Woods Hole Oceanographic Institution

Thesis Supervisor: Prof. Kristopher B. Karnauskas
Title: Associate Professor, University of Colorado - Boulder

Acknowledgments

None of this would have an inkling of being possible without an incredible group of people. The MIT/WHOI Joint Program is far more than I could have imagined. Every day that I enter either institution I am thankful to be a part of it. One of the most incredible things about the Joint Program is the community that exists here. I would like to thank the faculty and staff that support the Joint Program for being a key reason this graduate experience is possible for any of us. My professors and instructors took the time to share their knowledge with us, open their doors to us, and treat us as colleagues. Thank you to the administrators who support all our (nearly always) last minute requests - your help is truly appreciated. Thank you to the physical oceanography students in my year for helping me review math after a six year hiatus and offering encouragement throughout our time in the program. I will forever value you, and the rest of the students I've met in the Joint Program, as friends and colleagues. This would absolutely not have been possible for me without you all. Thank you to my thesis committee: Glenn Flierl, Tom Farrar, and Dan Rudnick, and the chair of my thesis defense, Susan Wijffels, for your expertise, insight, guidance, and suggestions. Also thank you to Dan Rudnick for your work on the ROGER program (with the rest of the ROGER team), and for allowing me to spend time working at the Scripps Institution of Oceanography for three winters during my studies. And of course, thank you to my advisors: Breck Owens, Robert Todd, and Kristopher Karnauskas. Your experience, knowledge, and understanding are second to none. I don't know how articulate how meaningful this experience was to me, largely shaped by your influences. I will always be grateful for your willingness to work with my sometimes non-traditional approach to my graduate studies and your ability to help me grow into a scientist who deeply loves oceanography. My graduate studies in the Joint Program were truly an incredible experience.

Outside of the academic realm, I would like to thank my friends "from before grad school" who ran with me in the mountains, inspired and encouraged me, and gave me academic and personal advice. You had more of an impact than you realize. Thank you to the New Hampshire surf and swimming communities for your support along the way. Thank you to my friends (east and west coast), surf and swim partners, and to the ocean itself for providing a place to step away from thesis writing when I needed it. Thank you to the Evans family for giving me a place to study, write, eat and sleep. Mikel Evans gets an unofficial award for his constant support: for making the best breakfast sandwiches that I can take on the train or in the car with me as I dash into the house for a half a second between a surf session and rushing to school, for reminding me to be confident and positive, and for everything else.

Thank you to my extended family for making me who I am. To Dad, Mom, and Derek: some things are too big for words, but thank you. You know you are there every step of the way, between steps, and more. Now, onto the next adventure!

Funding for my thesis research was provided by the National Science Foundation (grants OCE-1232971 and OCE-1233282), the NASA Earth and Space Science Fellowship Program (grant 80NSSC17K0443), the J. Seward Johnson Fund, and the Karen L. Von Damm Fellowship.

THIS PAGE INTENTIONALLY LEFT BLANK

Contents

List of Figures

THIS PAGE INTENTIONALLY LEFT BLANK

List of Tables

THIS PAGE INTENTIONALLY LEFT BLANK

Introduction

The Galápagos Cold Pool (GCP) is a region of anomalously cold sea surface temperature (SST) that exists just west of the Galápagos Archipelago (Figure 0-1). The GCP supports the unique ecosystem of the Galápagos Archipelago by bringing high-nutrient, upwelled waters to the surface where it supports a wide-range of endemic species (e.g., *Karnauskas et al.*, 2015). This region of cool SST reaches 300-500 km westward from the west coast of Isla Isabela (91°W) and extends along the meridional extent of the archipelago. The GCP exists due to wind- and current-driven upwelling (*Palacios*, 2004; *Sweet et al.*, 2007). *Houvenaghel* (1978) showed that the GCP is maintained even during periods of light and variable winds, indicating that additional sources of upwelling must exist, such as upwelling of the Pacific Equatorial Undercurrent (EUC).

The EUC is a coherent, eastward flow with a maximum speed near 1 m s^{-1} first documented by *Cromwell et al.* (1954). It originates in the western Pacific at a depth of 200 m and shoals to a depth of 50 m as it arrives at the Galápagos Archipelago in the eastern Pacific (*Johnson et al.*, 2002). The EUC is the result of the zonal momentum balance across the equatorial Pacific, driven by the depth-integrated zonal pressure gradient that results from easterly trade winds (e.g., *Charney*, 1959; *Charney and Spiegel*, 1971; *Pedlosky*, 1987a; *Johnson and Luther*, 1994; *Qiao and Weisberg*, 1996). The average position of the EUC core is near 0.2°S and 50 m depth and extends meridionally beween about 2°S-1°N and vertically from the surface to 200 m (*Qiao and Weisberg*, 1996; *Johnson et al.*, 2002).

The Galápagos Archipelago lies on the equator in the eastern equatorial Pacific Ocean, directly in the path of the EUC (Figure 0-2). As the EUC reaches the topographic boundary of the Galápagos Archipelago, upwelling in the region of the GCP may result, as suggested by the modeling results of *Liu et al.* (2014). Potential upwelling of the EUC is dependent on the path of the EUC with respect to the Galápagos Archipelago (*Houvenaghel*, 1978;

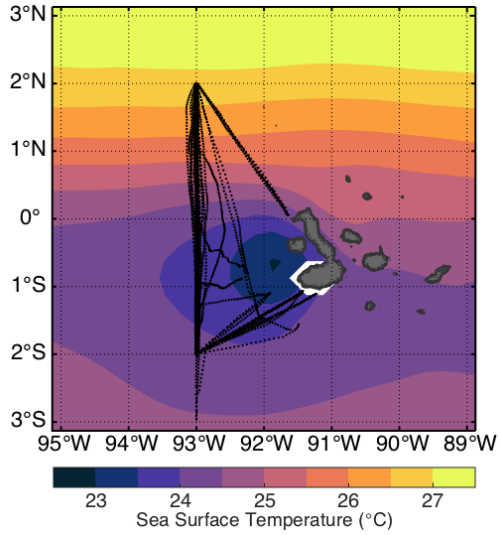

Figure 0-1: Average sea surface temperature (SST) in the the region around the Galápagos Archipelago during 2013–2016 and individual profiles from Spray glider missions west of the Galápagos Archipelago obtained during the ROGER program (black dots). Daily SST data are from the Group for High Resolution Sea Surface Temperature (GHRSST) at $1/4° \times 1/4°$ horizontal resolution (*Reynolds et al.*, 2007; *National Centers for Environmental Information*, 2016).

Liu et al., 2014); however, the fate of the EUC when it reaches the Galápagos Archipelago is largely unknown. Previous observations of the EUC as it reaches the archipelago have been limited to relatively sparse shipboard observations of velocity, temperature, salinity, and pressure (e.g., *Knauss*, 1966; *Lukas*, 1986).

The equatorial current system, including the EUC, South Equatorial Current (SEC), and North Equatorial Countercurrent (NECC), result in regions of high vertical and horizontal shear. This shear results in barotropic and baroclinic instabilities that generate westward propagating Tropical Instability waves (TIWs) (e.g., *Philander*, 1976, 1978; *Johnson and Proehl*, 2004; *Qiao and Weisberg*, 1995). *Lyman et al.* (2005) showed that TIWs can be described as a resonance between two Rossby waves using a linearized model of the central Pacific Ocean. TIWs have been observed across the equatorial Pacific with periods between 15 and 50 days and wavelengths of 700–1300 km (e.g., *Wunsch and Gill*, 1976; *Périgaud*, 1990; *Farrar and Weller*, 2006; *Lyman et al.*, 2007; *Lee et al.*, 2012), including near the region of the GCP (*Harvey and Patzert*, 1976). Due to their proximity to the Galápagos Archipelago, TIWs have the potential to impact the GCP directly or through interaction with the EUC or SEC.

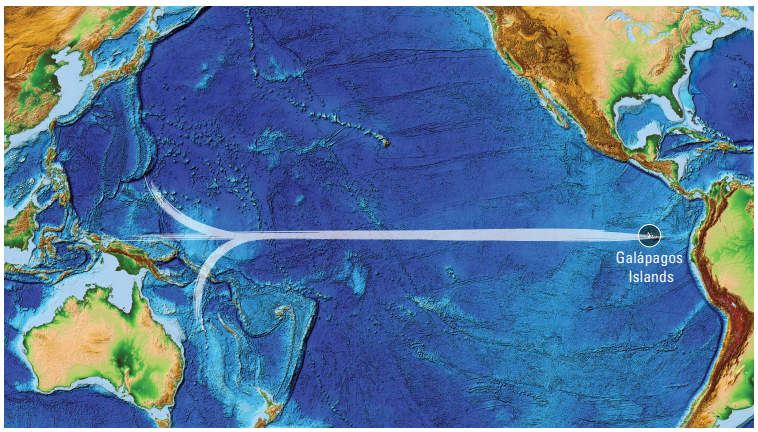

Figure 0-2: Schematic of the EUC (white) originating in the western Pacific Ocean and arriving at the Galápagos Archipelago. Credit: Eric S. Taylor, WHOI Creative Studio

The 'Repeat Observations by Gliders in the Equatorial Region' (ROGER) program deployed a fleet of Spray autonomous underwater gliders (*Sherman et al.*, 2001; *Rudnick et al.*, 2016) along three survey lines just west of the Galápagos Archipelago between 2013 and 2016. One of the primary goals of the ROGER program was to better observe and understand the fate of the EUC in this region. These gliders provided unprecedented, high resolution O(5 km) observations of temperature, salinity, and absolute velocity as a function of pressure to a depth of 1000 m. Absolute velocity measurements were obtained using small acoustic Doppler current profilers (ADCPs), mounted on the gliders, that can be combined with the depth averaged velocity obtained from positions at the start and end of a dive(*Todd et al.*, 2017). Observations of subsurface current velocity eliminate the need for estimating geostrophic velocity from density observations, which is particularly important at the equator where geostrophy does not apply due to vanishing of the Coriolis parameter. Three glider tracks were designed to observe the path of the EUC and encompass the GCP, based on the modeling results of *Karnauskas et al.* (2010). Together with the eastern boundary of Isla Isabela, they form a closed horizontal area (Figure 0-1). These unprecedented, simultaneous measurements of subsurface current velocity, temperature, and salinity allows us to estimate volume transport, area-averaged vertical velocity, volume transport as a function of salinity, and Ertel potential vorticity in the region between 93°W and the Galápagos Archipelago over timescales ranging from two months to three years.

The Argo program (*Riser et al.*, 2016) provides global measurements of subsurface temperature and salinity by deploying autonomous profiling floats worldwide. Argo floats pas-

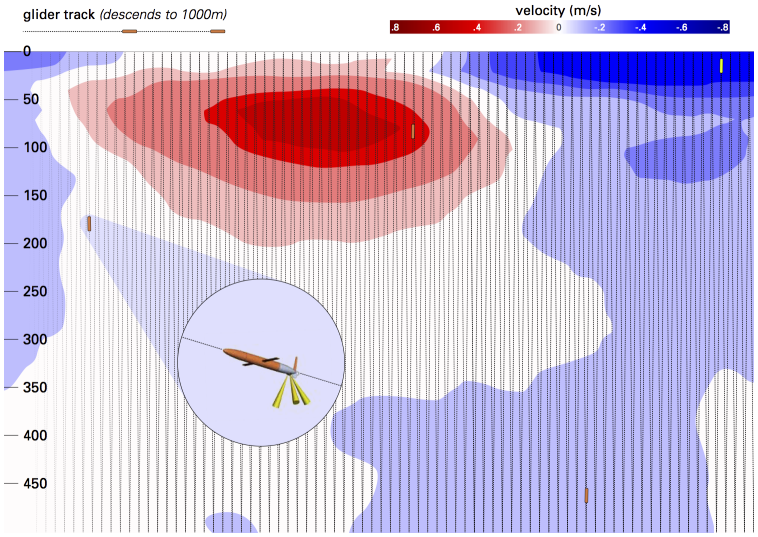

Figure 0-3: Schematic of a Spray glider completing a latitude-depth transect measuring zonal velocity from 2°N to 2°S latitude along 93°W longitude, where depth is in meters and the length of the transect is approximately 440 km. Red is eastward velocity. Credit: Eric S. Taylor, WHOI Creative Studio

sively drift through the ocean at a designed parking depth of 1000 m for ten days, descend to 2000 m, and then profile from 2000 m to the surface. Argo data is available since the year 2000 with floats added to the global array every year. The equatorial Pacific retains coverage due to an increased effort to deploy floats in the region (*Gasparin et al.*, 2015).

This thesis addresses the following primary questions:

- What is the fate of the EUC as it reaches the Galápagos Archipelago?
- What mechanisms contribute to the existence of the persistent, anomalously cold SST of the GCP?
- What can high resolution observations tell us about the potential vorticity field associated with the equatorial current system in the region of the GCP? Are conditions in this region conducive to instability?
- What is the observed three-dimensional structure of TIWs across the equatorial Pacific?

In Chapter 1, we examine the bifurcation of the EUC into a north and south branch around the Galápagos Archipelago using high resolution, subsurface glider measurements of current velocity, temperature, and salinity. The branches of the EUC transport nearly

all of the total EUC volume around the archipelago, while a small fraction of EUC water upwells into the GCP. Volume transport as a function of salinity class provides an estimate of the bifurcation latitude of the EUC and quantifies the hydrographic properties of the two branches in comparison with the incoming EUC. Volume transport from glider observations along each line is estimated and summed to find the net volume transport into the volume defined by the glider tracks. We then estimate an average vertical velocity profile over the closed area defined by the three glider lines and Isla Isabela from integrating the net horizontal transport profile estimate. The vertical velocity profile and horizontal volume transport estimates provide insight into the mechanisms maintaining the anomalously cold SST of the GCP. Net upwelling over the upper 300 m can not be explained by a slowing down of the EUC and is most likely due to a meridional divergence over the upper 300 m, which is consistent with observed meridional velocities along 93W.

Chapter 2 focuses on Ertel potential vorticity (*Ertel*, 1942; *Schubert et al.*, 2004) and a Bernoulli function (*Cushman-Roisin and Beckers*, 2011) associated with the average position of the EUC. Glider observations provide unprecedented, high-resolution estimates of the relative vorticity in this region. *Pedlosky* (1987a) showed that an inertial model of the equatorial region results in an eastward, EUC-like current on the equator, assuming EPV and the Bernoulli function are conserved along streamlines in the steady-state case. As Spray gliders are able to obtain velocity, temperature, and salinity measurements, we consider whether estimated sections of potential vorticity and the Bernoulli function are likely to be conserved in the real ocean.

In the absence of shear, the sign of Ertel potential vorticity is consistent with the sign of the Coriolis parameter on either side of the equator (*Gill*, 1982). *Stevens* (1983) showed that, in an equatorial β-plane model, it is possible to have Ertel potential vorticity with sign opposite to that of the Coriolis parameter in the region between the equator and a jet centered off the equator. This model approximately describes the EUC, which is centered near 0.5°S. Further, estimates of Ertel potential vorticity from glider measurements provide insight into the oceanic process that could result due to advection of EUC waters north and south of the Galápagos Archipelago as the EUC bifurcates into two branches. When Ertel potential vorticity has sign opposite to that of the Coriolis parameter, conditions may be conducive to inertial, symmetric, or gravitational instability (*Thomas et al.*, 2013). Glider observations are used to estimate possible e-folding timescales of such instabilities

and discuss possible limitations of these estimates.

To understand how TIWs may impact the GCP, we examine the three-dimensional signal of TIWs in Chapter 3. The surface expression of TIWs is well observed; however, the subsurface expression is less well known. If TIWs extend to the depth of the EUC or below, they may impact the GCP through modulation of the EUC or by inducing vertical velocity just west of the Galápagos Archipelago. A gridded Argo product from *Roemmich and Gilson* (2009) provides temperature and salinity observations across the equatorial Pacific to a depth of 2000 m. The resolution of the *Roemmich and Gilson* (2009) is sufficient to resolve TIWs with periods greater than 20 days. Chapter 3 estimates spectral variance of temperature, salinity, and potential density from Argo observations in the TIW band across the equatorial Pacific and between the surface and 200 m. It then compares three-dimensional spectral variance of temperature, salinity, and potential density to dispersion curves and meridional modes from a 1.5-layer, equatorial β-plane model linearized about a mean zonal velocity and to the results of *Lyman et al.* (2005). Vertical structure is compared to baroclinic vertical modes and the average stratification (N^2 profile).

Chapter 1

Bifurcation and Upwelling of the Equatorial Undercurrent West of the Galápagos Archipelago

A version of this work has been submitted to the Journal of Physical Oceanography for consideration for publication as: Jakoboski, J. K., Todd, R. E., Owens, W. B., Karnauskas, K. B., and Rudnick, D. L. *Bifurcation and Upwelling of the Equatorial Undercurrent West of the Galápagos Archipelago*

Abstract

The Equatorial Undercurrent (EUC) encounters the Galápagos Archipelago on the equator as it flows eastward across the Pacific. The impact of the Galápagos Archipelago on the EUC in the eastern equatorial Pacific remains largely unknown. In this study, the path of the EUC as it reaches the Galápagos Archipelago is measured directly using high-resolution observations obtained by autonomous underwater gliders. Gliders were deployed along three lines that define a closed region with the Galápagos Archipelago as the eastern boundary and 93°W from 2°S to 2°N as the western boundary. Twelve transects were simultaneously occupied along the three lines during 52 days in April – May 2016. Analysis of individual glider transects and average sections along each line show that the EUC splits around the Galápagos Archipelago. Average velocity normal to the transects is used to estimate net horizontal volume transport into the volume, which results in a net horizontal divergence within the volume. Downward integration of the net horizontal transport profile provides an estimate of the time-average, areal-average vertical velocity profile over the 52 day time period. Local maxima in vertical velocity occur at depths of 25 m and 280 m with magnitudes of $(1.7 \pm 0.6) \times 10^{-5}$ m s^{-1} and $(8.0 \pm 1.6) \times 10^{-5}$ m s^{-1}, respectively. Volume transport as a function of salinity indicates that water crossing 93°W south (north) of 0.4°S tends to flow around the south (north) side of the Galápagos Archipelago. Comparisons are made between previous observational and modeling studies with differences attributed to effects of the strong 2015 – 2016 El Niño event, the annual cycle of local winds, and varying longitudes

between studies of the equatorial Pacific.

1.1 Introduction

The Galápagos Archipelago lies on the equator in the path of the eastward flowing Pacific Equatorial Undercurrent (EUC). The Galápagos Cold Pool (GCP) is a region of nutrient-rich, anomalously cool sea surface temperature (SST; Figure 1-1) just west of the Galápagos Archipelago that is characterized by wind- and current-driven upwelling (*Palacios*, 2004; *Sweet et al.*, 2007). The GCP spans roughly the meridional extent of the Galápagos Archipelago and extends 300 – 500 km westward from Isla Isabela at 91°W (*Houvenaghel*, 1978). Sources of upwelling associated with the GCP and possible connections to the EUC are not well understood.

Three distinct processes cause upwelling in the vicinity of the Galápagos Archipelago. Eastward trade winds drive horizontally divergent surface flow in two ways: 1) Ekman divergence due to the change in sign of the Coriolis parameter at the equator; and 2) downwind transport in the lee of the islands, which we refer to as 'wind-driven coastal upwelling' despite differences from Ekman-driven coastal upwelling away from the equator. The third process can occur when a sub-surface current encounters a sloping bottom or coast, which we will call 'topographic upwelling'. *Houvenaghel* (1978) showed that upwelling associated with the GCP continues even when wind patterns are light and variable, suggesting that this is likely primarily topographic upwelling of the EUC as it reaches the Galápagos Archipelago. *Liu et al.* (2014) predicted the occurrence of both wind-driven and topographic upwelling of the EUC at the Galápagos Archipelago. *Karnauskas et al.* (2007) show that the GCP emerges without wind-topography interactions, indicating the presence of topographic upwelling.

Previously, equatorial upwelling and its connection to the EUC were examined using a box model from 170°E to 100°W by *Wyrtki* (1981) and using mooring observations at 140°W (*Weisberg and Qiao*, 2000) and 170° – 95°W (*Johnson et al.*, 2001). Vertical velocity profiles from *Weisberg and Qiao* (2000) and *Johnson et al.* (2001) show similar shape with upwelling (positive vertical velocity) above 150 m depth that is significantly different from zero above 50 m. However, it is expected that upwelling just west of Galápagos Archipelago differs from general equatorial Pacific upwelling due to the presence of the archipelago, as indicated by the presence of the GCP.

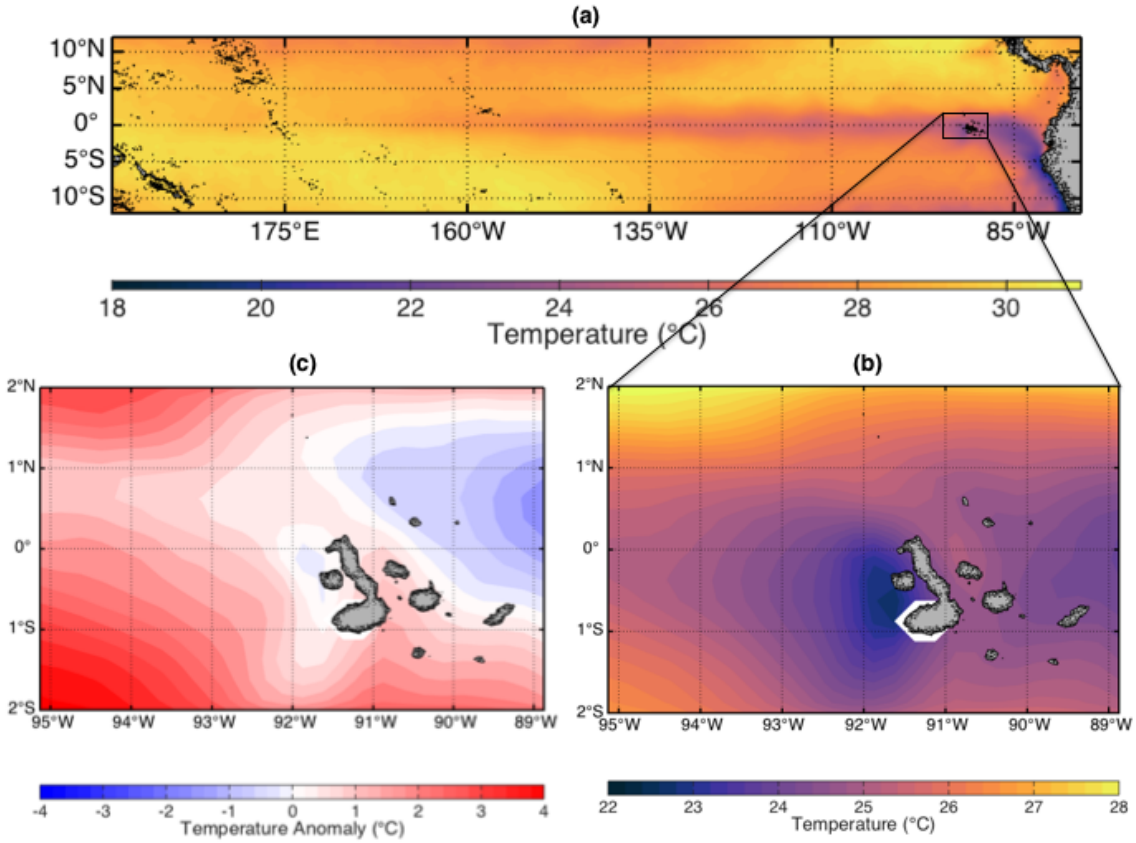

Figure 1-1: (a) SST in the equatorial Pacific during 6 April – 31 May 2016 with the region around the Galápagos Archipelago enlarged (b) to show the GCP. (c) SST anomalies during April – May 2016 relative to the 2004 – 2016 climatology. Daily SST data are from the Group for High Resolution Sea Surface Temperature (GHRSST) provided with $1/4° \times 1/4°$ horizontal resolution (*Reynolds et al.*, 2007; *National Centers for Environmental Information*, 2016).

The EUC is a relatively high velocity ($\sim$ 1 m s^{-1}), subsurface, coherent flow moving eastward along the equator at the depth of the thermocline. It was first documented by *Cromwell et al.* (1954) using taut-wire buoy observations. EUC dynamics can be described by a non-linear, inertial model driven by a depth-integrated zonal pressure gradient set up by a westward wind stress (e.g., *Charney*, 1959; *Charney and Spiegel*, 1971; *Pedlosky*, 1987a; *Johnson and Luther*, 1994; *Qiao and Weisberg*, 1996). The EUC core shoals, following the thermocline, from a maximum depth of about 150 m in the western Pacific to a minimum depth of approximately 50 m as it approaches the Galápagos Archipelago in the east (*Johnson et al.*, 2001). The observed EUC has an estimated meridional extent of about 2° of latitude centered near 0.5°S, and a vertical extent of 200 m (*Qiao and Weisberg*, 1996; *Johnson et al.*, 2002).

The strength of the EUC varies on a range of time scales. On seasonal scales, the EUC tends to be weaker from October through February, and stronger from April to August (*Wyrtki and Meyers*, 1977; *Johnson et al.*, 2002; *Karnauskas et al.*, 2010). During El Niño years, the EUC is significantly weakened (*Johnson et al.*, 2002), with the exception of the passage of Kelvin waves (*Roundy and Kiladis*, 2006). *Firing et al.* (1983) show that this weakening can lead to a near reversal of the EUC, analogous to the atmospheric weakening of the Walker circulation associated with El Niño events (*Bjerknes*, 1969; *Lau and Yang*, 2015). During strong El Niño events, trade winds tend to decrease or reverse, which in turn decreases the zonal pressure gradient at the equator that drives the EUC.

The EUC has been observed at the depth of the thermocline with a broadening of the thermocline at the location of the EUC core due to geostrophic behavior associated with relatively high zonal velocities (e.g., *Lukas*, 1986; *Johnson et al.*, 2002). These studies also show a high salinity tongue extending into the EUC core from the south at the depth of the thermocline. This high salinity water originates in the subtropcial South Pacific and is transported toward the equator by multiple pathways (e.g., *Knauss*, 1966; *Johnson and McPhaden*, 1999; *Liu et al.*, 2014).

Few studies have attempted to characterize the path of the EUC around the Galápagos Archipelago, and related details of the eastern equatorial Pacific circulation remain unclear (*Kessler*, 2006). Previous subsurface observations in the eastern equatorial Pacific consist mostly of relatively sparse shipboard ADCP data (e.g., *Karnauskas et al.*, 2010), since the TAO array (*Hayes et al.*, 1991) does not extend east of 95°W. *Lukas* (1986)

used hydrographic data to show that the high salinity tongue associated with the EUC remains intact east of the Galápagos Archipelago as far as 82°W. *Lukas* (1986) also estimated geostrophic flow from dynamic topography, finding that the EUC splits around the Galápagos Archipelago with eastward flowing branches north and south of the islands. In a regional model, *Karnauskas et al.* (2007) showed that SST across the Eastern Equatorial Pacific is influenced by the presence of the Galápagos Archipelago, which impacts the EUC and characteristics of ENSO events (*Karnauskas et al.*, 2008).

Here we use autonomous underwater glider observations from the 'Repeat Observations by Gliders in the Equatorial Region' (ROGER) program to diagnose the flow of the EUC around the Galápagos Archipelago and to estimate areal-averaged upwelling between 93°W and the Galápagos Archipelago for a two-month period during which the region was well sampled. Section 1.2 describes the ROGER program and the glider observations used here. Section 1.3 presents average velocity fields (Section 1.3.1), describes the characteristics of horizontal volume transport associated with the EUC (Section 1.3.2) and provides an estimated time average, areal-averaged vertical velocity profile (Section 1.3.3). Volume transport by salinity class is analyzed in Section 1.3.4 to determine the latitude along 93°W where a split of the EUC around the Galápagos Archipelago may occur. Section 1.4 summarizes the results, their implications, and potential for future study.

1.2 Observations and Methods

ROGER used a fleet of Spray gliders (*Sherman et al.*, 2001; *Rudnick et al.*, 2016) to observe the equatorial current system in the region west of the Galápagos Archipelago. From January 2013 through December 2016, a total of 19 glider missions surveyed along three lines bounding a region (hereafter referred to as A_{gl}) to the west of the Galápagos Archipelago (Figure 1-2a, dashed black lines). The fourth side of A_{gl} (Figure 1-2a, magenta line) consists of Isla Isabela, the largest of the Galápagos Islands. The three glider survey lines were: 1) the northern diagonal (hereafter referred to as ND), between the northwestern corner of Isla Isabela and 93°W, 2°N, 2) 93°W from 2°N to 2°S (referred to as 93W), and 3) the southern diagonal (SD), between 93°W, 2°S and the southwestern corner of Isla Isabela. The sampling pattern was designed to capture the path of the EUC as it approaches the Galápagos Archipelago, guided by the modeling results of *Karnauskas et al.* (2010).

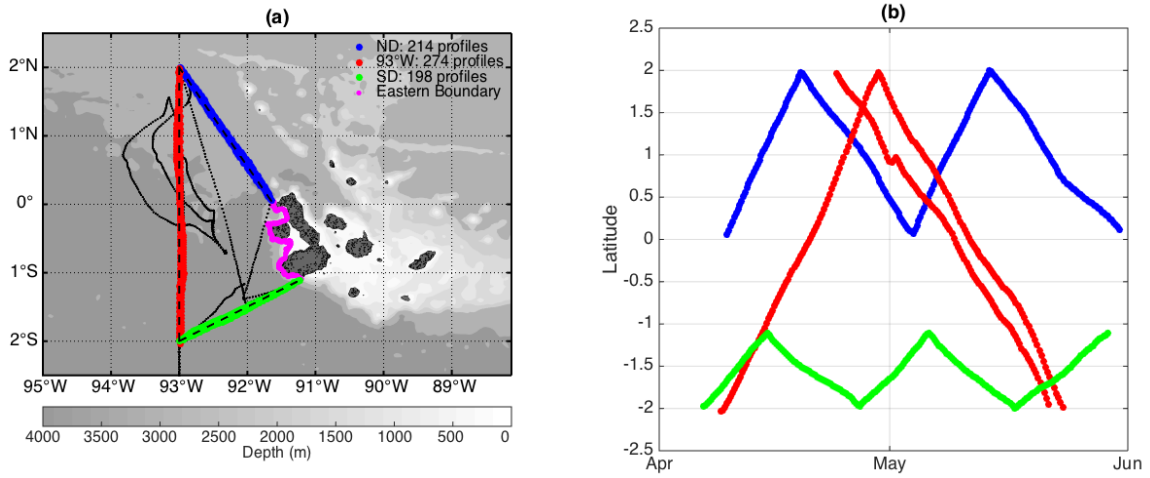

Figure 1-2: (a) Trajectories of Spray glider missions west of the Galápagos Archipelago that are included in the analysis. Individual profiles from transects within 30 km of ND (blue), 93W (red), and SD (green) are shown in color. Dashed black lines indicate the three lines that the gliders occupied, defining the area of interest (A_{gl}). The magenta line connecting the eastern endpoints of ND and SD is the 300 m depth contour used to calculate A_{gl}. The total number of profiles along each line is shown in the legend. (b) Sampling along ND (blue), 93W (red), and SD (blue) as a function of time and latitude.

For closure of transport calculations, all three survey lines need to be occupied simultaneously and only fully occupied lines can be used to calculate transport for each transect. This limits our analyses to the period between 6 April 2016 and 31 May 2016 during which time four gliders surveyed the region (Figure 1-2). Gliders were deployed from oceanographic research vessels of the Ecuadorian Instituto Oceanográfico de la Armada near the south coast of Isla Isabela on 30 March 2016. Two missions followed SD toward 93°W, subsequently occupying 93W. One mission each repeated transects along ND and SD. The four gliders were retrieved west of Isla Isabela on 20 July 2016. Three transects were completed along 93W, two of which were nearly coincident; ND and SD were occupied 5 and 4 times, respectively (Figure 1-2b) between 6 April 2016 and 31 May 2016.

Each glider was equipped with a Sea-Bird SBE 41CP conductivity-temperature-depth sensor (CTD), a Seapoint chlorophyll fluorometer, and a 1-MHz Nortek AD2CP Doppler current profiler (*Todd et al.*, 2017). All instruments sampled during the ascending portion of each glider dive from a maximum depth of 1000 m to the surface. CTD and fluorometer measurements were averaged to 10-m vertical resolution after post-processing and quality control. Vertical profiles of absolute horizontal velocity at 10-m resolution were estimated following *Todd et al.* (2017). An example transect (Figure 1-3) resolves major features

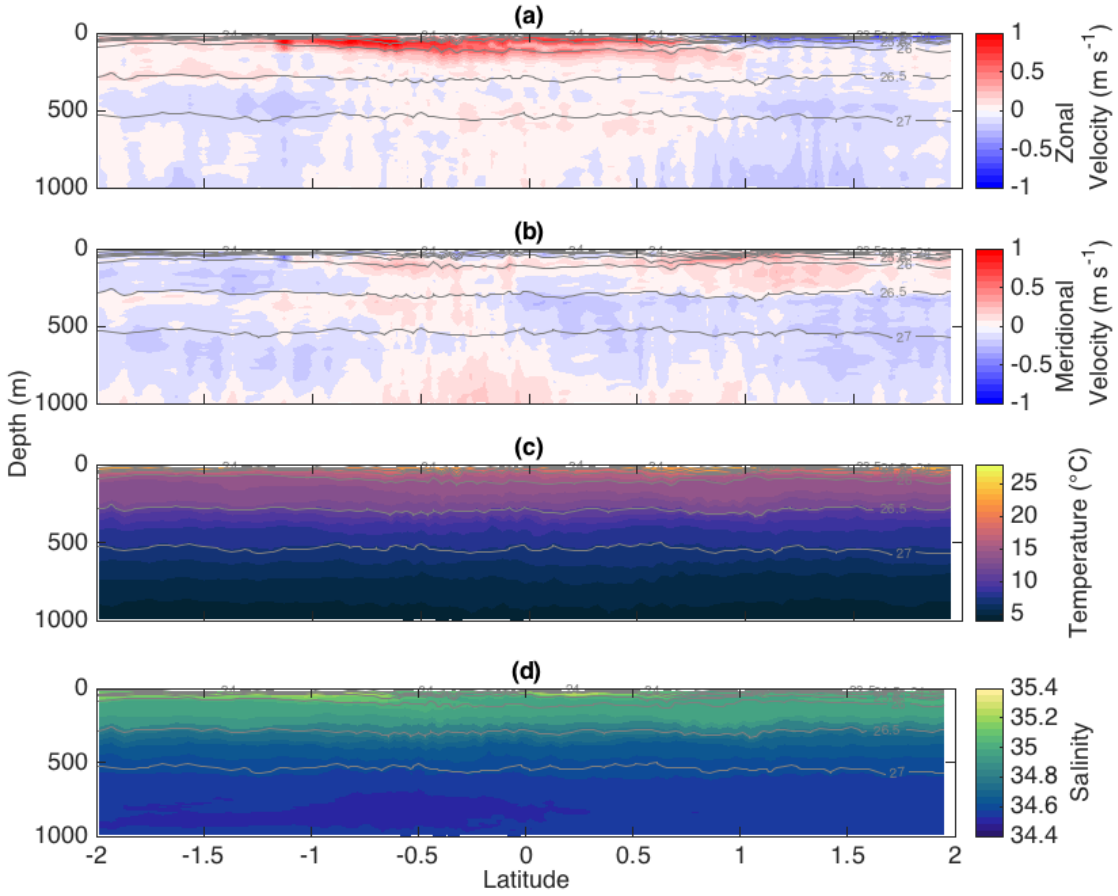

Figure 1-3: Sections of (a) zonal velocity, (b) meridional velocity, (c) potential temperature, and (d) salinity in the upper 1000 m from one southbound transect along 93W from 29 April to 23 May 2016. Isopycnals (kg m^{-3}) are shown in gray.

of the local equatorial current system, including a well-defined EUC core with maximum eastward velocity near 1 m s^{-1}, a relatively strong westward surface flow north of the equator associated with the South Equatorial Current (SEC) and weaker meridional velocities.

Errors in temperature and salinity are small relative to the expected signal after quality control of individual measurements (*Rudnick and Cole*, 2011). Obviously faulty observations due to instrument failure were flagged and excluded. The glider CTDs are highly accurate (*Rudnick and Cole*, 2011), calibrated periodically at Sea-Bird, and checked prior to each mission using a transfer standard in the lab. Salinity and density observations are not available along ND during this time due to a CTD failure.

Estimated error associated with depth-average velocity measurements is $0.01 - 0.02$ m s^{-1} (*Rudnick et al.*, 2018), small compared with typical O(1 m s^{-1}) EUC velocities. Error

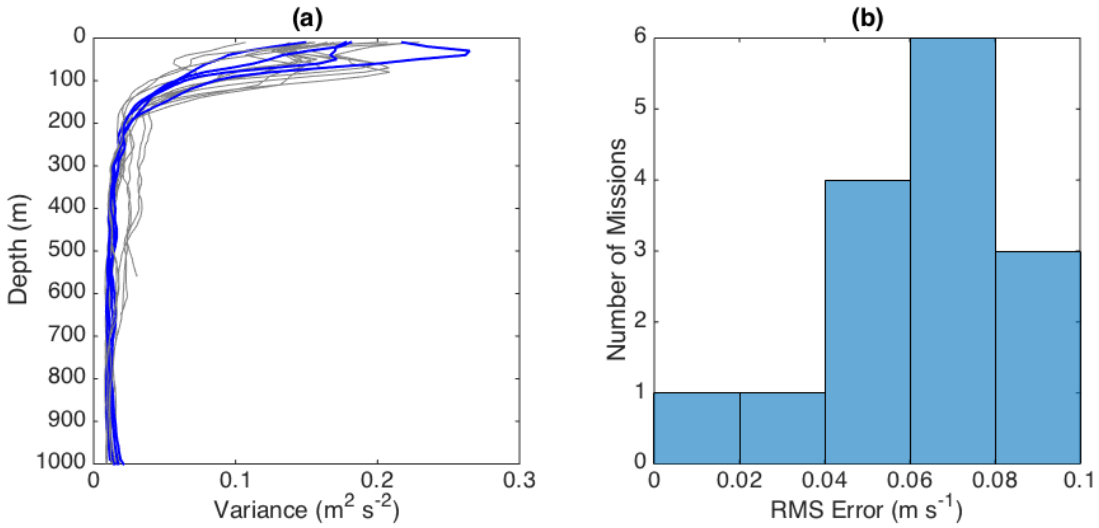

Figure 1-4: (a) Profiles of velocity variance for each ROGER glider mission (gray) with the missions analyzed here highlighted in blue. (b) Histogram of RMS errors (Equation 1.1) for each of the 15 glider missions that sampled to 1000 m.

in depth-average velocity sets the absolute accuracy of velocity profiles (*Todd et al.*, 2017). To estimate depth dependent velocity errors, *Todd et al.* (2017) compared velocity profiles from two earlier ROGER glider missions that crossed paths three times while simultaneously occupying 93W. The root-mean-square (RMS) difference was between 0.07 and 0.09 m s^{-1} for those three crossings. RMS error of horizontal velocity for an individual profile reaches a minimum near the middle of the profile as a result of constraining velocity profiles to match measured depth-average velocity (*Visbeck*, 2002) and increases with decreasing scatterers at depth. We assume that variance in the ocean should not increase with depth after a minimum value is reached. Following *Todd et al.* (2017), profiles of velocity variance for 16 similarly equipped ROGER glider missions deployed along ND, 93W, and SD (April 2014 – May 2016) have minimal increase at 1000 m depth, with slight increases corresponding to two missions used in this analysis (Figure 1-4a).

RMS errors for all ROGER missions that sampled to 1000 m are calculated as

$$\sigma_{\text{rms}} = \sqrt{\sigma^2_{1000\text{m}} - \sigma^2_{z_0}} \tag{1.1}$$

where z_0 is the depth of minimum variance for each mission (average $z_0 = 676$ m) and σ^2 is the variance over the length of the mission. RMS errors are sufficiently small ($0.05 - 0.1$

m s^{-1}; Figure 1-4b) to capture the velocities of interest in this study. These estimates are smaller than those of *Todd et al.* (2017) due to minor updates in post processing, particularly changes to quality control thresholds that admit a greater number of individual measurements of current velocity relative to the gliders. All further analyses include only observations obtained between 6 April 2016 and 31 May 2016.

1.3 Results

1.3.1 Velocity Observations along Transects

Average transects of flow across (normal to) and along 93W, SD, and ND during 6 April 2016 – 31 May 2016 are constructed by rotating velocities, gridding and smoothing individual transects, and finally averaging transects. Velocities below 300 m are small (< 0.1 m s^{-1}), consistent with Figures 1-3a and 1-3b, and are not considered further. Velocities for each transect along the three lines are gridded onto on a 15-km horizontal grid using a Gaussian weighted average of the nearby data in order to smooth high frequency variability. Following *Rudnick et al.* (2017), the Gaussian weighting function $W(y)$ is

$$W(y) = \exp\left(\frac{-(y-d)^2}{L^2}\right), \tag{1.2}$$

where d is the along-track position of a grid point, $L = 15$ km is the chosen scale of the Gaussian weight, and y is along-track position of a measurement. The Gaussian scale is chosen based on the frequency spectrum of normal velocity at 50 m depth of all transects, consistent with *Rudnick and Cole* (2011) and *Rudnick et al.* (2017). The weighted average is

$$v(d) = \sum_{i=1}^{m}(W(y_i) \cdot v(y_i))/\sum_{i=1}^{m} W(y_i), \tag{1.3}$$

where $v(d)$ represents gridded velocity (or other gridded field) and summation is over the m observations within 80 km of the grid point, beyond which $W(y) < 0.001$. Time average velocity is obtained by taking the average of all transects along each line. We assume that individual transects, lasting 10–20 days, are statistically independent and can be weighted equally, with the exception of those along 93W. Since two transects occur at nearly the same time along 93W (Figure 1-2), we use a weighted average for 93W transects, giving twice the weight to the first transect. Standard error estimates of the average sections of velocity are

included in Appendix 1.A.

Average velocity normal to 93W during April – May 2016 (Figure 1-5a) shows a clear EUC core with eastward flow peaking near 0.9 m s^{-1} at 50 m depth and 0.7°S. Measured near the end of the 2015 – 2016 El Niño, this velocity is higher than the El Niño average calculated by *Johnson et al.* (2002), but lower than the La Niña average or the general long term average. During this time, the EUC core (normal velocity > 0.3 m s^{-1}) extends roughly from the surface to 180 m depth and from 1.25°S to 0.5°N. North of the EUC, the westward SEC has a maximum velocity of 0.7 m s^{-1} and extends vertically from the surface to a depth of 75 m and meridionally from 0.5°N through the end of the line at 2°N based on westward velocities greater than 0.1 m s^{-1}. These observations are consistent with previous studies of the equatorial current system along 95°W (*Johnson et al.*, 2001, 2002).

Normal velocities along the two diagonals during April – May 2016 show the bifurcation of the EUC around the Galápagos Archipelago. Regions of high velocity out of the control volume (V_{gl}, defined by A_{gl}, the 0 m and 300 m depth surfaces) are found across ND and SD (Figure 1-5b) on both sides of the Galápagos Archipelago. The magnitude of maximum velocity out of the volume is 0.5 m s^{-1} along both ND and SD at depths of 60 m and 70 m respectively, indicating that the speed of the EUC core decreases as the EUC branches around the Galápagos Archipelago, consistent with the results of *Karnauskas et al.* (2010).

The southern branch of the EUC extends from the surface to about 150 m depth, with some weaker flow (< 0.2 m s^{-1}) reaching 300 m. The northern branch extends from the surface to 200 m, with very little flow below that. Thus, the decrease in maximum velocity along the two diagonals is also associated with increased vertical extent. The flow between the Galápagos Archipelago and 93°W across SD is dominated by the EUC branching around the south side of the archipelago with negligible flow into V_{gl}. Across ND, the north branch of the EUC is at a maximum close to the archipelago while flow reverses across ND north of 0.75°N where the SEC dominates.

Although our focus is velocity normal to each transect for the purpose of estimating volume transport, we note that tangential (along-track) velocity (Figure 1-9) is consistent with the behavior of tropical cells modeled by *McCreary and Lu* (1994). Near the surface along 93W there is clear poleward flow, likely a result of Ekman divergence (e.g., *Wyrtki and Kilonsky*, 1984; *Johnson et al.*, 2001; *Perez and Kessler*, 2009). During this time period, poleward flow continues below the thermocline down to 280 m, deeper than a typical equa-

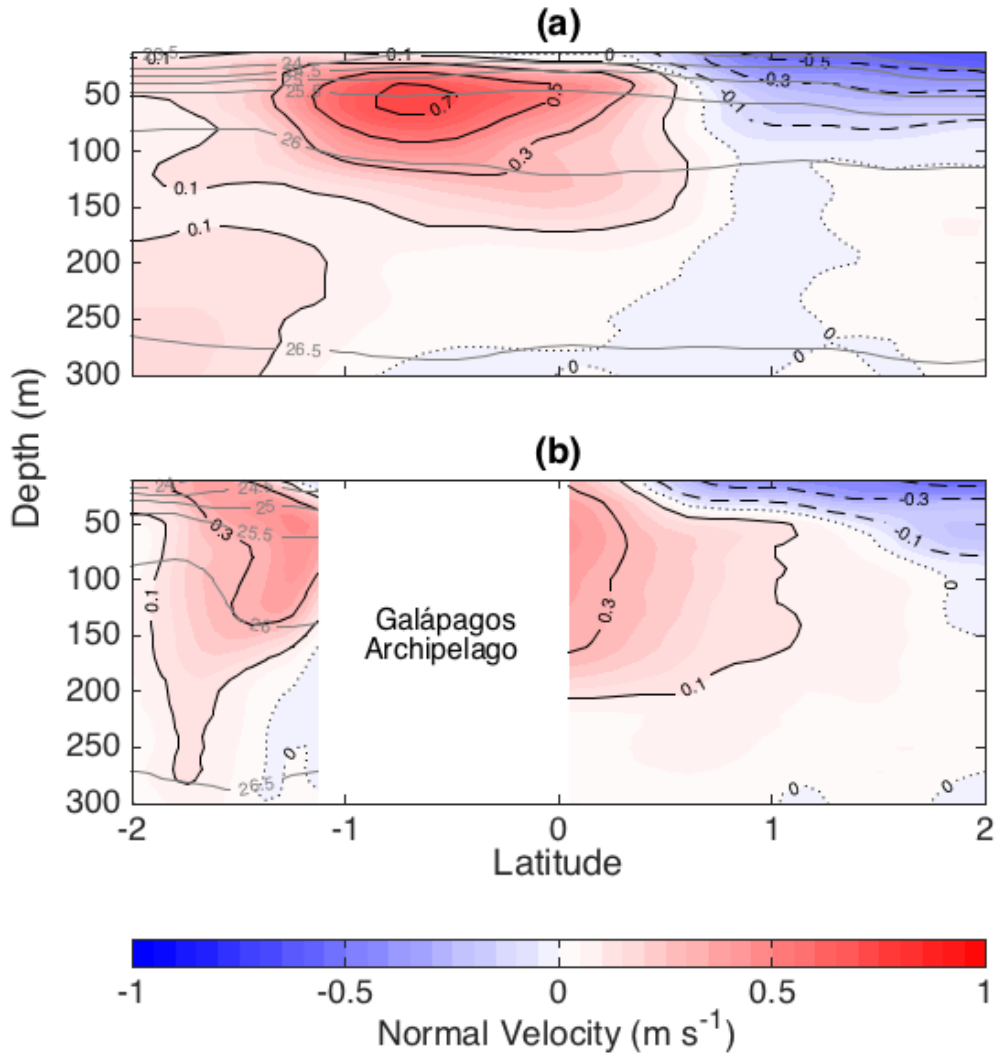

Figure 1-5: Time average of velocity normal to (a) 93W and (b) ND and SD above 300 m. Positive (negative) velocities eastward (into V_{gl}) along 93W. Positive velocities are out of V_{gl} along ND (northeastward) and SD (southeastward) for clarity in this figure and Figure 1-13 only (elsewhere, all three survey lines use positive normal velocity into V_{gl}). Isopycnals (kg m^{-3}) are drawn gray and are not available for ND. The gap in panel (b) corresponds to the meridional extent of the Galápagos Archipelago.

torial Ekman layer (e.g., *Johnson et al.*, 2001; *Perez and Kessler*, 2009). The ND section (Figure 1-9b) is dominated by northwestward flow with maximum velocities at the surface due to a combination of SEC and Ekman transport. SD (Figure 1-9b) has mostly southwestward along-track flow with a region of northeastward flow that corresponds to the northward flow just below the EUC core along 93W. The strongest flows along SD are normal to the line resulting in small along-track velocities.

1.3.2 Net Horizontal Transport

We now consider the net volume transport into V_{gl}. For each transect, we define the 'transport profile', $T_n(z)$, as the horizontal volume transport per unit depth ($\mathrm{m}^2\ \mathrm{s}^{-1}$ or $\mathrm{Sv\ m}^{-1}$). $T_n(z)$ is calculated for individual transects by integrating normal velocity over the length of the transect:

$$T_n(z) = \int_0^L u(y,z)dy \tag{1.4}$$

where z is depth, n is an index corresponding to transect number, v is velocity normal to the section, y is the along-track distance of each dive, and L is total line length.

The resulting transport profiles (Figure 1-6) have maximum magnitudes above 300 m. The magnitude of the transport through 93W at the depth of the EUC core varies by nearly a factor of 3 between transects. Similar variations occur along the two diagonals, indicating that variability of the EUC and related transport occurs on time scales $O(20)$ days, which is the time between consecutive transects, and implying that most transects can be considered independent.

We calculate the average transport profile $\overline{T_l}(z)$ for each survey line l (93W, SD, and ND) by averaging $T_n(z)$ from individual transects. A weighted average is used along 93W as in Section 1.3.1. The standard error of the mean, $\sigma_e(z)$ is calculated at each depth level as

$$\sigma_e(z) = \frac{\sqrt{\sum_{n=1}^{N} a_n \left(T_n(z) - \overline{T_l}(z)\right)^2}}{\sum_{n=1}^{N} a_n} \tag{1.5}$$

where N is the number of transects along the line, and a_n is the weight given to each transect T_n. To obtain $\sigma_e(z)$ along 93W we use a weighted variance consistent with the weights used to calculate the average transport profile for 93W. Variability during the finite time (10–25 days) required for gliders to occupy individual transects in not accounted for in estimation of $\sigma_e(z)$.

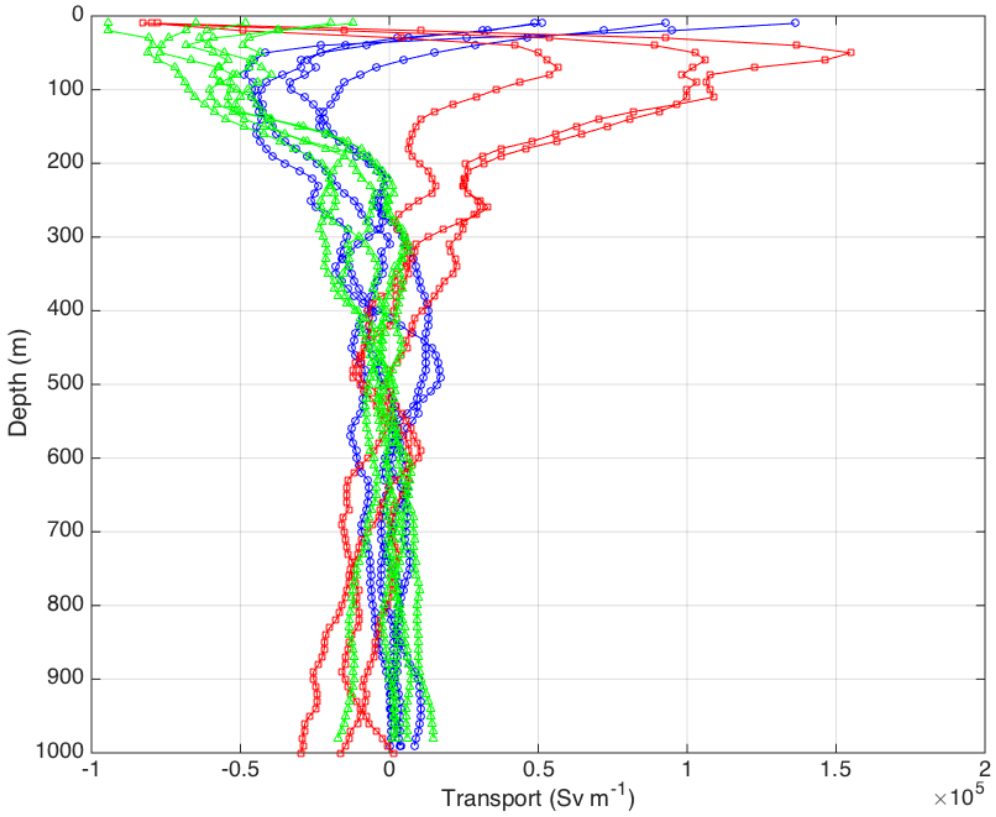

Figure 1-6: Horizontal transport profiles $T_n(z)$ for all complete transects from 6 April 2016 through 31 May 2016 along ND (blue), 93W (red), and SD (green).

Table 1.1: Average transport (Sv) and standard error normal to each line above 300 m. Negative (positive) transport is calculated by summing over only negative (positive) velocities. Positive indicates into the control volume.

Transport Component	ND	93W	SD
Negative	-7.6 ± 0.1	-6.0 ± 0.2	-10.9 ± 0.1
Positive	3.7 ± 0.1	16.4 ± 0.6	0.7 ± 0.1
Total	-3.9 ± 0.2	10.5 ± 0.7	-10.1 ± 0.1

Consistent with average normal velocity (Figure 1-5), average horizontal transport across 93W (Figure 1-7a) tends to be positive (into V_{gl}) below 20 m while average horizontal transports across SD and ND are generally negative (out of V_{gl}). Positive transport across 93W is primarily due to the EUC with its core centered near 50 m depth (Figure 1-5). Strong negative transport is confined to the surface, corresponding to the westward SEC. Negative horizontal transports across SD and ND peak around 50 and 100 m depth, respectively (Figure 1-7a), reflecting splitting of the EUC core around the Galápagos Archipelago as it continues eastward. The sign of horizontal transport for ND changes from positive (0 – 40 m depth) to negative (40 – 300 m) due to the presence of the westward flowing SEC (positive horizontal transport) on the north side of the archipelago that extends from the surface to about 75 m depth north of 0.5°N (Figure 1-5b).

To differentiate the transport of the EUC and SEC around the islands we compute total, negative and positive horizontal transport from the surface to 300 m depth (Table 1.1).

Nearly all of the volume transport of the EUC (16.4 ± 0.6 Sv) bifurcates into two branches north and south of the Galápagos Archipelago, with higher transport to the south (10.9 ± 0.1 Sv across SD vs. 7.6 ± 0.1 Sv across ND, Table 1.1). Subtracting the negative components of horizontal transport along ND and SD from the positive component along 93W provides an estimate for the change in the EUC transport (ΔEUC) between 93W and the diagonals, $\Delta\mathrm{EUC} = -2.1 \pm 0.6$ Sv; more flow exits V_{gl} along the diagonals than enters through 93W. Similarly, $\Delta\mathrm{SEC} = -2.3 \pm 0.2$ Sv is defined as flow into the volume along ND minus flow out along 93W. Over the upper 300 m, ΔEUC and ΔSEC are negative. Together with small positive transport along SD (0.7 ± 0.1 Sv), there is a net divergence in the upper 300 m of -3.6 ± 0.7 Sv.

The three average transport profiles (Figure 1-7a) are summed to give the average net transport profile $\overline{T}_{net}(z)$ into V_{gl} (Figure 1-7b). For a given depth range, when the net trans-

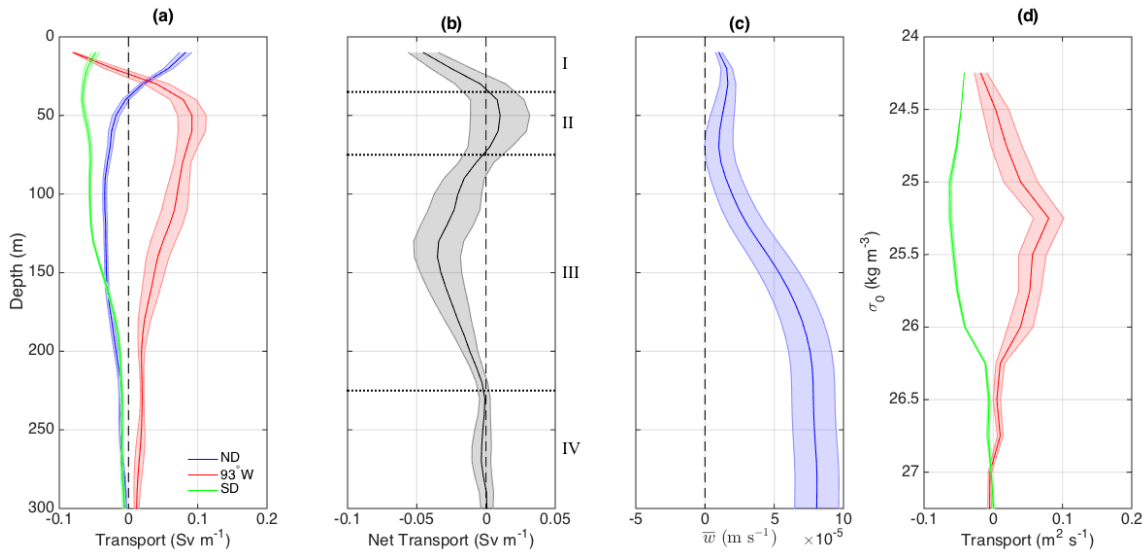

Figure 1-7: Profiles of (a) average horizontal transport $\overline{T}_l(z)$, (b) net horizontal transport into the control volume, (c) vertical velocity, and (d) horizontal transport as a function of potential density in the upper 300 m. Shaded color error bars show standard errors. Dotted lines in (b) delineate depth layers I-IV.

port profile is negative (positive), there is net horizontal divergence (convergence) averaged over the volume at that depth. V_{gl} is divided by depth into four layers using the transport profile of Figure 1-7b. These four layers are: I) 5 – 35 m, II) 35 – 75 m, III) 75 – 225 m, and IV) 225 – 305 m (Figure 1-8).

In Layer I, EUC related flow is divergent (greater flow out along the diagonals than in across 93W). Net divergence in Layer I is dominated by strengthening of the SEC between its entry into V_{gl} across ND and its exit across 93W, primarily due to the entrainment of upwelled waters and the northern branch of the split EUC as it is deflected northward by the archipelago (Figure 1-8a). However, since both ΔEUC and ΔSEC are negative (i.e. the two branches of the EUC transport more water out of V_{gl} along ND and SD than the EUC transports into V_{gl} along 93W), there must be an additional source of volume transport into Layer I. Ekman divergence likely contributes to net divergence via poleward flow on both sides of the equator, as indicated by tangential (along-track) velocities along ND and near 0.5°N along 93W (Figures 1-9 and 1-8a).

Net convergence in Layer II (Figure 1-7b) results from greater transport into V_{gl} by the EUC core across 93W compared with the combined transport out of V_{gl} along the diagonals (Figure 1-8b). SEC divergence is weaker in this layer compared with Layer I (Figure 1-

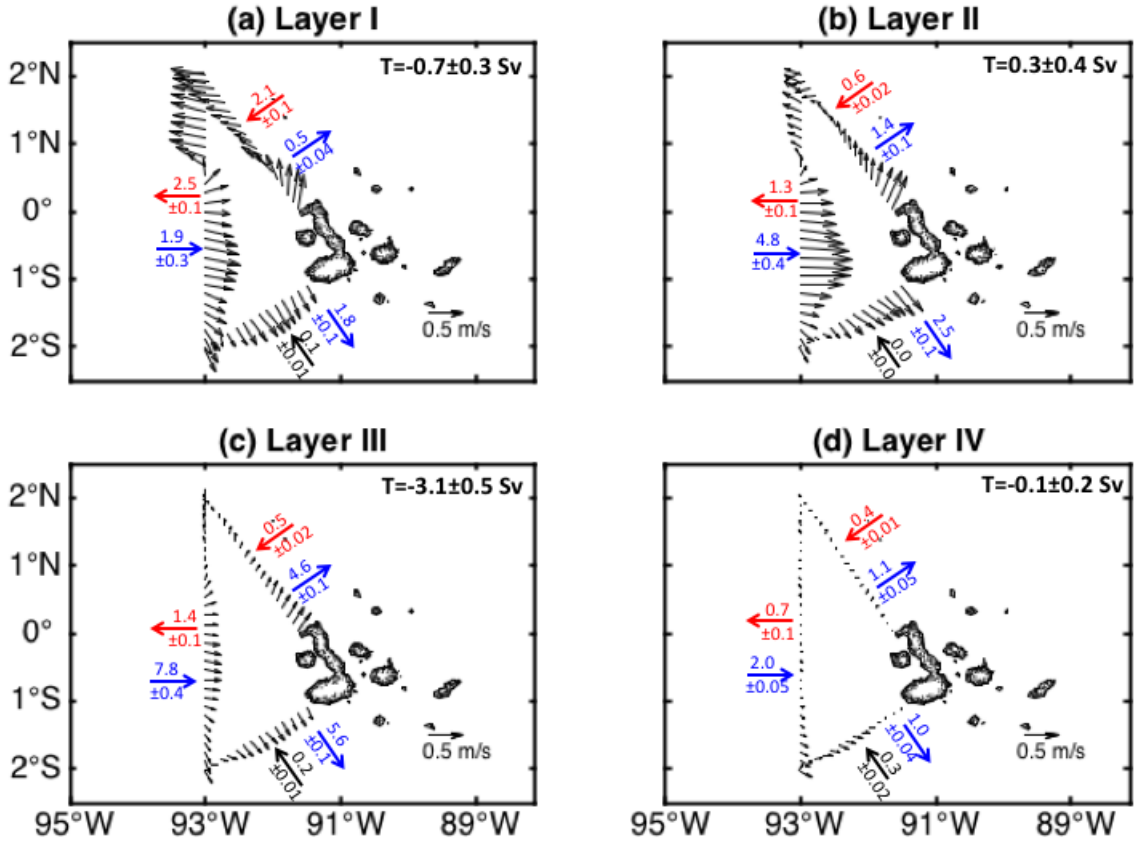

Figure 1-8: Average velocity (m s^{-1}, gridded) over (a) Layer I, 5 – 35 m, (b) Layer II, 35 – 75 m, (c) Layer III, 75 – 225 m, (d) Layer IV, 225 – 305 m. Numerical values are horizontal transport (Sv) in each depth layer. Red indicates flow associated with the SEC (in across ND, out across 93W), while blue is flow associated with the EUC (in across 93W, out across ND and SD). T is the net horizontal transport into the control volume in each layer.

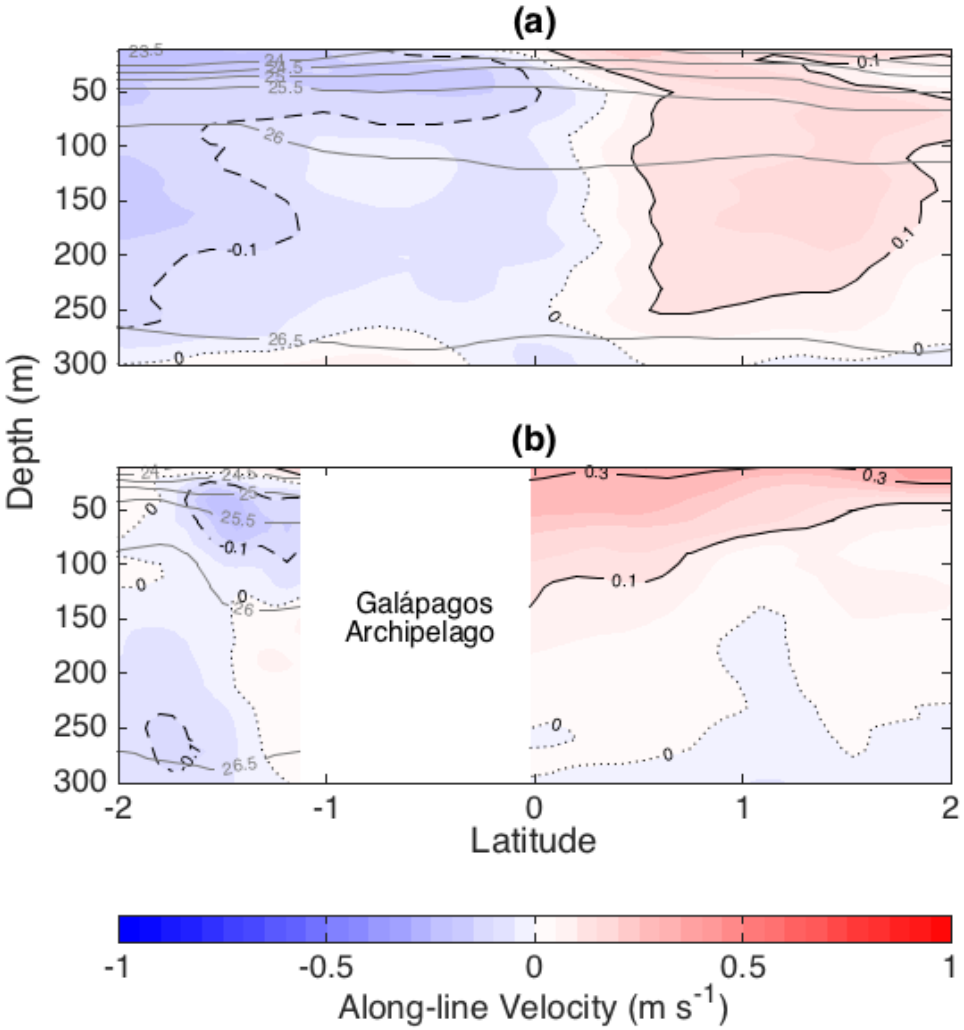

Figure 1-9: As in Figure 1-5 but for velocities tangent to (along) the survey lines. Positive (negative) velocities are northward (southward).

8b). Layer II convergence may be driven by vertical spreading of the split EUC, resulting in decreased transport out of V_{gl} along the diagonals within Layer II, and topographic upwelling of the EUC as it reaches the Galápagos Archipelago. Below Layer II, vertical spreading of the split EUC results in increased transport out of V_{gl} along the diagonals.

Net divergence in Layer III over A_{gl}, below the EUC core, is partially a result of greater EUC related flow out of V_{gl} across the diagonals than in across 93W (Figures 1-8c and 1-5). However, the transport out of V_{gl} has a greater magnitude than transport into V_{gl} in Layer II, which indicates that the net divergence cannot be accounted for solely by downwelling of EUC waters as the EUC splits into two branches. Net divergence over the upper 300 m is discussed further in Section 2.4. Below the EUC, SEC, and Ekman transport, Layer IV is nearly non-divergent (Figure 1-8d).

To provide insight into the mechanisms behind vertical spreading of the EUC branches compared to the incoming EUC across 93W, we calculate average horizontal volume transport profiles across 93W and SD as functions of potential density by interpolating velocity estimates onto potential density surfaces prior to calculating volume transport (Figure 1-7d; ND density is unavailable due to CTD failure). The horizontal transport maximum along 93W and subsequent decrease toward zero below $\sigma_0 = 26.5$ kg m^{-3} occur on the same potential density surfaces as along SD (Figure 1-7d). Between 93W and SD, the some of the divergence in $T(z)$ below 75 m is due to isopycnal spreading. Above $\sigma_0 = 25$ kg m^{-3}, transport across 93W is near zero while transport across SD remains negative near the surface.

1.3.3 Vertical Velocity

Integrating the average net horizontal transport profile (Figure 1-7b) from the surface to 300 m depth gives a net transport of 3.6 ± 0.7 Sv out of the volume. The average vertical velocity required at 300 m to balance this horizontal divergence is $(8.0 \pm 1.6) \times 10^{-5}$ m s^{-1}, indicating net upwelling during the observed time period. To estimate $\overline{w}(z)$, the time- and area-averaged vertical velocity profile in the region A_{gl}, we time average ($\langle \cdot \rangle$) the incompressible continuity equation, solve for $\frac{\partial \langle w \rangle}{\partial z}$, average over A_{gl}, and apply the divergence theorem to obtain

$$-\frac{1}{A_{\mathrm{gl}}} \iint_{A_{\mathrm{gl}}} \frac{\partial \langle w \rangle}{\partial z} dA = \frac{1}{A_{\mathrm{gl}}} \int_P \langle u \rangle dy = \frac{1}{A_{\mathrm{gl}}} \overline{T}_{net}, \tag{1.6}$$

where $\langle u(y,z)\rangle$ is time-average horizontal velocity normal to ND, 93W, and SD, P is the perimeter of A_{gl}, and the incompressible continuity equation is

$$\frac{\partial u}{\partial x}+\frac{\partial v}{\partial y}+\frac{\partial w}{\partial z}=0. \tag{1.7}$$

where u and v are normal and along-track velocity, respectively and x is cross-track distance. We then estimate $\overline{w}(z)$ by integrating the average horizontal volume transport profile $\overline{T}_{net}(z)$ vertically as

$$\overline{w}(z)=-\frac{1}{A_{\mathrm{gl}}}\int_{z}^{z_0}\overline{T}_{net}(z)dz, \tag{1.8}$$

where z is positive upwards and we assume that $w=0$ at $z_0=-10$ m, the shallowest depth at which velocity is estimated. The value of $A_{\mathrm{gl}}=4.51\times10^4$ km^2 is the area of the region with maximum depth greater than 300 m within the polygon defined by the three glider survey lines and Isla Isabela (Figure 1-2). The standard error of the average of vertical velocity,$\sigma_{\overline{w}}(z)$, is

$$\sigma_{\overline{w}}(z)=\int_{z}^{z_0}\sigma_e dz, \tag{1.9}$$

where σ_e is defined in Equation 1.5.

Above 50 m (Figure 1-7c), significant upwelling is consistent with SST observations of Figure 1-1 due to horizontal divergence (negative net transport) that exists above the EUC core (Layer I, Figure 1-8a). The maximum vertical velocity is $(1.7\pm0.6)\times10^{-5}$ m s^{-1} (or 1.5 ± 0.5 m day^{-1}) at 25 m depth. Vertical motions are small compared to horizontal motions, so standard error associated with vertical velocity is high compared to the magnitude of $\overline{w}(z)$ and $\overline{w}(z)$ is not significantly different than zero from about 50 m to 100 m. Vertical velocity decreases below 30 m from the near surface peak until it reaches a minimum near 75 m (Figure 1-7c), corresponding to the region where the EUC core is strongest and there is net convergence in Layer II (Figure 1-8b).

Below 75 m, positive vertical velocity (Figure 1-7c) is primarily attributed to increased vertical extent of the north and south branches of the EUC core in Layer III compared to the EUC core along 93W in Layer II as it reaches the archipelago (Figure 1-8c), resulting in a net divergence in Layer III. Vertical velocity is nearly constant below 225 m, consistent with near zero divergence in Layer IV.

An additional source of error in the vertical velocity calculation is the assumption of

zero divergence at 10 m depth. Westerly wind stress along the equator would result in non-zero Ekman divergence above 10 m. The gliders' downward looking AD2CPs do not resolve depth-dependent velocity shallower than 10 m so any divergence in the upper 10 m is not included in our analysis. Such a divergence would result in a shift of the entire vertical velocity profile toward more positive values, increasing upwelling estimates without impacting estimated errors.

1.3.4 Volume Transport by Salinity Class

Using the methods of Section 1.3.1, we calculate average salinity along 93W and SD (Figure 1-10). A major feature of the average salinity section along 93W (Figure 1-10a) is the subsurface salinity maximum (salinity > 35.1) from 0.5°S to 2°S at the depth of the EUC core (50 m). High salinity water originates in the subtropical South Pacific (*Knauss*, 1966; *Fiedler and Talley*, 2006) and is transported equatorward via multiple pathways (*Johnson and McPhaden*, 1999). The high salinity (35.2–35.25) tongue observed along 93W is bounded by the 25.0 kg m^{-3} and 26.0 kg m^{-3} isopycnals, consistent with observations of *Johnson and McPhaden* (1999) along 125°W. There is an additional local salinity maximum at a depth of 50 m between the equator and 0.5°N, consistent with transient extensions north of the equator in the central Pacific on monthly timescales as described by *Johnson et al.* (2000).

A high salinity tongue similar in shape to that along 93W also exists along SD (Figure 1-10b), although the SD high salinity tongue slopes downward from 2°S to 1.1°S from a depth of 20 m to 70 m. Aside from this downward slope, it appears that the salinity section along SD closely matches in magnitude and spatial pattern the section along 93W between 2°S and about 0.4°S, indicating that much of the water south of 0.4°S entering the volume across 93W exits out the SD. High salinity water exiting along SD has similar temperature and salinity properties to the high salinity tongue along 93W (Figure 1-11). However, SD includes water of higher salinity. This discrepancy could be due to slight differences in sampling coverage between the two lines (Figure 1-2b) as the higher salinity water in the average section is the result of a single SD transect.

We now consider volume transport as a function of salinity class along 93W and SD adapting our methodology from Section 1.3.2. We compute the cumulative volume transport

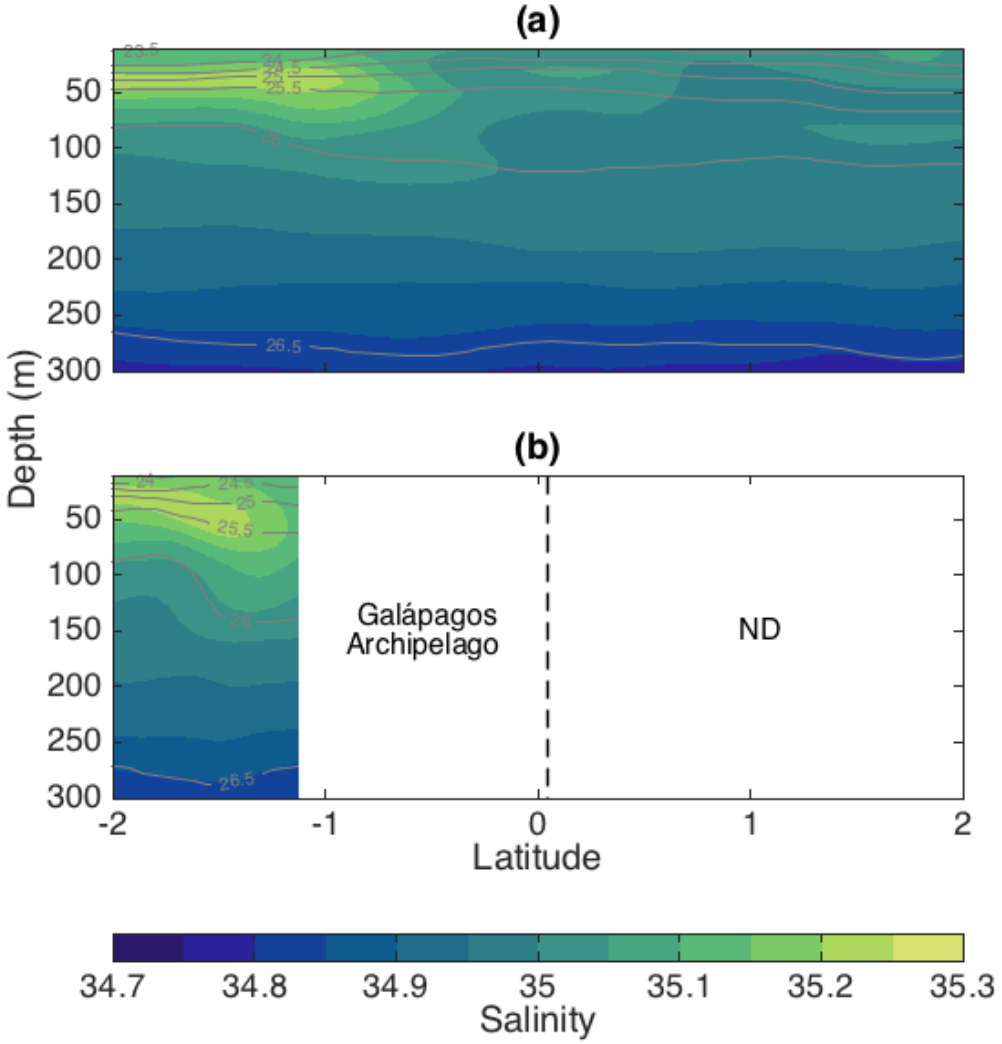

Figure 1-10: As in Figure 1-5 but for salinity. The dashed line in (b) delineates the Galápagos archipelago from ND, where salinity observations were not available. Isopycnals (kg m^{-3}) are shown in gray contour.

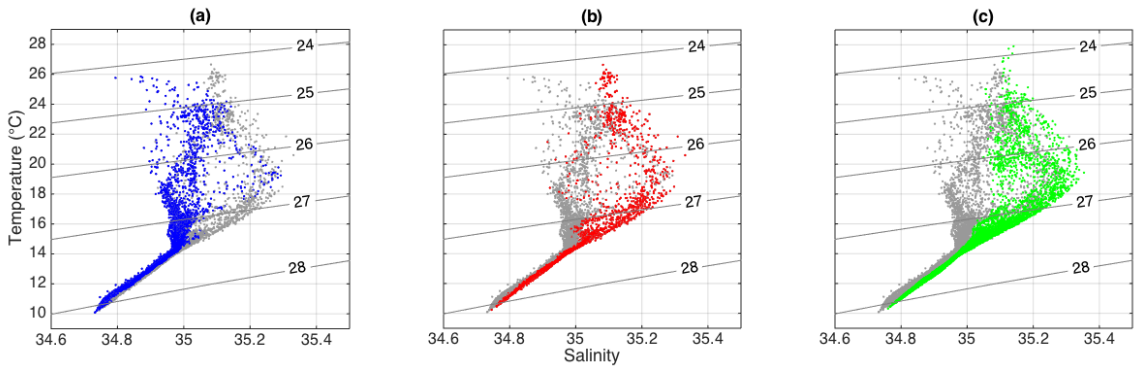

Figure 1-11: Potential temperature-salinity diagram along (a) 93W north of 0.4°S (blue), (b) along 93W south of 0.4°N (red), and (c) along SD (green). In (a)–(c), all potential temperature-salinity pairs along 93W between 2°S and 2°N are shown in gray dot. Isopycnals (kg m^{-3}) are shown in gray contour.

of waters in the upper 300 with salinity less than salinity S through 93W and SD as

$$T_n(S) = \int_{300\text{ m}}^{z=10\text{ m}} \int_0^L u(y,z) H\big(S - s(y,z)\big) dy dz \tag{1.10}$$

where n is the index corresponding to a single transect, H is the heaviside function, S is the upper salinity bound, $s(y,z)$ is the observed salinity, and L is the length of the line. $\overline{T}_l(S)$ is the time average of $T_n(S)$ for a given survey line, where subscript l indicates 93W or SD. Standard error for $\overline{T}_l(S)$ is

$$\sigma_l(S) = \frac{\sqrt{\sum_{n=1}^{N} a_n \left(T_n(S) - \overline{T(S)}\right)^2}}{\sum_{n=1}^{N} a_n} \tag{1.11}$$

where N and a_n remain the same as in Section 1.3.2 for SD and 93W.

Volume transport is into the volume along 93W for all salinity classes as indicated by the monotonically increasing cumulative transport (Figure 1-12a, red); similarly, transport is out of the volume for all salinity classes along SD (Figure 1-12a, green). Volume transport as a function of salinity along ND is estimated by assuming that net horizontal volume transport is zero for each S so that $\overline{T}_{ND}(S) = -\big(\overline{T}_{93W}(S) + \overline{T}_{SD}(S)\big)$. For salinities above 35, transport into V_{gl} across 93W is nearly equal to transport out across SD, as indicated by nearly constant cumulative transport of salinities above 35 along ND (Figure 1-12a). The high salinity tongue transported into V_{gl} across 93W leaves through SD. In the salinity range $34.9 - 35$, waters flowing in across 93W are not accounted for by flow out across SD,

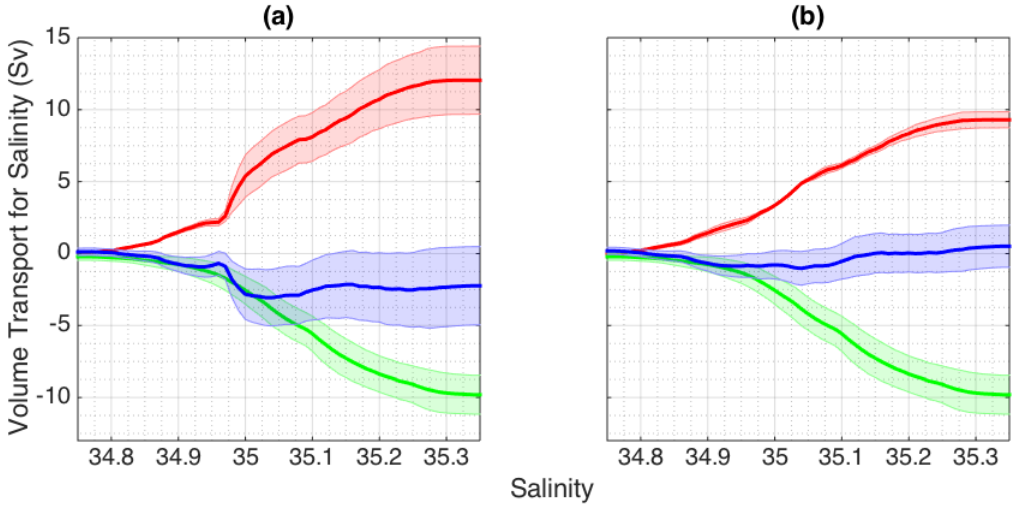

Figure 1-12: (a) Cumulative volume transport as a function of salinity for 93W (red) and SD (green). Cumulative transport through ND is calculated as a residual due to the lack of CTD data. Shading shows standard errors. Positive transport is into the control volume. (b) As in (a), but for transport through 93W only south of 0.4°S.

implying transport of those waters out of V_{gl} across ND.

To examine meridional dependence of these results, we recompute $T_{93W}(S)$ using only observations between 2°S and 0.4°S along 93W line (Figure 1-12b). The cutoff latitude of 0.4°S was obtained by minimizing the average squared difference between $T_{93W}(S)$ and T_{SD}(S), such that residual transport through ND was as small as possible for all S (Figure 1-12b). This latitude can be interpreted as the boundary where the EUC splits into north and south branches around the Galápagos Archipelago. Relatively fresh water (salinities between 34.8 – 34.9) occurs near 300 m and is accounted for by small, non-zero (negative slope, Figure 1-12b) transport through the ND in those classes consistent with northward velocity south of the equator below 250 m (Figure 1-9). This northward velocity advects cold, fresh water from south of the equator northward where it is then advected out of the volume by the northern branch of the EUC.

Upon reaching the Galápagos Archipelago, the EUC splits into a north and south branch. Water south of 0.4°S flows south around the archipelago, while water north of the cutoff latitude flows north around the islands. The cutoff latitude south of which nearly all water that enters V_{gl} across 93W exits along SD is close to the latitude of the center of the Galápagos Archipelago and the approximate average latitude of the EUC core during this time period (Figure 1-5). Water mass properties in the south branch of the EUC match

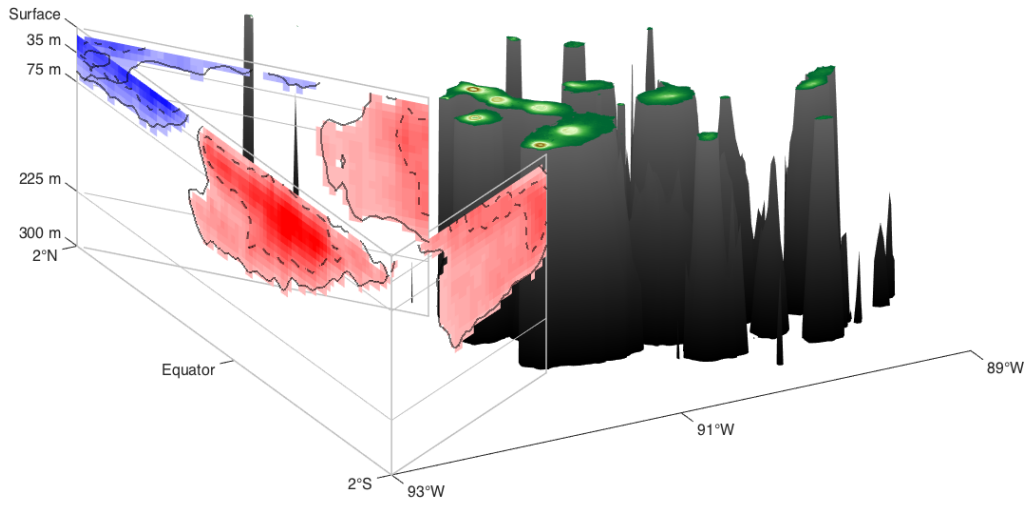

Figure 1-13: Schematic showing sections of normal velocity with magnitude greater than 0.1 m s^{-1} across 93W, ND and SD with the bathymetry of the Galápagos Archipelago in the upper 300 m. Flow related to the SEC (generally westward) is shown in blue, while EUC (generally eastward) is red as in Figure 1-5.

those of waters in the southern half of the EUC along 93W (Figure 1-11). Volume transport calculations along ND (north branch of the EUC) imply that a similar scenario occurs north of 0.4°S.

1.4 Summary and Discussion

Autonomous underwater glider observations during April–May 2016 capture the bifurcation of the EUC around the Galápagos Archipelago (Figures 1-5 and 1-13) and allow estimation of upwelling (Figure 1-7) that supports the persistent, anomalously cold SST of the GCP (Figure 1-1). Time-average velocity over the 52 day time period shows a coherent EUC and SEC along 93W. Along both ND and SD, there is transport out of the volume at the depth of the EUC, indicating the EUC splits into a northern and southern branch as it encounters the Galápagos Archipelago (Figure 1-13).

Model analyses have suggested that the path of the EUC around the Galápagos Archipelago may have impacts on the local ecosystem (*Karnauskas et al.*, 2015), model resolution of

ENSO (*Karnauskas et al.*, 2008), the equatorial Pacific cold tongue (*Karnauskas et al.*, 2007), and the basic state of the tropical Pacific (*Karnauskas et al.*, 2014). Validation of these model results requires observations of the path of the EUC just west of the Galápagos Archipelago, such as those presented here. Additionally, it is unknown to what degree and by what pathway the EUC contributes to the eastern equatorial Pacific cold tongue that extends westward from the coast of South America (*Wyrtki*, 1966; *Philander*, 1973; *Kessler*, 2006; *Karnauskas et al.*, 2007). This study does not directly address the latter question, but the observed bifurcation of the EUC (Figure 1-5) indicates that the two branches may reach the western edge of the eastern Pacific cold tongue at 90°W (Figure 1-1) while maintaining most of the zonal transport of the EUC prior to its encounter with the Galápagos Archipelago.

The bifurcation of the EUC along 92°W was previously estimated by *Lukas* (1986) using a climatological average of historical observations between 100°W and 80°W. Because these sections were taken on either side of the Galápagos Archipelago, the splitting of the two branches was not directly observed. However, the beginnings of the split into a north and south branch were evident along 92°W with a north branch extending down to 400 m, much deeper than the weaker south branch. Along 88°W, two eastward branches existed on either side of the equator, with the stronger branch to the north. During April – May 2016, our analysis shows two nearly equal branches with similar vertical extent to 200 m. Differences between our results and those of *Lukas* (1986) may be due to temporal differences between the two studies relative to annual and ENSO cycles.

Total volume transport of the EUC into the volume across 93W (16.4 ± 0.6 Sv) is lower than previous estimates in the central Pacific of 20 – 30 Sv (*Lukas and Firing*, 1984; *Wyrtki and Kilonsky*, 1984), due to the well-known weakening of the EUC as it moves eastward (*Johnson et al.*, 2002), possible effects of the 2015 – 2016 El Niño and/or the annual cycle of wind-stress in the equatorial Pacific (*Kessler et al.*, 1998). *Wyrtki and Kilonsky* (1984) reported the EUC transport to be 22 Sv along 150°W during 1979 – 1980. These discrepancies in EUC transport between studies are due to multiple factors in additional to differences in longitude.

The average vertical velocity profile (Figure 1-7c) indicates upwelling throughout the upper 300 m, with maximum value at 300 m. While this result is surprising, we expect vertical velocity in the region of A_{gl} to differ from the general equatorial upwelling reported

by previous studies (e.g., *Weisberg and Qiao*, 2000; *Johnson et al.*, 2001; *Wyrtki*, 1981) due to the presence of the Galápagos Archipelago. A major difference between this estimate and those of previous studies is that the average vertical velocity profile estimated here has high values below the EUC core.

Upwelling near the surface coincides with strengthening of the SEC between ND and 93W and may be due to poleward Ekman transport combined with shoaling of some EUC flow between 93W and the diagonals. Increase in SEC transport may be attributed to entrainment of both upwelled waters and the northern branch of the split EUC. However, entrainment of the EUC into the SEC or vice versa alone is not sufficient to explain divergence near the surface, since ΔEUC and ΔSEC are both negative (Section 1.3.2). Upwelling below 110 m is associated with vertical spreading of the EUC across ND and SD compared to the coherent EUC core across 93W, resulting in net divergence below the EUC core. We are unable to resolve the distinct mechanisms maintaining the GCP; however, the observations suggest that a combination of topographic upwelling of the EUC as it reaches the Galápagos Archipelago, wind-driven coastal upwelling, and Ekman divergence along the equator contribute to the existence of the GCP.

In Layers I (0 – 35 m) and III (75 – 225 m) of Section 1.3.2, negative transport has greater magnitude than positive transport associated with the EUC. In addition, ΔEUC and ΔSEC are both negative, indicating that greater volumes of water are leaving V_{gl} than entering V_{gl} in via the EUC and SEC. This suggests that a mechanism beyond vertical spreading of the EUC is necessary to account for the overall net divergence (upwelling) in the upper 300 m. During the two-month average presented here, and a three-year average also calculated using ROGER observations (personal communication with Daniel Rudnick), divergence in the along-track direction ($\partial v/\partial y$) along 93W extends all the way through the upper 300 m (Figure 1-9a, two-month average). It is possible that, in an incompressible ocean, meridional divergence along 93W is balanced by an opposite zonal convergence (Equation 1.7), such as in the case of a slowing EUC as it moves eastward. While it is likely the EUC is slowing between 93W and the Galápagos Archipelago based on the normal velocities of Figure 1-5, the EUC is confined to the upper 150 m and meridional divergence occurs over the entire upper 300 m, centered north of the EUC core near 1°N – 2°N. Combined with overall net divergence in the upper 300 m, it is likely that the meridional divergence along 93W (Figure 1-9a) is associated with upwelling just north of the equator. The mechanism driving this

meridional divergence is currently unknown. The average vertical velocity profile of Figure 1-7c may be a result of divergence/convergence of the EUC and SEC superimposed on the upwelling in the upper 300 m that is suggested by the meridional velocity section along 93W.

Upwelling below 75 m is partially attributed to vertical spreading of the branches of the EUC compared to the EUC core along 93W. However, this vertical spreading below 75 m implies downwelling, not upwelling, between 93W and SD. Average SST (Figure 1-1b) reaches a minimum in a limited region near 0.75°S. According to average density sections (gray contours of Figure 1-10), isopycnals slope downward between 93W and SD (and presumably between 93W and ND, although density estimates are not available). We expect isopycnals to slope upwards between 93W and the Gaápagos Archipelago near the latitude of minimum SST (maximum upwelling), which the gliders did not directly observe. In addition, SST is impacted by wind stress and anomalously cold SST resulting from upwelling is likely advected into a broader region than where the upwelling actually occurs. While sections of velocity normal to 93W and SD indicate downwelling as the EUC flows eastward, SST (Figure 1-1b) suggests a limited region of localized, intense upwelling within A_{gl}. The average vertical velocity profile over A_{gl} incorporates intense upwelling just off the coast of Isla Isabela, possible upwelling associated with the meridional divergence over the upper 300 m, and possible regions of downwelling consistent with vertical spreading of the two branches of the EUC.

Regional ocean model results of *Karnauskas et al.* (2007) indicate upwelling in the upper 300 m along the equator west of the Galápagos Archipelago, with a maximum near 300 m (*Karnauskas et al.*, 2007, their Figure 12d). On the equator, upwelling is apparent over the entire upper 300 m and over the distance between 93W and the archipelago, consistent with the meridional divergence of Figure 1-9a. The same model (*Karnauskas et al.*, 2007, their Figure 14) shows deepening and slowing of the two branches of the EUC as they bifurcate around the archipelago. It remains to examine the mechanisms resulting in vertical spreading of the EUC after bifurcation. It would also be useful to obtain measurements of temperature, salinity, and current velocity along a zonal transect between 93W and the archipelago at the latitude of minimum SST within the region of the GCP, and directly compare the observed zonal transect with model estimates of isopycnal shoaling/deepening. This approach would have the benefit of examining whether cold SST of the GCP is due to isopycnal shoaling,

vertical mixing, or a combination of these.

SST observations (Figure 1-1) suggest that the region between 93°W and 91.5°W would be characterized by enhanced upwelling compared to the central equatorial Pacific. Our estimate of upwelling above 50 m, with maximum value of $(1.7 \pm 0.6) \times 10^{-5}$ m s^{-1} at 25 m, is slightly less than the maximum magnitude of $1.9 - 2.0 \times 10^{-5}$ m s^{-1} reported by *Weisberg and Qiao* (2000) at 140°W and by *Johnson et al.* (2001) at $170 - 95$°W, but agrees within standard error. *Wyrtki* (1981) estimated upwelling across the 50 m depth surface in the central Pacific to be 1.1×10^{-5} m s^{-1}, less than our estimate. These differences may be attributed to a combination of the following:

1. Discrepancies in upwelling between studies are impacted by the relatively broad meridional extent of A_{gl}, as *Johnson et al.* (2001) showed that the maximum in equatorial upwelling occurs along the equator and decreases with increasing latitude. The western (93W) and eastern (Galápagos Archipelago) boundaries of A_{gl} span 4° and 1.1° of latitude about the equator, respectively, with the centroid of A_{gl} located slightly south of the equator at 0.3°S. *Weisberg and Qiao* (2000) and *Johnson et al.* (2001) obtained higher vertical velocity estimates from observations that spanned 2° across the equator. *Wyrtki* (1981) used data from a meridional range of 4° centered at the equator and arrives at an estimate less than the one in this study. Our estimated $\overline{w}(z)$ is an average over A_{gl}, yet the SST minimum associated with the GCP (Figure 1-1) is confined to a fraction of A_{gl}. If upwelling associated with the GCP occurs over an area smaller than A_{gl}, our estimated vertical velocity over the smaller area is proportionally stronger than that in Figure 1-7c.

2. The spatial extent of the GCP is limited to a smaller horizontal area during the 6 April 2016 – 31 May 2016 time period compared to the 2004 – 2016 time average (Figure 1-1), consistent with topographic upwelling of a weaker-than-average EUC. On seasonal timescales, *Kessler et al.* (1998) and *Kessler* (2006) show that meridional and zonal wind stresses along the equator between 95°W – 90°W are at a minimum while equatorial SST is at a maximum during April – May. Climatologically, the EUC is seasonally stronger than average during April – May (*Johnson et al.*, 2002), yet the EUC observed by the gliders during April – May 2016 is weaker than average. This is likely due to the impact of the end of the 2015 – 2016 El Niño.

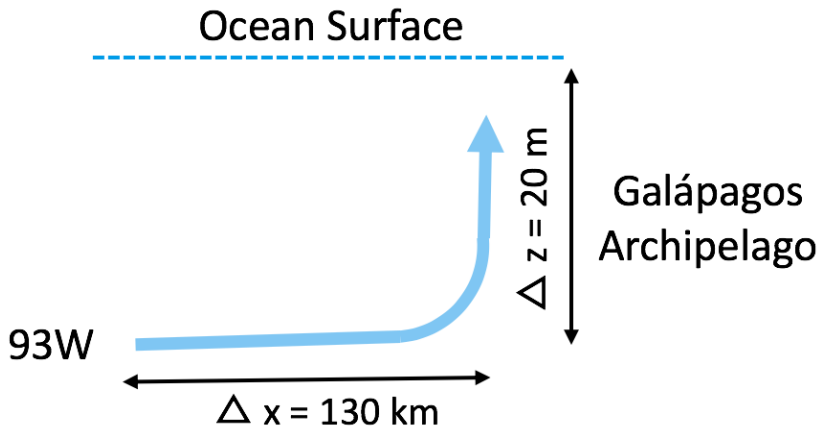

Figure 1-14: Schematic of water parcel traveling eastward from 93W and upwelling into the GCP.

3. The end of the strong 2015 – 2016 El Niño may have resulted in decreased equatorial upwelling compared to a long-term average. In addition to potentially decreasing the maximum velocity of the EUC core, El Niño events are associated with a decrease or reversal in easterly trade winds, after initial anomalous westerly wind bursts (*Firing et al.*, 1983). A decrease in trade wind magnitude could result in minimal surface divergence along the equator and decreased equatorial upwelling, in addition to decreasing potential wind-driven topographic upwelling in the lee of the Galápagos Archipelago.

As a simple check of the estimated vertical velocity profile in the upper 50 m, we consider the minimum SST in Figure 1-1b of 22°C, which occurs at a latitude of 0.75°S. Along 93W at the latitude of the minimum SST, the average depth of the 22°C isotherm is approximately 20 m. The distance of the point of minimum SST in the GCP from 93W is approximately 130 km, which suggests that a parcel of water with minimum SST in the GCP rises 20 m over 130 km between 93W and the point at which it reaches the surface (Figure 1-14). If the parcel travels at a constant velocity equal to the velocity it has when crossing 93W (approximately 0.1 m s^{-1} at 20 m depth and 0.75°S, Figure 1-5a), the vertical velocity necessary to reach the surface by the time it reaches the GCP is 1.3 m day^{-1}. This estimate is remarkably close to that of the average vertical velocity profile in the upper 50 m, which has a maximum value of 1.5 m day^{-1} at 25 m depth.

Volume transport as a function of salinity shows that the meridional boundary where the split between the branches occurs is at 0.4°S, just north of the meridional center of the Galápagos Archipelago and the EUC core. Figure 1-12b indicates that the high salinity

tongue, extending equatorward from the southern hemisphere, is advected south of the Galápagos Archipelago as the EUC splits into north and south branches.

Although this study was limited in time to a single 52-day period in 2016, we successfully observed the path of the EUC just west of the Galápagos Archipelago. Future studies will leverage temporal variability over the full three-year time period of available glider observations to further understand mechanisms behind results presented here. Results of this study will be quantitatively compared to model results (e.g., *Karnauskas et al.*, 2007, 2014) to improve understanding of implications of the observed bifurcation and upwelling of the EUC at the Galápagos Archipelago.

1.5 Acknowledgments

Spray glider operations would not have been successful without the support of the Instrument Development Group at the Scripps Institution of Oceanography (Jeff Sherman, Evan Randall-Goodwin, Derek Vana, Kyle Grindley, Brent Jones, and Ben Reineman) and Larry George and Patrick Deane at WHOI. Glider deployment was made possible through collaboration with the Ecuadorian Instituto Oceanográfico de la Armada (INOCAR). Thank you to Susan Wjiffels, Glenn Flierl, and Thomas Farrar for their discussions and input. This work was supported by National Science Foundation (grants OCE-1232971 and OCE-1233282) and the NASA Earth and Space Science Fellowship Program (grant 80NSSC17K0443). Colormaps are from *Thyng et al.* (2016). Glider observations are available by request from the authors.

1.A Standard Error of Average Sections

Standard error of average velocity (Figure 1-15) and salinity (Figure 1-16) are estimated as

$$\sigma_e(x,z) = \frac{\sqrt{\sum_{n=1}^{N} a_n \left(C(x,z) - \overline{C(x,z)}\right)^2}}{\sum_{n=1}^{N} a_n}, \tag{1.12}$$

where $C(x,z)$ is velocity or salinity of a point on a gridded transect, x is along-line distance, and z, N, and a_n are consistent with Equation 1.5.

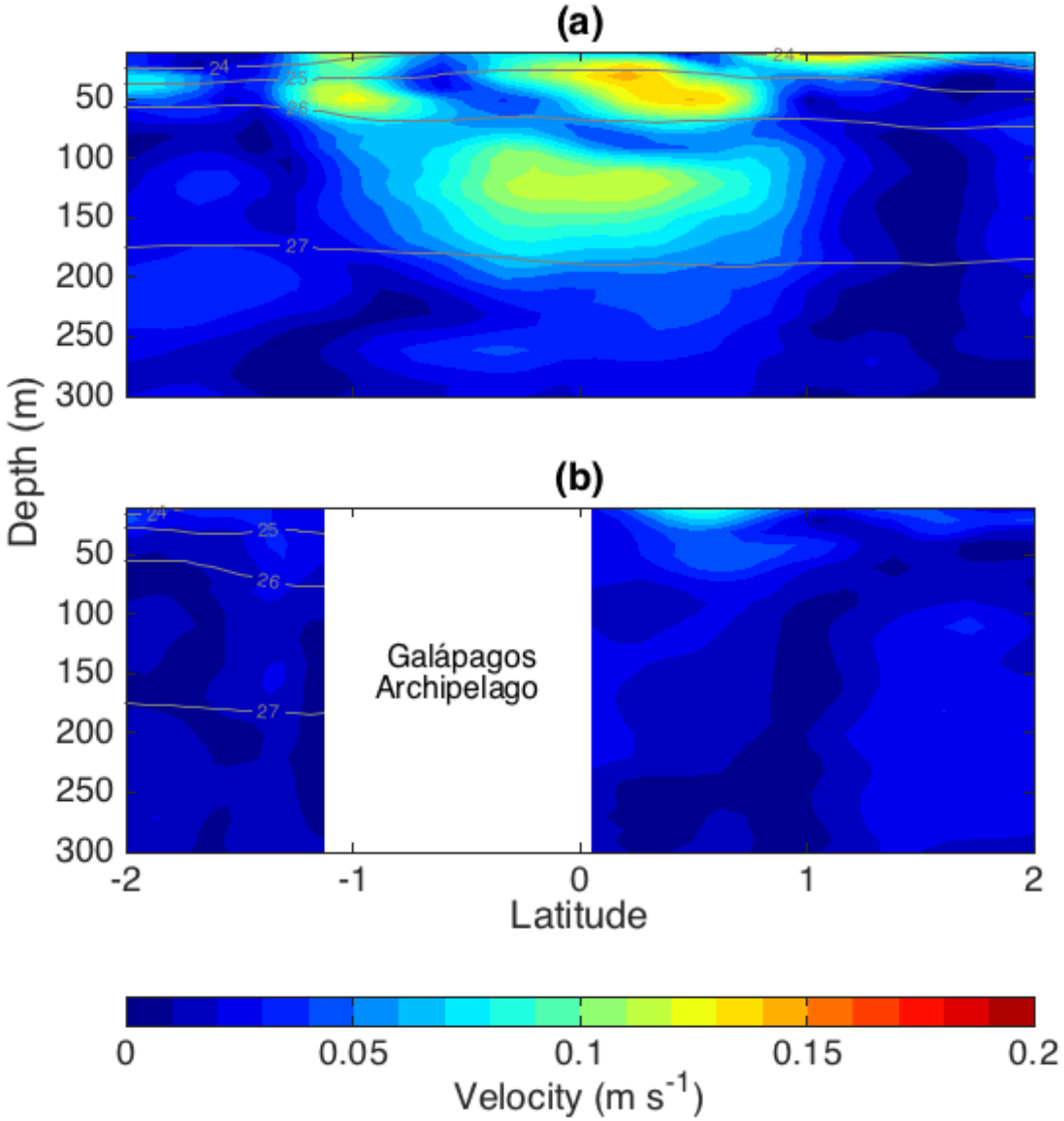

Figure 1-15: Estimated standard error of time average velocity normal to (a) 93W and (b) ND and SD.

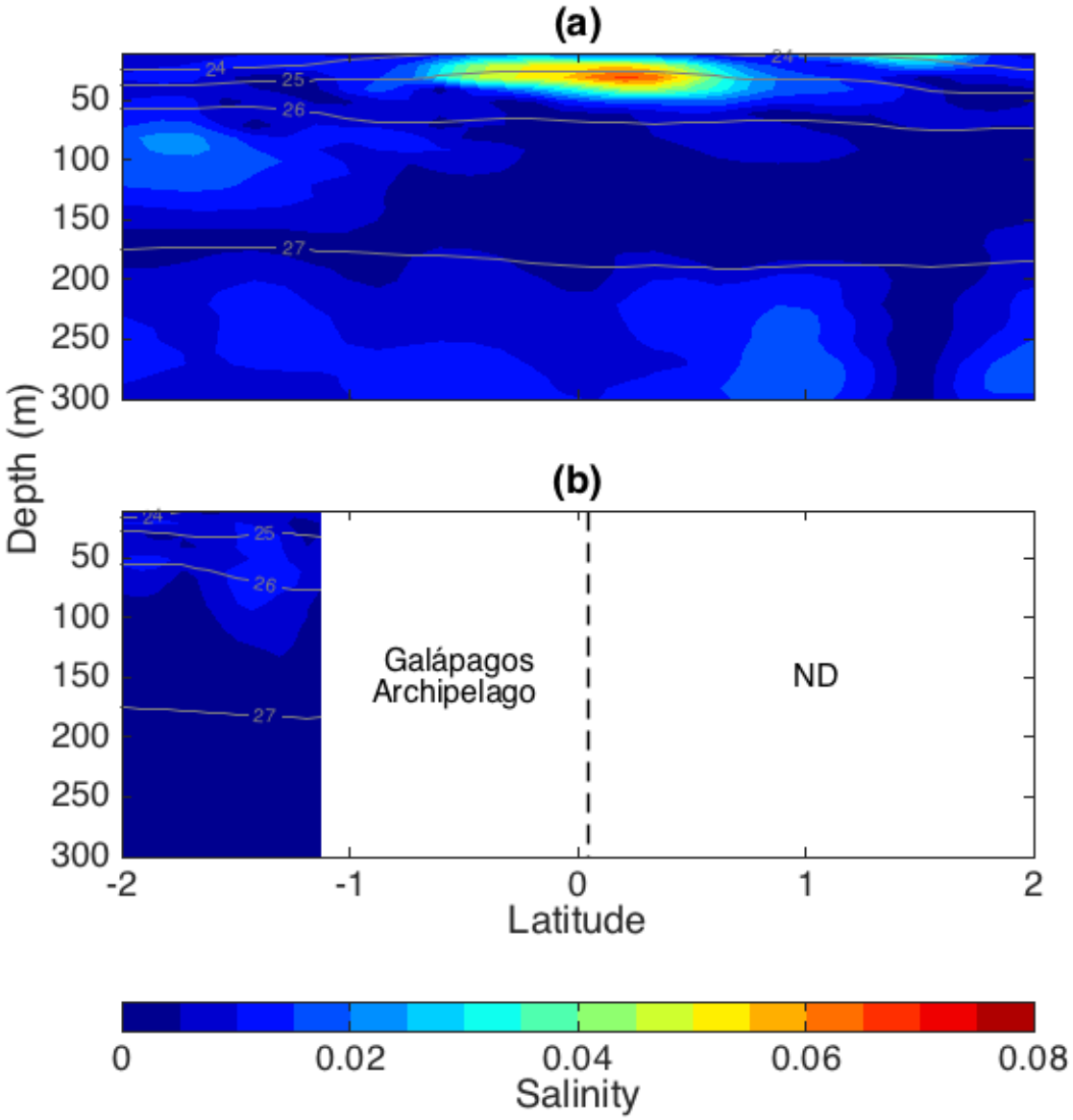

Figure 1-16: Estimated standard error of time average salinity along (a) 93W and (b) ND and SD.

THIS PAGE INTENTIONALLY LEFT BLANK

Chapter 2

Potential Vorticity and Bifurcation of the Equatorial Undercurrent West of the Galápagos Archipelago

Abstract

The Galápagos Archipelago lies on the equator in the path of the eastward flowing Pacific Equatorial Undercurrent (EUC). On average, the EUC is centered south of the equator near 0.5°S. When the EUC reaches the Galápagos Archipelago, it bifurcates into two branches that flow north and south around the archipelago at a latitude determined by the topography of the Galápagos Archipelago. *Pedlosky* (1987a) used a 2.5-layer, inertial model, where potential vorticity and the Bernoulli function are conserved along streamlines, to explain the existence of an eastward flowing EUC. Strong velocity gradients associated with the EUC core exist within 2° latitude of the equator. Since the Coriolis parameter approaches zero at the equator, these strong velocity gradients can result in Ertel potential vorticity (EPV) having sign opposite that of the Coriolis parameter near the equator and conditions conducive to inertial and/or symmetric instability. Changes in sign of the horizontal gradient of EPV indicate whether necessary conditions are met for barotropic and/or baroclinic instability associated with the equatorial current system. A fleet of autonomous, underwater gliders, deployed just west of the Galápagos Archipelago between 2°S – 2°N along 93°W and between 2°S and the southernmost point of Isla Isabela from 2013 – 2016 collected a unique set of temperature, salinity, and velocity observations, providing the opportunity to estimate sections of potential vorticity and Bernoulli function. EPV and the Bernoulli function are qualitatively conserved along streamlines. EPV having sign opposite of the Coriolis parameter is advected south of the Galápagos Archipelago when the EUC core is located south of the bifurcation latitude. EPV estimates are used to investigate whether the EUC is susceptible to various instability processes. The horizontal gradient of EPV suggests that the region between 2°S and 2°N above 100 m is unstable to barotropic instability, while limited regions are baroclinically unstable. Conditions conducive to inertial and symmetric instabilities are observed between the EUC core and the equator and within the south branch

of the EUC. E-folding timescales are between 2 – 13 days from two-month and three-year averages, suggesting inertial and symmetric instabilities can persist on those timescales.

2.1 Introduction

The Pacific Equatorial Undercurrent (EUC), initially observed by *Cromwell et al.* (1954) and *Knauss and King* (1958), is a coherent, eastward current very near the equator at the depth of the thermocline that flows across the Pacific Ocean (e.g., *Knauss and King*, 1958; *Wyrtki*, 1974; *Johnson et al.*, 2002). The EUC has been studied extensively using observational (e.g., *Knauss*, 1959; *Lukas and Firing*, 1984; *Johnson et al.*, 2001, 2002; *Leslie and Karnauskas*, 2014) and theoretical/numerical approaches (e.g., *Fofonoff and Montgomery*, 1955; *Pedlosky*, 1987a; *Johnson and Luther*, 1994; *Qiao and Weisberg*, 1996). *Pedlosky* (1987a) estimated eastward, equatorial flow consistent with the EUC using a 2.5-layer, inertial model, in which potential vorticity and the Bernoulli function are conserved along streamlines. The average position of the EUC core (region of maximum eastward velocity of the EUC) is near 0.5°S with a maximum velocity of approximately 1 m s^{-1} near 95°W (*Johnson et al.*, 2002).

The Galápagos Archipelago, with a meridional extent of 1.1°S – 0.25°N, lies directly in the path of the EUC in the eastern equatorial Pacific (Chapter 1). The interaction of the EUC with the topographic barrier of the Galápagos Archipelago produces a region of anomalously cold sea surface temperature (SST) just west of the islands known as the Galápagos Cold Pool (*Karnauskas et al.*, 2007; *Jakoboski et al.*, 2019) that exists in part due to upwelling of the EUC. The path of the EUC as it reaches the Galápagos Archipelago has been observed previously, primarily relying on shipboard observations (e.g., *Christensen*, 1971; *Lukas*, 1986; *Karnauskas et al.*, 2010). The 'Repeat Observations by Gliders in the Equatorial Region' (ROGER) program deployed a fleet of autonomous underwater gliders in the region between 93°W and the Galápagos Archipelago to obtain high resolution observations of current velocity, temperature, salinity, and depth just west of the Galápagos Archipelago (the region of the GCP) over a period of three years. Chapter 1 described the bifurcation of the EUC into two branches around the northern and southern boundaries of the Galápagos Archipelago and upwelling shallower than the core of the EUC.

Strong velocity gradients exist between the EUC core and surrounding waters. The velocity gradient between the eastward EUC and the westward, surface intensified South Equatorial Current (SEC) is particularly large (*Johnson et al.*, 2002; *Kessler*, 2006). These

velocity gradients near the equator can result in Ertel potential vorticity (EPV, Q) having sign opposite to that of the Coriolis parameter (f). EPV (*Ertel*, 1942; *Schubert et al.*, 2004) is a dynamically active tracer that is conserved in adiabatic and inviscid flows, but modified by buoyancy and frictional forcing, defined as

$$Q = -\frac{2\vec{\mathbf{\Omega}} + \vec{\zeta}}{\rho} \cdot \nabla \rho_\theta \tag{2.1}$$

where $\vec{\mathbf{\Omega}}$ is the earth's rotation vector, $\vec{\zeta}$ is relative vorticity (Equation 2.5), ρ is seawater density, and ρ_θ is potential density. In the absence of heat and friction in the ocean interior, EPV is a materially conserved property along streamlines (*Gill*, 1982), as in the inertial model of *Pedlosky* (1987a). *Pedlosky* (1987a) also assumes the Bernoulli function is conserved along streamlines in a steady-state ocean. The Bernoulli function is defined as

$$B = \frac{u^2 + v^2}{2} + \frac{p}{\rho_0} + \frac{\rho g z}{\rho_0} \tag{2.2}$$

from the steady-state, shallow water equations (*Cushman-Roisin and Beckers*, 2011). In the inertial, steady-state ocean of *Pedlosky* (1987a), we expect both EPV and B to be conserved along streamlines that connect the EUC west of the Galápagos Archipelago and the two branches of the EUC as they flow around the archipelago.

Without a velocity gradient, EPV will be the same sign as the Coriolis parameter (*Gill*, 1982). Prior to bifurcation of the EUC, EPV with sign opposite to the Coriolis parameter may exist due to the average meridional position of the EUC core with respect to the equator. If the bifurcation latitude of the EUC is determined topographically by the existence of the Galápagos Archipelago, EPV with sign opposite of f associated with the EUC core would be advected further poleward by the branches of the EUC around the archipelago.

A range of instabilities associated with the average EPV field can exist in the equatorial region. Tropical Instability Waves (TIWs) have been widely considered to be a result of baroclinic instability, barotropic instability, or a combination of both resulting from shear within the equatorial current system (e.g., *Philander*, 1976, 1978; *Yu et al.*, 1995; *Proehl*, 1998; *Lyman et al.*, 2005, 2007; *Farrar*, 2011). Baroclinic instability is maintained by potential energy associated with density gradients resulting from vertical shear, while barotropic instability is the result of horizontal shear (*Pedlosky*, 1987b). In a quasi-geostrophic fluid, a change in sign of the cross-flow gradient of EPV in the vertical plane is a necessary condition

for baroclinic instability (*Pedlosky*, 1987b; *Gill*, 1982; *Cushman-Roisin and Beckers*, 2011). Barotropic instability requires a change in sign of the cross-flow gradient of absolute vorticity in the horizontal plane, which is approximately equivalent to a horizontal change in sign of the cross-flow gradient of EPV for a stably stratified fluid. While baroclinic instability tends to be suppressed at the equator for eastward flows, due to the β-effect (where β is the meridional gradient of the Coriolis parameter), sufficiently high vertical shears may result in instability (*Philander*, 1976).

Smaller scale instabilities, including gravitational, inertial, symmetric, and Kelvin-Helmholtz instability, are possible sources of mixing that may impact the anomalously cold SST of the GCP. Potential vorticity with sign opposite of the Coriolis parameter can result in combinations of three types of instability (adapted from *Thomas et al.*, 2013):

1. Gravitational: unstable stratification ($N^2 < 0$) results in vertical overturning

2. Symmetric: strongly baroclinic fluid with $N^2 > 0$, EPV with sign opposite to f is primarily due to large vertical shear compared to horizontal shear, resulting in along-isopycnal stirring

3. Inertial: the contribution to EPV by the sum of the vertical component of relative vorticity and planetary vorticity has the opposite sign of f (large horizontal shear) with $N^2 > 0$, resulting in horizontal stirring

where

$$N^2 = -\frac{g}{\rho}\frac{\partial \rho}{\partial z}. \tag{2.3}$$

Where EPV with sign opposite to the Coriolis parameter persists, the flow is unstable to gravitational, inertial, or symmetric instabilities, or combinations of these, depending on the local flow characteristics (*Thomas et al.*, 2013). *Stevens* (1983) showed that an eastward jet located slightly off of the equator results in a region of EPV with sign opposite of f between the core of the jet and the equator, supporting the possibility of instability associated with the average meridional position of the EUC. In the case where conditions conducive to both symmetric and inertial instability exist, inertial instability dominates where horizontal shear is large compared to vertical shear. Symmetric instability dominates in the opposite case.

Kelvin-Helmholtz instability (*Thomson*, 1871; *Helmholtz*, 1868) is an inertial instability that arises when the vertical gradient of horizontal velocity is sufficiently strong to result in

mixing despite the presence of stratification. Kelvin-Helmholtz instability extracts energy from the mean shear flow when the gradient Richardson number (Ri) is less than 1/4 (*Kundu et al.*, 2015), where

$$Ri = \frac{N^2}{(\partial u/\partial z)^2 + (\partial v/\partial z)^2}. \tag{2.4}$$

In regions of high vertical shear, Kelvin-Helmholtz instability can result in vertical mixing on timescales faster than those typical of inertial or symmetric instabilities in the region surrounding the EUC (*Smyth et al.*, 2013).

While *Gouriou and Toole* (1993) estimated EPV from shipboard hydrographic and current measurements in the western Pacific and resolve some regions of negative EPV north of the equator (EPV opposite sign of f), few studies consider equatorial EPV and its implications for instability. Conditions conducive to instability may result from the average meridional position of the EUC core slightly south of the equator in the central and eastern equatorial Pacific, and the associated bifurcation of the EUC around the topographic barrier of the Galápagos Archipelago. Concurrent observations of horizontal current velocity, temperature, and salinity as a function of depth and distance from ROGER gliders provide observations used to estimate EPV and Bernoulli function sections between 2°S and 2°N with very high spatial and temporal resolution. Since horizontal velocity is directly measured by the gliders, the need to estimate velocity from geostrophy is eliminated, and allows us to resolve the velocity field at the equator where geostrophy does not hold. The resulting EPV and Bernoulli function fields provide insight into the wide-range of equatorial dynamics that exist in the region just west of the Galápagos Archipelago with unprecedented resolution.

The following analyses consider advection of EPV and the Bernoulli function around the Galápagos Archipelago by the two branches of the EUC (Chapter 1) and the potential for instability associated with the EUC. In Section 2.2, we describe the glider observations obtained during the ROGER program and the methods used to estimate EPV and the Bernoulli function from those observations. Section 2.3 describes a sample glider transect, the major features of average potential vorticity and Bernoulli function sections, advection of potential vorticity and the Bernoulli function around the Galápagos Archipelago, mechanisms behind regions of high or "wrong-signed" potential vorticity, and possible resulting instabilities. Section 2.4 reiterates the main findings of the preceding sections.

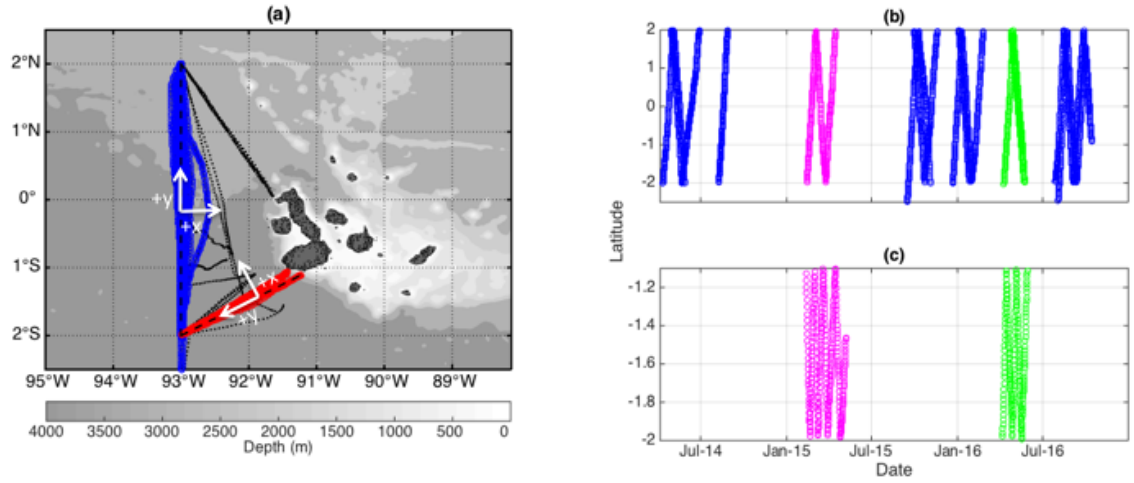

Figure 2-1: (a) Glider transects along 93W (blue) and SD (red) used in the analysis, with all ROGER transects (black) and local coordinate systems for 93W and the SD (white). (b,c) Latitude-time plots of transects along (b) 93W and (c) SD during 11 April 2014 – 13 October 2016 (TP1, blue), 11 February 2015 – 7 May 2015 (TP2, magenta), and 6 April 2016 – 31 May 2016 (TP3, green). TP1 includes data from TP2 and TP3.

2.2 Observations and Methods

2.2.1 Glider Observations West of the Galápagos Archipelago

A fleet of Spray gliders (*Sherman et al.*, 2001; *Rudnick et al.*, 2016) from the Repeat Observations by Gliders in the Equatorial Region (ROGER) program measured profiles of temperature, salinity, and absolute horizontal currents in the region between 93°W and the Galápagos Archipelago from January 2013 to December 2016 (Figure 2-1). During a total of 19 missions, gliders sampled along three survey lines: 1) 93°W from 2°N to 2°S (hereafter referred to as 93W), 2) the southern diagonal (SD), between 93°W, 2°S and the southwestern corner of Isla Isabela, and 3) the northern diagonal. Along the northern diagonal, only a single, one-week-long CTD transect is available due to instrument failure; ND is not included in the analysis due to anomalous velocity observations during that transect. A total of 15 missions from 11 April 2014 – 13 October 2016 along 93W and SD are used in the following analysis; these missions had high quality velocity measurements necessary for EPV and Bernoulli function estimation.

Each glider was equipped with a Sea-Bird SBE 41CP conductivity-temperature-depth sensor (CTD), a Seapoint chlorophyll fluorometer, and a 1-MHz Nortek AD2CP Doppler current profiler (*Todd et al.*, 2017). Instruments sampled during the ascending portion of

Table 2.1: Dates and number of glider transects that descended to 1000 m during TP1, TP2, and TP3. SD transects are not used for TP1 analyses.

Time Period	Begin Date	End Date	No. W93 Transects	No. SD Transects
TP1	11 April 2014	13 October 2016	27	(20)
TP2	11 Feb 2015	07 May 2015	3	8
TP3	06 April 2016	29 May 2016	3	5

each dive with horizontal spacing between profiles of 5 km, from the surface to 1000 m depth. CTD and flourometer observations were averaged into 10 m vertical depth bins. Profiles of current velocity with 10 m vertical resolution were calculated via dead-reckoning methods of *Todd et al.* (2017) with minor updates as described in Chapter 1. Velocity error is estimated in Chapter 1, with maximum values less than 0.1 m s^{-1}. After calibration at Sea-Bird, laboratory checks prior to deployment, and post-mission quality control, remaining temperature and salinity observations are highly accurate with small error relative to the desired signal (*Rudnick and Cole*, 2011).

Individual transects along 93W were occupied in about three weeks, while transects along SD were occupied in about one week (e.g., Figure 2-2). Velocity, temperature and salinity transects resolve the major features of the equatorial current system and show relatively low variability below $\sigma = 26.5$ kg m^{-3} or 300 m depth (Chapter 1). This analysis focuses on the region above $\sigma = 26.5$ kg m^{-3} (average depth of 310 m over all 93W and SD transects).

After quality control, data were gridded onto a 15 km horizontal grid along each section using a Gaussian weighted average, as in Chapter 1, and linearly interpolated from depth surfaces onto potential density surfaces. The Gaussian scale of 30 km (Chapter 1) is chosen to remove horizontal variability due to high-frequency processes (e.g., internal waves) resulting from the finite sampling speed of the gliders (Rudnick and Cole, 2011). Average sections are calculated for three time periods (Table 2.1): the full time period of 11 April 2014 – 13 October 2016 (TP1), 11 Feb 2015 -âĂŞ 7 May 2015 (referred to as TP2), and 6 April 2016 -âĂŞ 31 May 2016 (TP3). The 93W and SD sections were simultaneously occupied during TP2 and TP3 (Figure 2-1), while TP1 only includes data along 93W.

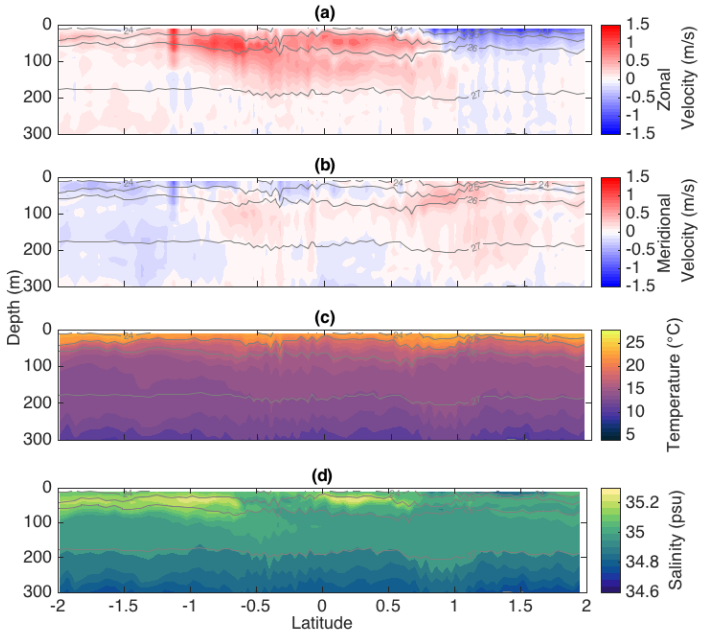

Figure 2-2: (a) Sections of zonal velocity, (b) meridional velocity, (c) potential temperature, and (d) salinity as a function of depth in the upper 300 m from one transect along 93W from 29 April 2016 to 23 May 2016. Potential density (kg m^{-3}) contours are shown in gray.

2.2.2 Potential Density on Depth and Density Surfaces

We estimate EPV (Equation 2.1) along 93W and SD using the coordinate systems in Figure 2-1a. Three-dimensional relative vorticity is defined by

$$\vec{\zeta} = \nabla \times \vec{\mathbf{v}} = \left(\frac{\partial w}{\partial y} - \frac{\partial v}{\partial z}, \frac{\partial u}{\partial z} - \frac{\partial w}{\partial x}, \frac{\partial v}{\partial x} - \frac{\partial u}{\partial y} \right)^T, \tag{2.5}$$

where $\vec{\mathbf{v}}$ is three-dimensional velocity. In the local (rotated) coordinate system for each line, u is the cross-line (normal) velocity in the x direction, v is along-line velocity in the y direction, and w is vertical velocity. The sign convention is positive into the volume V_{gl} (defined by area A_{gl}, the surface and 300 m depth) and positive upwards (Figure 2-1).

The earth's rotation vector, $2\vec{\mathbf{\Omega}}_G$, in the global coordinate system is

$$2\vec{\mathbf{\Omega}}_G = [0, f \cot\theta, f]^T \tag{2.6}$$

where $f = 2\Omega \sin\theta$, θ is latitude, and Ω is the rotation rate of the earth. The transformation of the earth's rotation vector into the local, rotated coordinate system of each line is achieved

via multiplying $2\vec{\mathbf{\Omega}}_G$ by the rotation matrix

$$\begin{bmatrix} \cos\phi & \sin\phi & 0 \\ -\sin\phi & \cos\phi & 0 \\ 0 & 0 & 1 \end{bmatrix} \tag{2.7}$$

where ϕ is the counterclockwise angle of rotation between east and the local x-axes of 93W ($\phi = 0°$) and SD ($\phi = 26.7°$) shown in Figure 2-1. The earth's rotation vector in the local coordinate system is then

$$2\vec{\mathbf{\Omega}}_L = [f\cot\theta\sin\phi, f\cot\theta\cos\phi, f]^T. \tag{2.8}$$

Combining Equations 2.5 and 2.8, the EPV (Equation 2.1) can be written in the coordinate system of 93W or SD with depth as the vertical coordinate:

$$Q_d = -\frac{1}{\rho}\left[\left(f\cot\theta\sin\phi + \frac{\partial w}{\partial y} - \frac{\partial v}{\partial z}\right)\frac{\partial\rho}{\partial x} + \left(f\cot\theta\cos\phi + \frac{\partial u}{\partial z} - \frac{\partial w}{\partial x}\right)\frac{\partial\rho}{\partial y} + \left(f + \frac{\partial v}{\partial x} - \frac{\partial u}{\partial y}\right)\frac{\partial\rho}{\partial z}\right] \tag{2.9}$$

Based on the vertical velocity estimates in Chapter 1, we assume vertical velocities (w) are small compared with horizontal velocities (u, v). Horizontal components of $2\vec{\mathbf{\Omega}}$ are small compared to vertical gradients of horizontal velocity (e.g., Figure 2-3e) and neglected. With these assumptions, EPV in depth coordinates simplifies to

$$Q_d = -\frac{1}{\rho}\left[-\frac{\partial v}{\partial z}\frac{\partial\rho}{\partial x} + \frac{\partial u}{\partial z}\frac{\partial\rho}{\partial y} + \left(f + \frac{\partial v}{\partial x} - \frac{\partial u}{\partial y}\right)\frac{\partial\rho}{\partial z}\right]. \tag{2.10}$$

We apply the chain rule to transform from depth coordinates to density coordinates. In density coordinates, Equation 2.10 simplifies to

$$Q_\rho = -\frac{1}{\rho}\left(f + \left.\frac{\partial v}{\partial x}\right|_\rho - \left.\frac{\partial u}{\partial y}\right|_\rho\right)\frac{\partial z}{\partial\rho}. \tag{2.11}$$

The first two terms of Equation 2.10 do not appear in the density coordinate equation (Equation 2.11) since horizontal gradients of velocity occur along isopycnals in the density coordinate framework.

As glider observations provide along-track measurements only, cross-track gradients are unresolved. We assume $\partial v/\partial x$ and $\partial\rho/\partial x$ are small compared to gradients in the y direction

of the local coordinate system, resulting in the final estimates of EPV used in this analysis:

$$Q_d = -\frac{1}{\rho}\left[\frac{\partial u}{\partial z}\frac{\partial \rho}{\partial y} + \left(f - \frac{\partial u}{\partial y}\right)\frac{\partial \rho}{\partial z}\right]. \tag{2.12}$$

in depth coordinates and

$$Q_\rho = -\frac{1}{\rho}\left(f - \left.\frac{\partial u}{\partial y}\right|_\rho\right)\frac{\partial z}{\partial \rho} \tag{2.13}$$

in density coordinates. Hereafter, when PV is expressed as a function of density or depth, horizontal derivatives are taken along isopycnals and depth surfaces, respectively. In Equation 2.13, the first term of Q_ρ is the contribution to Q_ρ by the vertical component of planetary vorticity, while the second term represents velocity shear along isopycnals.

Along 93W, the assumption that $\partial v/\partial x$ is small is supported by meridional velocities (v in the local coordinate system) having smaller magnitude than zonal velocities. Cross-track variability of density ($\partial \rho/\partial x$) is unknown. However, it multiples with $\partial v/\partial z$ (Equation 2.10), which is small compared to $\partial u/\partial z$ along 93W. Along SD, v contains both meridional and zonal velocity components. Assuming small $\partial v/\partial x$ and $\partial \rho/\partial x$ is likely a greater source of error along SD than 93W.

Isopycnal coordinates are used to examine the features of potential vorticity sections, which include high variability in the pycnocline where strong velocity gradients between the EUC and SEC exist. Since inertial, symmetric barotropic, and baroclinic instability are characterized based on horizontal and vertical gradients of velocity and density, depth coordinates are used to differentiate between types of instabilities.

2.2.3 Conditions for Inertial and Symmetric Instability

Growth rates of instabilities associated with EPV having sign opposite to the Coriolis parameter are estimated via

$$\omega^2 = \frac{-Q_d f g}{N^2} \tag{2.14}$$

using the methods of *Haine and Marshall* (1998) and *Kelly* (2016). To understand the types of instabilities that result when EPV is of sign opposite to that of f, we separate Q_d (Equation 2.12) into two terms, where $Q_d = Q_h + Q_v$:

$$Q_h = -\frac{1}{\rho}\left(\frac{\partial u}{\partial z}\frac{\partial \rho}{\partial y}\right) \tag{2.15}$$

and

$$Q_v = -\frac{1}{\rho}\left(f - \frac{\partial u}{\partial y}\right)\frac{\partial \rho}{\partial z} \tag{2.16}$$

Q_h represents the baroclinic contribution to Q_d by the horizontal component of the relative vorticity, while Q_v represents vertical contributions to Q_d by the vertical components of the planetary and relative vorticities.

Inertial instability dominates when Q_v (including horizontal shear) is primarily responsible for regions of EPV with sign opposite to f and Q_h is small relative to Q_v. In the case where $Q_h = 0$ (inertial instability with no symmetric instability) and given a stably stratified fluid, Equation 2.14 simplifies to

$$\omega_I^2 = f\,(f + \zeta) \tag{2.17}$$

where ζ is the vertical component of relative vorticity and ω_I^2 is the effective local inertial frequency (e.g., *Mooers*, 1975; *Stevens*, 1983). Inertial instability requires that $\omega_I^2 \leq 0$. If ζ is of greater magnitude than and of opposite sign of f, ω_I^2 is negative, and inertial instability is possible. Near the equator, f is near zero so that small horizontal shear can result in instability. Non-zero EPV on the equator or "wrong sign" EPV away from the equator dominated by horizontal shear is inertially unstable.

Symmetric instability requires that $fQ_d < 0$ and $fQ_h < 0$ and dominates over inertial instability when Q_h (vertical shear) is of larger magnitude than Q_v and has sign opposite to f (*Haine and Marshall*, 1998; *Thomas et al.*, 2013). The growth rate of symmetric instability is estimated by setting $\zeta = \partial u/\partial y = 0$ in Equation 2.14:

$$\omega_S^2 = f\frac{\partial u}{\partial z}\frac{\partial \rho}{\partial y}\left(\frac{\partial \rho}{\partial z}\right)^{-1} + f^2. \tag{2.18}$$

In the case where the fluid state is conducive to both inertial and symmetric instability ($fQ < 0$, $fQ_h < 0$, and $fQ_v < 0$), inertial and symmetric instability may both be present (*Thomas et al.*, 2013). To differentiate between regions of symmetric versus inertial instability, we consider the ratio of Q_h to Q_v. In regions where Q_h and Q_v both have sign opposite to f and Q_h is of larger magnitude than Q_v, vertical shear is large compared to horizontal shear and symmetric instability dominates. Where Q_v has larger magnitude than Q_h, "wrong sign" EPV is dominated by horizontal shear, resulting in inertial instability.

Following *Dunkerton* (1981) and *Stevens* (1983), we estimate the e-folding timescale of inertial and symmetric instabilities to be

$$\tau_n = \sqrt{\frac{1}{\omega_n}} \tag{2.19}$$

where n is either I (inertial instability) or S (symmetric instability).

2.3 Results

2.3.1 Sample Glider Transect

A representative sample transect of current velocity and hydrography (Figure 2-2) along 93W from 29 April 2016 to 23 May 2016 shows the major features of the equatorial current system above 300 m and $\sigma_0 = 26.5$ kg m^{-3} (Figure 1-3 of Chapter 1) includes the upper 1000 m for the same transect). The eastward EUC has maximum zonal velocity $O(1$ m s$^{-1})$ just south of the equator and extends from 1.25°S to 1°N within the thermocline near 50 m depth (Figure 2-2c), consistent with previous observations (e.g., *Wyrtki and Kilonsky*, 1984; *Johnson et al.*, 2002). The westward South Equatorial Current (SEC) exists north of the equator with a maximum zonal velocity of 0.75 m s^{-1} at the surface. The portion of the SEC observed by this section transports relatively fresh, warm water westward (Figures 2-2c and 2-2d). Meridional velocities are small compared to zonal velocities. At a depth of 50 m, a high salinity tongue extends northward into the EUC core from the southern boundary of the transect at 2°S (Figure 2-2d).

Spray glider observations of velocity, temperature, and salinity as a function of distance and depth provide estimates of EPV in the equatorial region with very high spatial resolution, resulting in the ability to observe detailed features of the EPV field. The corresponding sample transect of EPV in depth and density coordinates show generally positive (negative) EPV north (south) of 0.7°S (Figures 2-3a and 2-4a). The contribution to EPV by the vertical component of planetary vorticity (Figures 2-3b and 2-4b) changes sign and reaches a minimum (zero) at the equator corresponding to the magnitude and sign of f. Vertical structure is due to variations in the magnitude of N^2. The contribution to EPV by the vertical component of relative vorticity (Figures 2-3c and 2-4c) is generally positive (negative) north (south) of the EUC core, which is centered slightly south of the equator

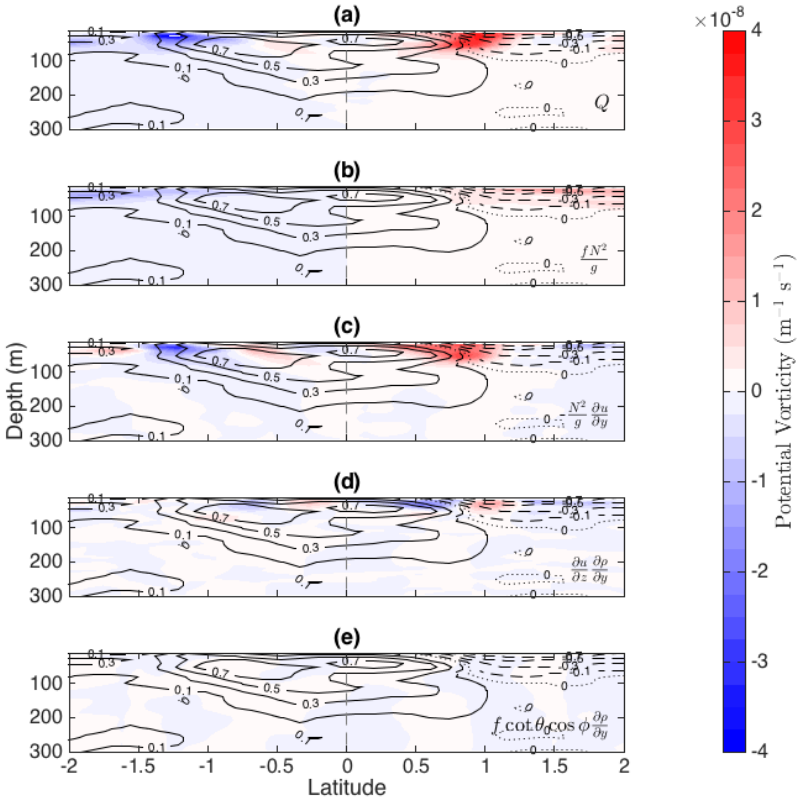

Figure 2-3: Latitude-depth sections of (a) EPV and the contributions to EPV by: (b) the vertical component of planetary vorticity, (c) the vertical component of relative vorticity, (d) the horizontal component of relative vorticity, and (e) the horizontal component of planetary vorticity in the upper 300 m from one transect along 93W from 29 April 2016 to 23 May 2016. Zonal velocity (m s^{-1}) is shown in black solid (positive), dashed (negative), and dotted (zero) contour. Gray, dashed, vertical line denotes the equator.

near 0.7°S. Regions of relative vorticity with sign opposite to that of the planetary vorticity exist within the SEC near $1.5 - 2$°N, south of the EUC core near $1.5 - 2$°S, and between the EUC core and the equator. Combined with the contribution to EPV by the vertical component of planetary vorticity, these result in regions of EPV with sign opposite of f near 1.75°N and between the EUC core and the equator. The feature near 1.75°N is likely due to transient variations in the EUC and SEC. Aside from small regions of "wrong-sign" EPV, a clear change in sign of EPV exists at the EUC core near 0.7°S.

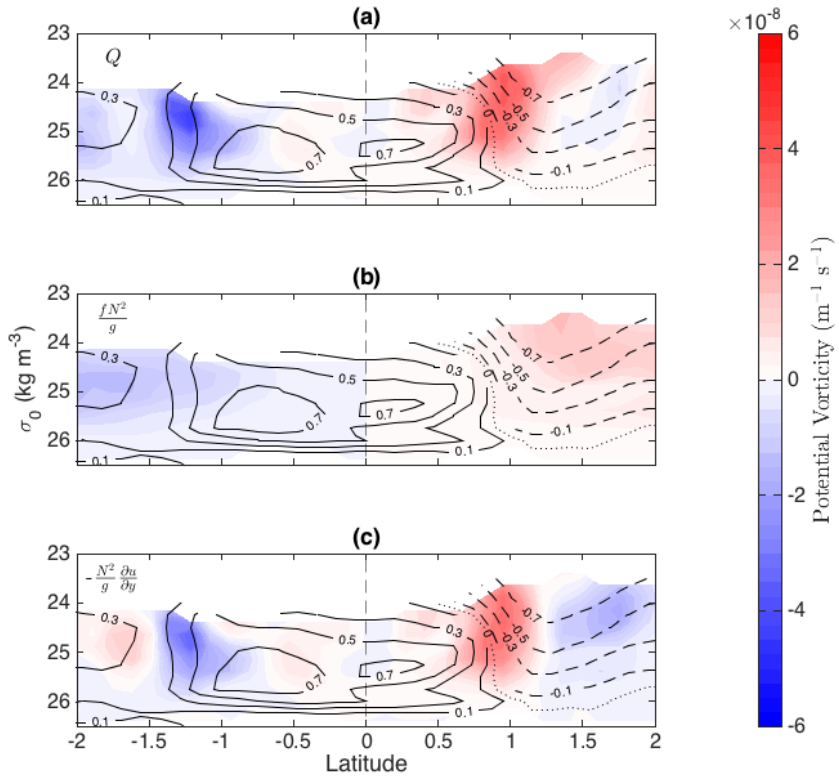

Figure 2-4: Latitude-potential density sections of (a) EPV and the contributions to EPV by: (b) vertical component of planetary vorticity and (c) relative vorticity above $\sigma_0 = 26.5$ kg m^{-3} from the same transect as in Figure 2-3. Zonal velocity (m s^{-1}) is shown in black solid (positive), dashed (negative), and dotted (zero) contour. The average depth of $\sigma_0 = 26.5$ kg m^{-3} during this transect is 275 m. Gray, dashed, vertical line denotes the equator.

2.3.2 Average Potential Vorticity

Long-Term Average (TP1)

We first calculate average potential vorticity along 93W for TP1 (11 April 2014 – 13 October 2016). Poleward of 0.5°S and 0.5°N, EPV has the same sign as f (Figure 2-5a). However, at densities of $\sigma_0 = 22 - 23$ kg m^{-3}, positive potential vorticity extends south of the equator as far as 0.5°S. This is due to the relative vorticity contribution to EPV (Figure 2-5c) resulting from the zonal velocity gradient between the surface SEC and underlying EUC. Between $\sigma_0 = 23.5$ kg m^{-3} and $\sigma_0 = 26.5$ kg m^{-3}, the position of the EUC core near 0.5°S results in region of positive EPV that extends south of the equator to 0.1°S.

Similar to the sample transect, a region of relative vorticity with sign opposite of f associated with the SEC exists near the surface and 1.5°N in the long term average (Figure 2-5c). Corresponding vorticity with sign opposite of f is not seen in the EPV section, since

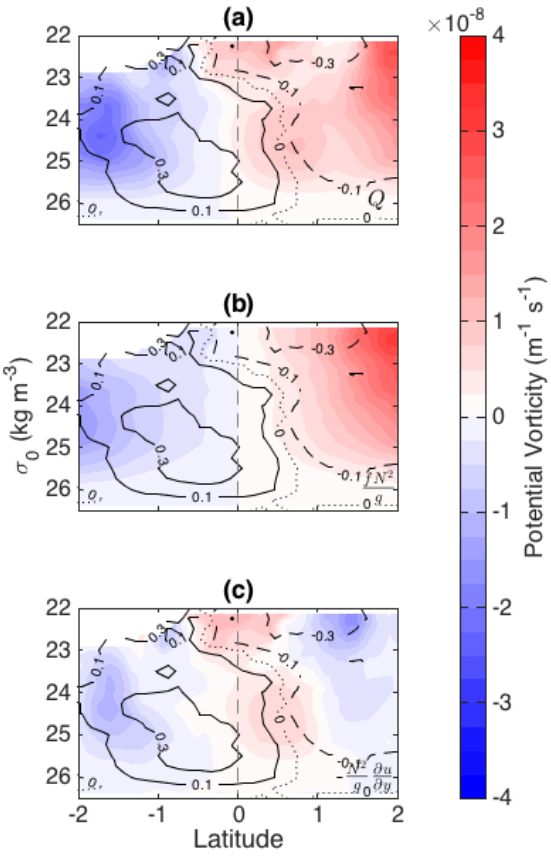

Figure 2-5: Average sections of (a) EPV and the contributions to EPV by: (b) vertical component of planetary vorticity and (c) relative vorticity over 11 April 2014 – 13 October 2016 (TP1) along 93W as a function of potential density. Zonal velocity (m s^{-1}) is shown in black solid (positive), dashed (negative), and dotted (zero) contour. Gray, dashed vertical line denotes the equator.

the vertical planetary vorticity contribution to EPV (Figure 2-5b) is strong near $\sigma_0 = 22.5$ kg m^{-3} and $\sigma_0 = 24.5$ kg m^{-3}, north and south of the equator, respectively.

Short Term Averages (TP2 and TP3)

During TP2 (85 days, 11 February 2015 – 7 May 2015) and TP3 (52 days, 6 April 2016 – 31 May 2016), both 93W and SD were occupied by gliders (Figure 2-1). Along 93W during both time periods, EPV is positive north of and negative south of the EUC core (Figures 2-6a and 2-7a) at the depth of the EUC. When the EUC core is located south of the equator, positive EPV exists just south of the equator above $\sigma_0 = 25.5$ kg m^{-3} during TP2 and TP3. The intrusion of positive potential vorticity south of the equator reaches 0.5°S and 0.7°S during TP2 and TP3, respectively. During TP3, the EUC core is centered near 0.7°S (Figures 2-7a

– 2-7c). During TP2, the EUC core is centered on the equator, with an extension southward above $\sigma = 24$ kg m^{-3} in the region where the EUC and SEC meet (Figures 2-6a – 2-6c). As the EUC core is centered south of the equator in the long-term average (TP1), positive EPV is seen south of the equator during all three time periods; however, the magnitude of this EPV with sign opposite of f is greater during TP2 and TP3.

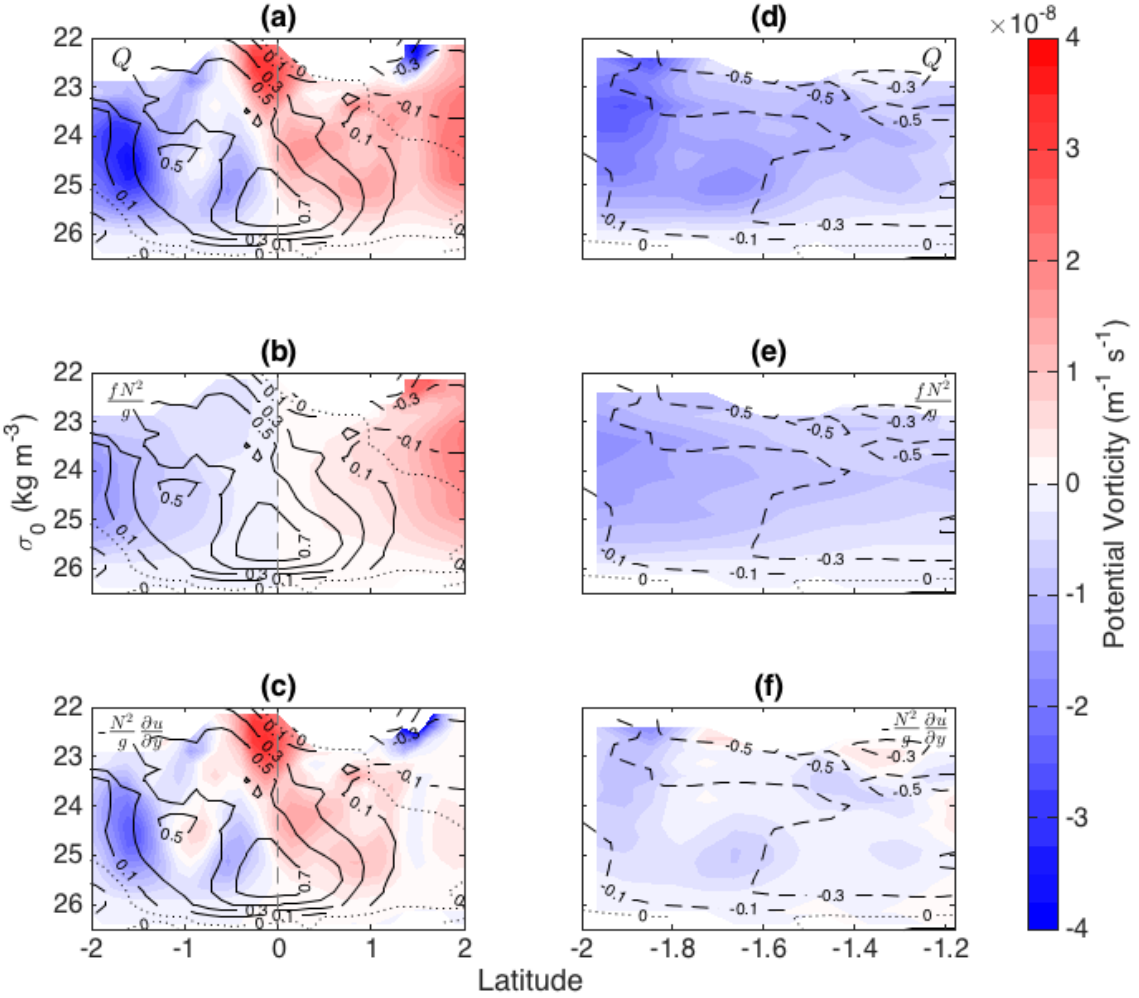

Figure 2-6: Average (a, d) EPV and the contributions to EPV by: (b, e) the vertical component of planetary vorticity and (c, f) relative vorticity for 93W (a – c) and SD (d – f) over 11 February 2015 – 7 May 2015 (TP2). Zonal velocity (m s^{-1}) is shown in black solid (positive), dashed (negative), and dotted (zero) contour. Gray, dashed vertical line denotes the equator.

During TP2 and TP3, the relative vorticity contribution to EPV is positive north of the EUC core with largest values near the surface (Figures 2-6c and 2-7c), where potential vorticity increases due to the vertical and meridional gradients of zonal velocity between

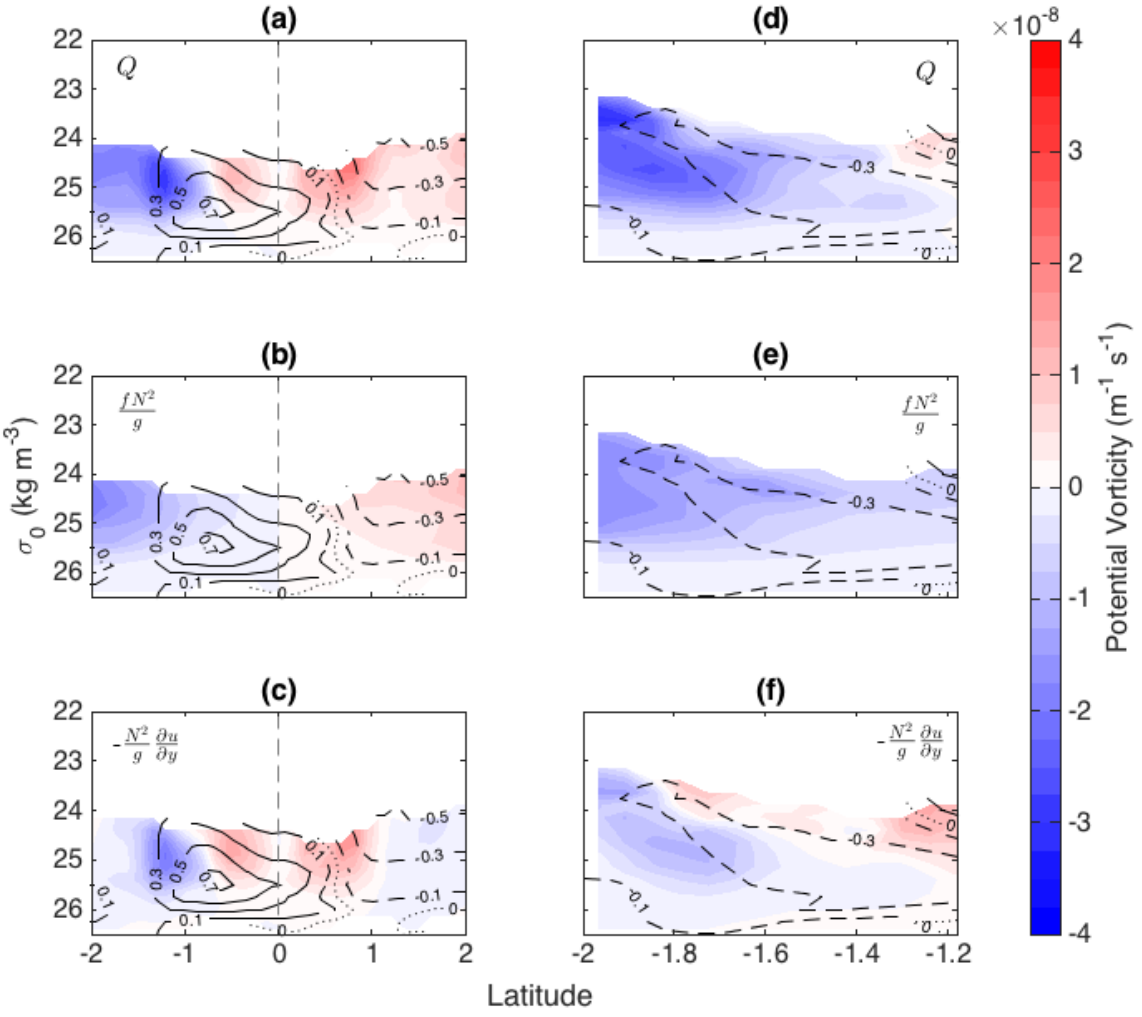

Figure 2-7: As in Figure 2-6, but averaged over 6 April 2016 – 31 May 2016 (TP3).

the eastward EUC and westward SEC and vertical density gradient associated with the thermocline (Figures 2-6c and 2-7c). Relative vorticity south of the EUC core is negative during TP2 (Figure 2-6c) and TP3 (Figure 2-7c), with the exception of a small region of positive vorticity associated with a local zonal velocity maximum south of the EUC core during TP2. This local maximum is likely a transient extension of the EUC core and is associated with near-zero EPV (Figure 2-6a). Combined with the vertical planetary contribution to EPV (Figure 2-6b) and TP3 (Figure 2-7b), the relative vorticity contribution to EPV results in positive EPV south of the equator between between the EUC and SEC during TP2 and the EUC core and the equator during TP3.

The SEC exists near the surface north of the equator and north of 0.5°N during TP2 and TP3, respectively. As in the sample transect and TP1, zonal velocity gradients associated

with the SEC result in negative relative vorticity (Figures 2-6b and 2-7b) near the surface at 1.5°N. The magnitude of this negative relative vorticity is small in TP3 (Figure 2-7c) compared with TP2 (Figure 2-6), due to differences in zonal velocity gradient. Although this feature is seen in the EPV section for TP2 (Figure 2-6a), we consider it a transient feature as it does not appear in TP3 (Figure 2-7a) or in the long-term average (Figure 2-5a).

Velocity normal to SD is southeastward (negative) during TP2 (Figures 2-6d – 2-6f) and TP3 (Figures 2-7d – 2-7f) with maximum magnitude near the southern boundary of the Galápagos Archipelago at 1.2°S. This region of relatively high velocity shoals with increasing distance southward from 1.2°S. Maximum southeastward velocity normal to SD is greater during TP2 (0.5 m s^{-1}) than TP3 (0.3 m s^{-1}), likely due to bifurcation of the stronger EUC around the archipelago during TP2 compared to TP3 (Figures 2-6a and 2-6d, 2-7a and 2-6d). EPV along SD is negative during TP2 and TP3 (Figures 2-6d and 2-7d), except immediately adjacent to the Galápagos Archipelago at 1.2°S during TP3. Positive EPV during TP3 is due to the relative vorticity contribution to EPV (Figure 2-7f) at $1.2 - 1.3$°S. This positive EPV is possibly a boundary effect as the EUC splits around the Galápagos Archipelago. During TP2, however, small regions of weak positive relative vorticity (Figure 2-6f) do not result in positive EPV across SD. If positive relative vorticity in TP3 is a boundary effect, it is not observed during TP2. Possible boundary effects include the generation of positive relative vorticity via interaction of the south branch of the EUC with topography (e.g., *Gula et al.*, 2015; *Molemaker et al.*, 2015) and/or the existence of strong cross-track gradients at the boundary with the Galápagos Archipelago, neglected here, that could minimize the apparent positive relative vorticity.

Branching of the EUC

The EUC bifurcates into a north and south branch around the Galápagos Archipelago between 93°W and the islands. Using salinity as a tracer, Chapter 1 estimated the latitude at which this split occurs ("bifurcation latitude") to be near 0.4°S during what is referred to here as TP3. Using the methods of Section 1.3.4, we estimate the bifurcation latitude based on volume transport as a function of salinity class to be 0.32°S during TP2, compared to the value of 0.40°S during TP3. The Bernoulli function (Equation 2.2, Figure 2-9) can also be used as a tracer to estimate the bifurcation latitude, since B is conserved in steady-

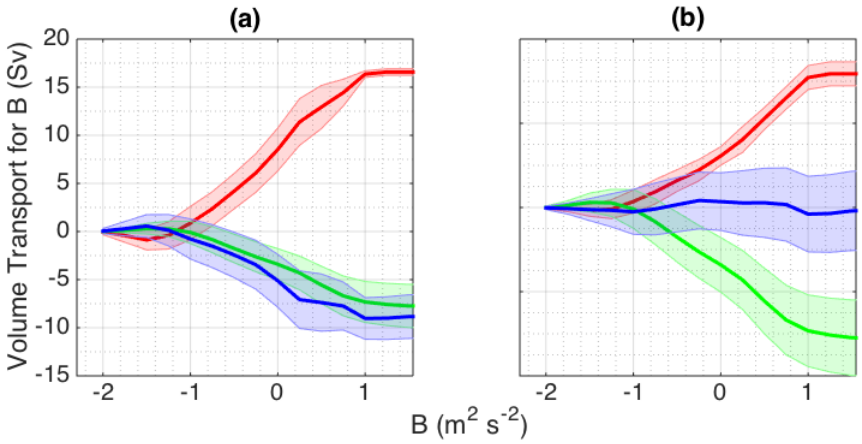

Figure 2-8: (a) Sample calculation of cumulative volume transport as a function of B for 93W (red) and SD (green) for TP2. Cumulative transport through ND is calculated as a residual due to the lack of CTD data. Shading shows standard errors per Section 1.3.4. Positive transport is into the control volume (V_{gl} in Section 1.3.4). (b) As in (a), but for transport through 93W only south of 0.23°S.

state, inviscid, adiabatic flow. Again using methods similar to that of Section 1.3.4 but for B instead of salinity, we estimate the bifurcation latitude based on volume transport as a function of B to be 0.23°S (Figure 2-8) and 0.33°S for TP2 and TP3, respectively.

Estimates of bifurcation latitude do not resolve vertical variability in the bifurcation of the EUC. Further, the Bernoulli function is only conserved along streamlines in a steady-state flow. Error in the bifurcation latitude estimate is apparent as the residual flow along ND is minimized, but does not reach zero in individual classes of salinity or B (Figure 2-8b). In salinity or B classes where the residual is particularly large, it is likely that the bifurcation latitude at the depth where that salinity or B class dominates is slightly different from the average bifurcation latitude. In Figure 2-8b, transport along ND reaches zero in the $B < 0$ m^2 s^{-2} class (the B class with maximum residual) if the bifurcation latitude is changed to 0.18°S from 0.23°S, suggesting that the bifurcation latitude during TP2 varies approximately 0.1° latitude in the upper 300 m.

As the meridional center of the Galápagos Archipelago is located near 0.4°S and the average meridional position of the EUC core is centered near 0.5°S (*Johnson et al.*, 2002) as it reaches the archipelago, it is likely that the bifurcation of the EUC into two branches is primarily topographically driven by the position of the Galápagos Archipelago. The average position of the EUC is located slightly south of the equator due to the predominantly south-easterly direction of the trade winds in the eastern equatorial Pacific (*Charney and Spiegel*,

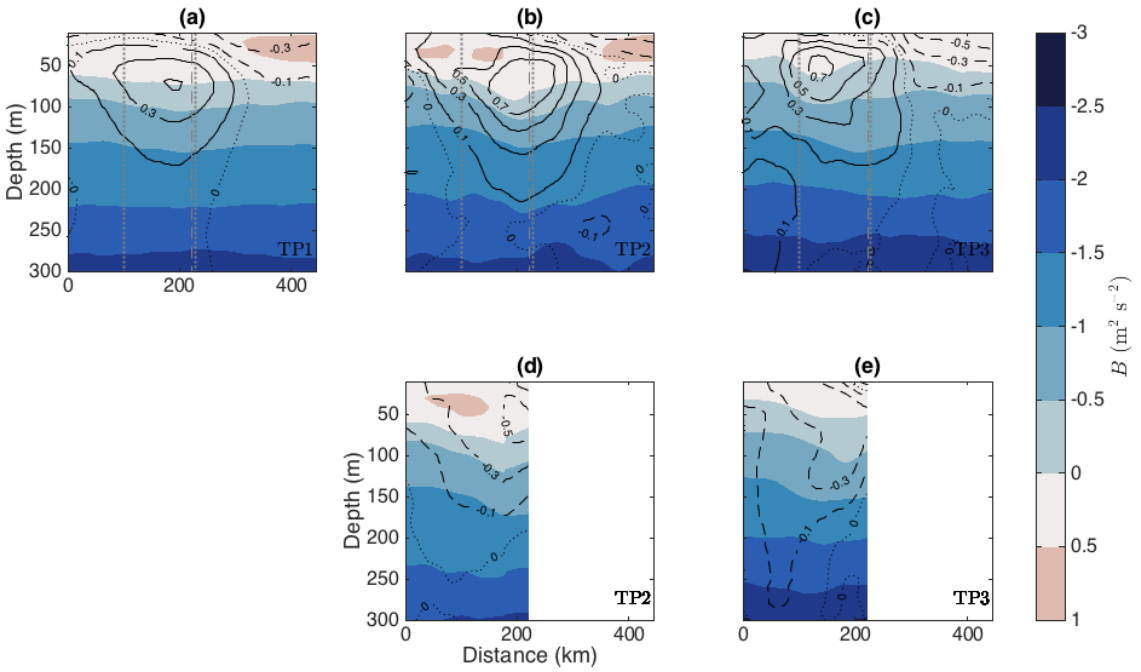

Figure 2-9: Average Bernoulli function along 93W (a – c) and SD (d, e) over (a) TP1, (b, d) TP2, (c, e) TP3 as a function of distance from the point (93°S, 2°S) along each survey line, in order to maintain consistency between x-axis scales for 93W and SD. Zonal velocity (m s^{-1}) is shown in black solid (positive), dashed (negative), and dotted (zero) contour. Vertical, dotted gray lines (a – c) denote the meridional extent of the Galápagos Archipelago and dashed, gray line the equator.

1971; *Yu et al.*, 1997; *Kessler et al.*, 1998). The EUC core meanders about it's average position on interannual, seasonal, and shorter timescales (*Johnson et al.*, 2002). Based on these results and those of Chapter 1, increased EUC-related flow passes south (north) of the Galápagos Archipelago when the EUC core is positioned further south (north) of the bifurcation latitude.

Using Spray glider observations, we are able to resolve the latitude at which EPV changes sign near the equator with high spatial resolution. To compare the bifurcation latitude with the latitude at which EPV changes sign along 93W (Figures 2-10a – Figures 2-10c), the latter is calculated at each depth level. The depth-averaged ($0 - 300$ m) latitude of the change of sign of EPV for each time period is 0.39°S for TP1, 0.25°S for TP2, and 0.64°S for TP3. These latitudes are approximately consistent with the location of the EUC core along 93W for each time period. During TP2, the EUC is located near the equator and velocity gradients that result in positive EPV south of the equator are limited to the region north of 0.25°S (Figure 2-10b). During TP3, the EUC core is located near 0.70°S, resulting

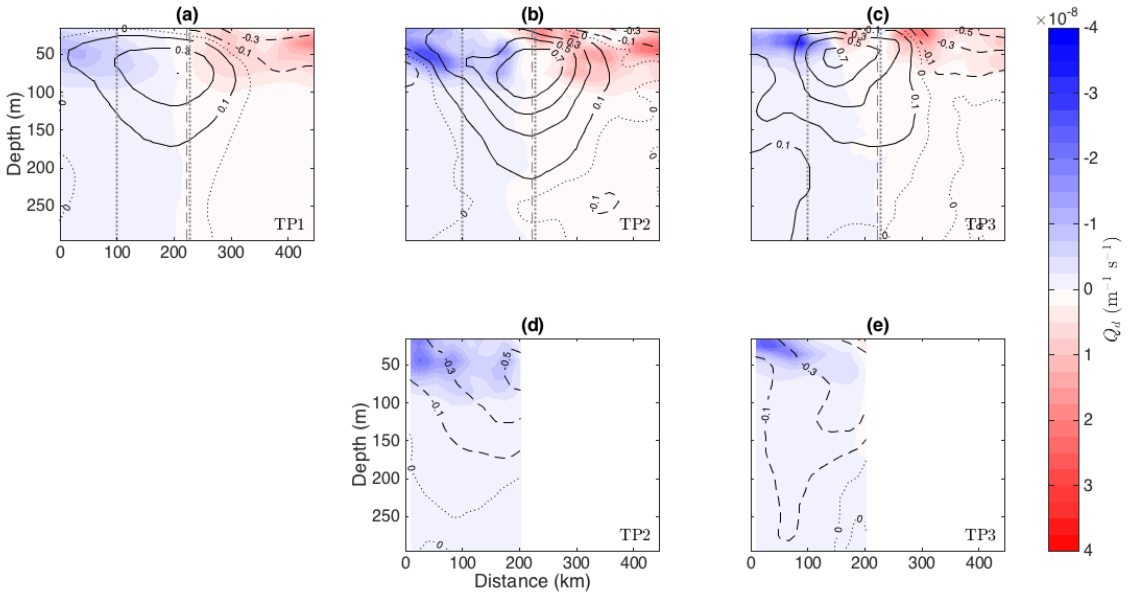

Figure 2-10: As is Figure 2-9, but for average EPV.

in a change from negative to positive EPV located further south (Figure 2-10c) than during TP2. The long-term average (TP1) change in sign is near 0.40°S (Figure 2-10a), consistent with the estimate of bifurcation latitude made in Chapter 1 using transport as a function of salinity class.

Along SD during TP2, no positive EPV is evident (Figure 2-10d) since along 93W, the change of sign of EPV is 0.25°S and positive EPV does not extend past the bifurcation latitude of 0.23°S – 0.32°S (Figure 2-10b). During TP3, a region of positive EPV along SD exists near the boundary with the Galápagos Archipelago, corresponding with the more southerly position of the EUC core (Figure 2-10e). Along 93W during this time, the latitude of change of sign of EPV is 0.64°S with positive EPV extending southward of the bifurcation latitude of 0.33°S – 0.4°S for TP3 (Figure 2-10c). Since EPV is conserved along streamlines in an adiabatic, inviscid flow, EPV south of the bifurcation latitude is advected south of the archipelago. In the case where the latitude at which EPV changes sign is south of the bifurcation latitude (Figure 2-10), positive EPV is advected across SD.

2.3.3 Conservation of EPV and the Bernoulli Function

The 2.5-layer, inertial model of *Pedlosky* (1987a) produces an EUC-like equatorial flow, neglecting friction in the shallow-water equations of motion. As a consequence, it is assumed

that both EPV and the Bernoulli function (B) are conserved in a steady-state ocean. Conservation of these quantities is a general property of ideal flow that extends beyond a layered model to an inviscid, adiabatic, stratified ocean (*Cushman-Roisin and Beckers*, 2011). In this study, high-resolution Spray glider observations of velocity, temperature, and salinity provide sections of EPV and B along 93W and SD in order to examine if EPV and B are conserved between the two survey lines.

Sections of EPV for TP2 – TP3 along 93W and SD (Figure 2-10) qualitatively show the conservation of notable features in the EPV field along streamlines between 93W and SD. Features south of the bifurcation latitude along 93W appear along SD during TP2 (Figures 2-10b and 2-10d) and TP3 (Figures 2-10c and 2-10e), consistent with Section 2.3.2. Two local minima in EPV south of the equator during TP2 and the single minimum near 100 km during TP3 are also seen along SD during the respective time periods.

Similarly, sections of Bernoulli function for TP2 – TP3 (Figure 2-9) also show qualitative conservation of B along streamlines. Positive B greater than 0.5 $m^2\ s^{-2}$ along 93W during TP2 is also seen along SD near 50 m depth. The deepening of the $B = 0\ m^2\ s^{-2}$ contour in the region of the EUC core is also apparent along both 93W and SD. During TP3, this deepening occurs farther south along 93W compared to TP2, but as the bifurcation latitude is also farther south, these features are apparent near the same distance along SD. The consistency of patterns in B and EPV between 93W and SD is qualitative evidence that these properties are conserved along streamlines between 93W and SD.

We do not expect conservation of EPV and B near the surface, where surface forcing plays a role in the form of wind-stress and heat exchange. The mixed layer depth in this region is very shallow, ranging from 10 – 30 m (*Boyer et al.*, 2013), and may not be resolved by the gliders. It is also possible that EPV and B are not conserved near the boundary with the Galápagos Archipelago. In sections of B, there is little evidence of a boundary layer, which also may be unresolved, as the gliders do not observe the 5 km closest to shore along SD. Lastly, the Bernoulli function is conserved in a steady-state, ideal fluid. The averages of Figure 2-9 include time variability that occurs during the transit between 93W and SD on a range of scales. Despite these potential sources of error, B and EPV sections during TP2 and TP3 are consistent with the inertial model of (*Pedlosky*, 1987a).

2.3.4 Equatorial Instability

Spray glider observations provide a unique opportunity to examine instabilities associated with the average EPV field within 2° latitude of the equator. The gradient of EPV and it's relationship to necessary conditions for baroclinic and barotropic instability are considered possible mechanisms driving TIW propagation. In addition to upwelling of the EUC (Chapter 1), smaller scale instabilities, including inertial, symmetric, and Kelvin-Helmholtz instability, are possible sources of mixing that may impact the anomalously cold SST of the GCP. The following sections consider the possibility of these instabilities in this region and their dynamical implications.

Barotropic and Baroclinic Instability

The change of sign of the horizontal gradient of EPV within the interior of a fluid is a necessary condition for barotropic or baroclinic instability in a quasi-geostrophic fluid. A change in sign of $\partial Q/\partial y$ in the vertical plane is a necessary condition for baroclinic instability, while changes in sign in the horizontal plane are indicative of barotropic instability in a stably stratified fluid (*Gill*, 1982; *Pedlosky*, 1987b). While quasi-geostrophic theory assumes the Rossby number is small, which is expected to be invalid in the region surrounding the EUC, quasi-geostrophy has been used to resolve instabilities that are consistent with equatorial observations (e.g., *Philander*, 1976, 1978) and will be applied here.

Sections of the along-line gradient of EPV are generally characterized by clear alternating vertical bands of positive and negative EPV along 93W during TP2 and TP3 above 100 m (Figures 2-11b and 2-11c), suggesting conditions conducive to barotropic instability. The long-term mean (Figure 2-11a) is dominated by same-sign (negative) $\partial Q/\partial y$, with no sign changes in the vertical plane. A weak sign change in the horizontal plane is apparent above 60 m near 300 km, where the EUC and SEC meet, indicating the potential for barotropic instability over the two-year average. During TP2, 93W and SD sections contain regions where $\partial Q/\partial y$ changes sign in the vertical direction, indicating possible conditions conducive to baroclinic instability, while little to no change of sign of $\partial Q/\partial y$ in the vertical plane is apparent during TP3. Vertical changes in sign are less pronounced than horizontal changes in sign during all time periods, where clear sign changes occur approximately every 50 km above 100 m during TP2 and TP3.

Philander (1976) showed that the EUC is stable to baroclinic instability using a quasi-geostrophic model, primarily due to the β-effect, except during periods when the EUC is at a seasonal maximum. Glider observations show that $\partial Q/\partial y$ meets the necessary condition for baroclinic instability during TP2 when the EUC is strong, but not during TP3 when the EUC is comparatively weaker, consistent with the results of *Philander* (1976). The change is sign of $\partial Q/\partial y$ in the horizontal plane during TP1 near 300 km (1°N) supports the conclusions of *Proehl* (1998) that TIWs are the result of barotropic instability arising from horizontal shear between the EUC and SEC. Changes in sign of $\partial Q/\partial y$ from glider observations during TP1 – TP3 suggest that the equatorial current system within 2° latitude of the equator is generally unstable to barotropic instability, while the necessary condition for baroclinic instability may be met when the EUC is strong. However, TIWs are observed outside the meridional bounds of this study (2°S – 2°N, e.g., *Farrar*, 2011), and equatorial currents poleward of this domain may exhibit different characteristics than those seen here.

Along SD, the sign of $\partial Q/\partial y$ maintains a banded structure in the horizontal plane, suggesting barotropic instability above 150 m during TP2 and TP3. Both sections along SD meet the necessary condition for baroclinic instability near 50 – 70 km and 50 m, coinciding with the southern bound of the south branch of the EUC. This suggests that the barotropic and baroclinic processes associated with TIWs may originate as far east as the Galápagos Archipelago.

Inertial and Symmetric Instability

Positive relative vorticity associated with the position of the EUC just south of the equator, combined with the relatively small vertical planetary contribution to EPV near the equator, leads to positive EPV between the EUC core and the equator during all three time periods (Figures 2-10a – 2-10c). The magnitude of this positive EPV varies between time periods and has the potential to result in inertial or symmetric instability as the EUC meanders about its long-term average position near 0.25°S in the eastern equatorial Pacific west of the Galápagos Archipelago (*Wyrtki and Kilonsky*, 1984; *Johnson et al.*, 2002).

Sections along 93W and SD are stably stratified ($N^2 > 0$) for all time periods, gravitational instability is unlikely. Along 93W (Figures 2-12a – 2-12c for inertial instability and 2-13a – 2-13c for symmetric instability), conditions conducive to both symmetric and inertial instability (positive values in Figures 2-12 and 2-13) are present during all three time

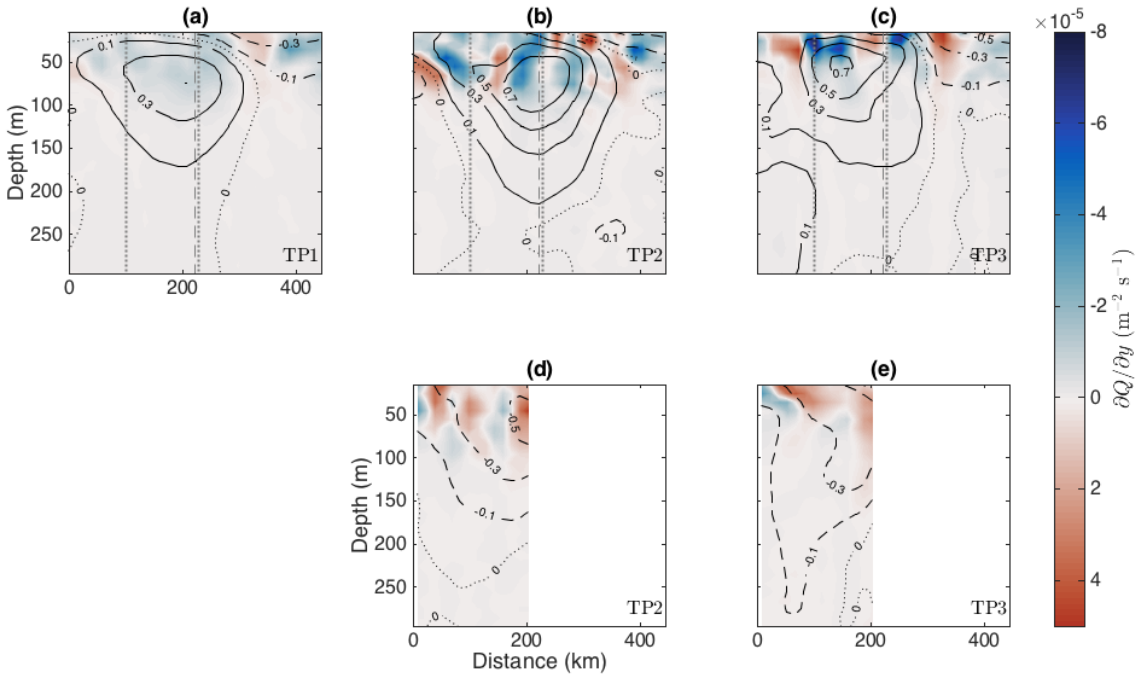

Figure 2-11: Average along-track gradient of EPV ($\partial Q/\partial y$) along 93W (a – c) and SD (d, e) over (a) TP1, (b, d) TP2, (c, e) TP3 as a function of distance from the point (93°S, 2°S) along each survey line. Zonal velocity (m s^{-1}) is shown in black solid (positive), dashed (negative), and dotted (zero) contour. Vertical, dotted gray lines (a – c) denote the meridional extent of the Galápagos Archipelago and dashed, gray line the equator.

periods due to the average position of the EUC core centered south of the equator. Unstable regions ($fQ < 0$; *Thomas et al.*, 2013) along 93W exist just south of the equator extending furthest poleward near the surface (Figures 2-12a – 2-12c and 2-13a – 2-13c), coincident with regions of EPV opposite in sign of the Coriolis parameter. Conditions conducive to symmetric instability are generally located near the surface, where Q_h (Figures 2-14a – 2-14c) and EPV (Figures 2-10a – 2-10c) both have sign opposite to f. Inertial instability generally is possible over a broader depth range, where Q_v (Figures 2-15a – 2-15c) and EPV both have sign opposite to f. Possible inertial (Figures 2-12a – 2-12c) and symmetric (Figures 2-13a – 2-13c) instabilities associated with the EUC along 93W have similar e-folding timescales in the range 4 – 13 days, indicating that both types of instabilities may exist in the region between the EUC core and the equator, particularly near the surface where the ratio of Q_h to Q_v is near one.

Along SD, inertial instability is possible at the boundary with the Galápagos Archipelago during TP2 and TP3 (Figures 2-12d and 2-12e). During TP3, conditions conducive to inertial instability are associated with Q_v with sign opposite to f between 0 – 200 m. Positive

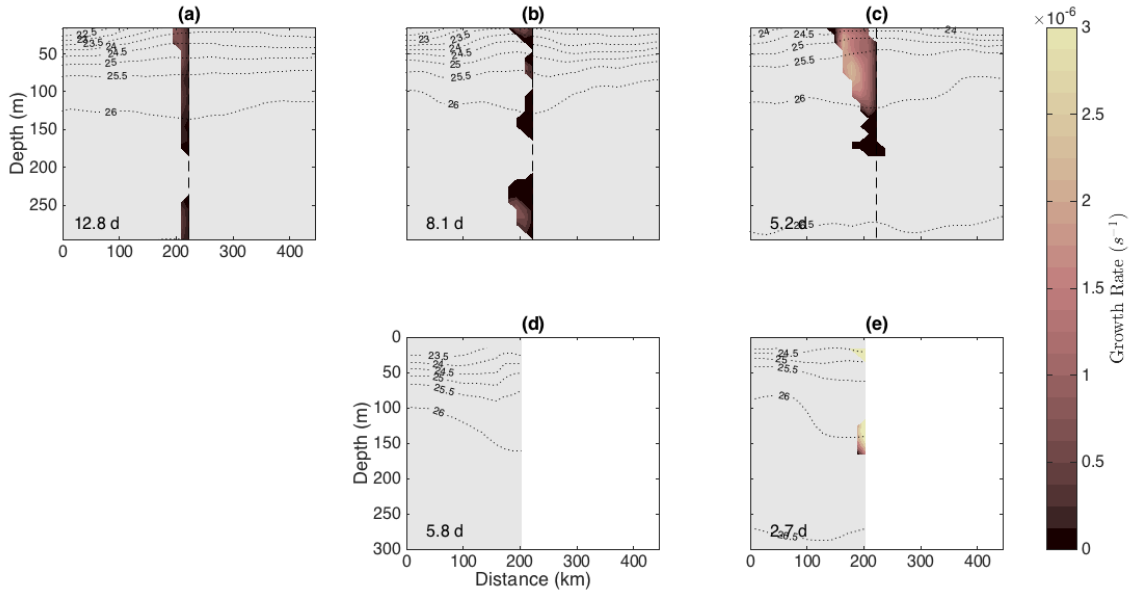

Figure 2-12: Average growth rate ω_I for (a, d) TP1, (b, e) TP2, and (c, f) TP3 along 93W (a – c) and SD (e – f) as a function of distance from the point (93°S, 2°S) along each survey line, with positive values indicating exponential growth. Fastest e-folding time associated with positive growth rates are shown in days (bottom left corner). Gray regions are stable to both symmetric and inertial instability ($fQ_d > 0$). Average isopycnal depth is shown in dotted, black contour. Vertical, black, dashed line denotes the equator.

unstable growth rates extend southward in regions of relatively high shear associated with the south branch of the split EUC core with an e-folding timescale of 2.7 days. During TP2, it is unlikely either instability will develop, as only a very minimal region is conductive to either inertial or symmetric instability (Figures 2-12d – 2-12e and 2-13d – 2-13e).

Conditions favorable to inertial and symmetric instabilities exist between the equator and the EUC core, consistent with the off-equatorial, eastward jet model of *Stevens* (1983). We expect inertial/symmetric instability to reduce positive EPV in the southern hemisphere on timescales of days or weeks. As the average position of the EUC core is south of the equator on long time scales, there must be a mechanism maintaining positive EPV in the region between the EUC core and the equator.

Surface wind forcing may be a dominant factor since unstable positive EPV primarily occurs above the EUC core, particularly during TP1 and TP2 (Figures 2-10a and 2-10b). In addition, largest magnitude positive EPV and fastest e-folding times along 93W occur at the boundary of the SEC and EUC, particularly during TP3 when the SEC extends southward of the equator. As the EUC core is centered at 50 m depth and the SEC is a surface current,

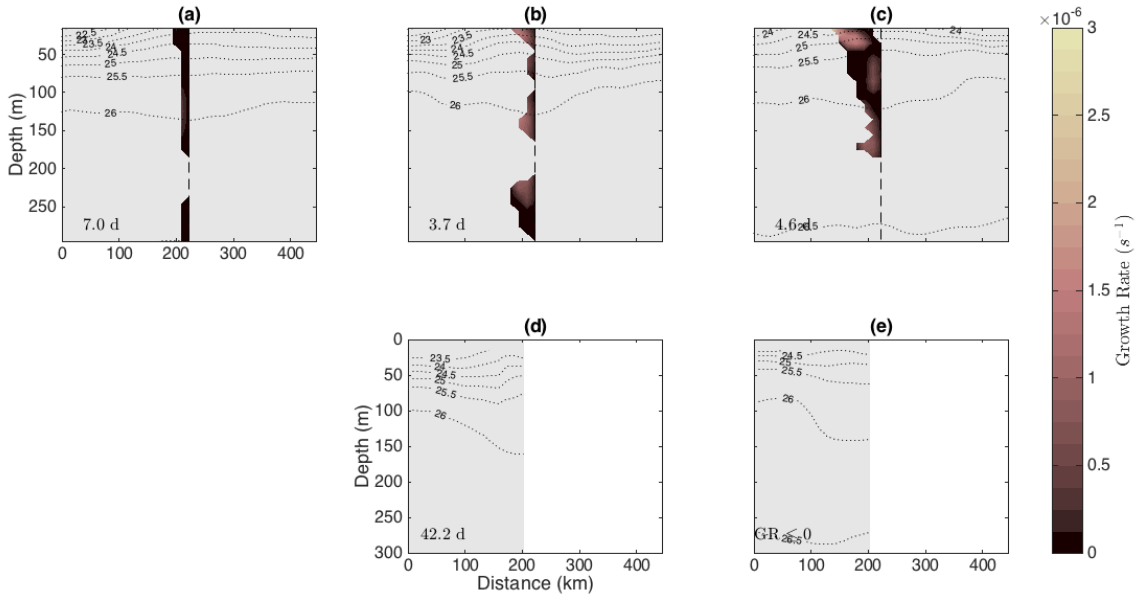

Figure 2-13: As in Figure 2-12, but for ω_S.

this "wrong-sign" EPV may be partially maintained by surface wind stresses.

Positive EPV along SD and conditions conducive to instabilities seen during TP3 may be a result of neglecting cross-track gradients of along-track velocity ($\partial v/\partial x$) in the relative vorticity contribution to EPV, which could impact EPV results in the boundary region between the southern branch of the EUC and the Galápagos Archipelago. To counteract the maximum existing positive contribution to EPV by the vertical component of relative vorticity during TP3, $\partial v/\partial x$ needs to be, at most, $\mathcal{O}(10)$ smaller than $\partial u/\partial y$. As along-line velocities along SD are smaller than, but of the same order as, velocities normal to SD, it is possible that positive relative vorticity during TP3 is a result of neglecting $\partial v/\partial x$. However, we do not see strong positive relative vorticity along SD during TP2, suggesting that either 1) the neglect of $\partial v/\partial x$ only results in positive relative vorticity during TP3 but not TP2 or TP1, or 2) positive EPV is advected south of the Galápagos Archipelago during TP3 due to the southerly position of the EUC core at that time.

Glider observations from which instability timescales are estimated do not represent an unperturbed background state. Rather, these observations necessarily include the effects of instabilities that do exist, and as such, constitute an adjusted state. The EUC core in the long-term average (TP1, Figure 2-10a) is weaker and extends further meridionally than that of TP2 or TP3 (Figures 2-10b and 2-10c). Positive EPV south of the equator is smaller in

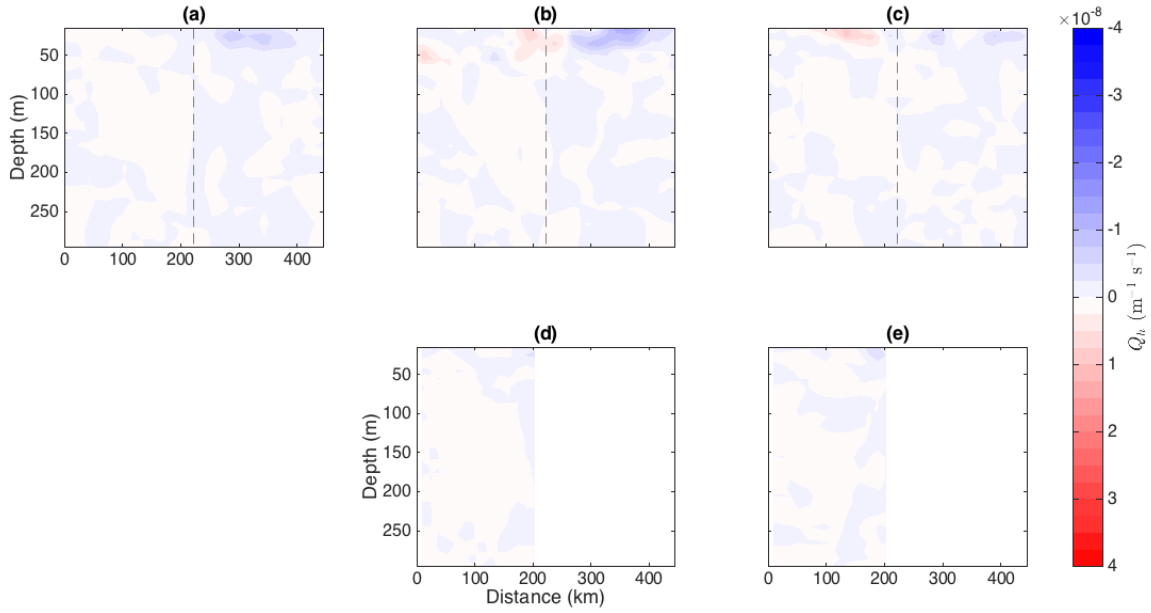

Figure 2-14: Average Q_h for (a, d) TP1, (b, e) TP2, and (c, f) TP3 along 93W (a – c) and SD (e – f) as a function of distance from the point (93°S, 2°S) along each survey line. Vertical, dashed line denotes the equator.

magnitude during TP1 compared to TP2 and limited in southern extent compared to TP3 (Figures 2-10a – 2-10c). It is possible that stirring as a result of inertial/symmetric instability is one of the mechanisms driving these differences in the long-term average compared to shorter-term averages. Symmetric instability results in along-isopycnal mixing, which will contain a vertical mixing component in regions where isopycnals are tilted (dotted lines of Figure 2-13). Symmetric instability may produce vertical mixing (*Thomas et al.*, 2013) along 93W during TP2 and TP3 (Figures 2-13b and 2-13c). Along-isopycnal mixing due to symmetric instability acts to reduce the magnitude of EPV with sign opposite to that of the Coriolis parameter. Estimated e-folding timescales for inertial and symmetric instabilities do not account for vertical mixing and are likely impacted by stirring that results from the instabilities themselves. Where symmetric instability occurs near the surface (along 93W during TP2 and TP3, Figures 2-13b and 2-13c), vertical mixing may contribute to the existence of the GCP. Since conditions conductive to symmetric instability are not apparent during TP1, it is unlikely that vertical mixing resulting from symmetric instability is a primary factor responsible for maintaining the GCP, but it may impact the SST associated with GCP on shorter timescales.

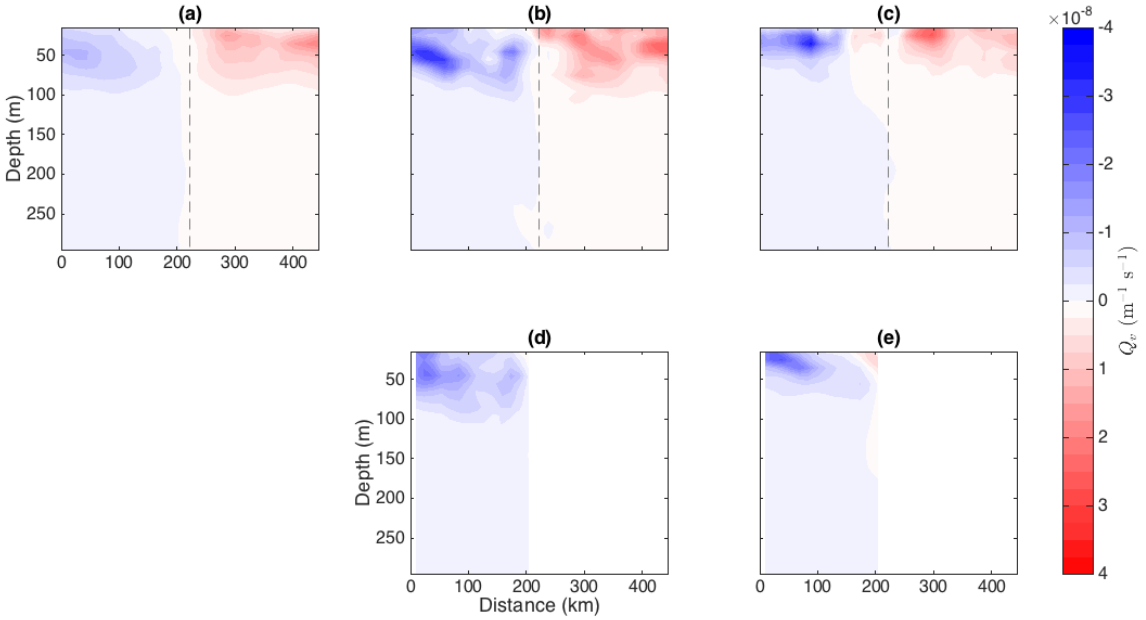

Figure 2-15: As in Figure 2-14, but for Q_v.

Kelvin-Helmholtz Instability

Kelvin-Helmholtz instability is a possible source of vertical mixing in regions where the gradient Richardson number (Ri) is less than 1/4. Estimates of Ri from glider observations, prior to horizontal smoothing (Section 2.2), show few regions with $Ri < 1/4$ during any time period (Figure 2-16). Regions where conditions conducive to inertial/symmetric instability exist are coincident with regions where $Ri > 1/4$ and Kelvin-Helmholtz instability is not expected.

2.4 Summary

Glider observations of temperature, salinity, and horizontal velocity with unprecedented subsurface resolution are used to estimate Ertel potential vorticity and the Bernoulli function in the upper 300 m just west of the Galápagos Archipelago. Conservation of these quantities along streamlines is consistent with the inertial model of the EUC developed by *Pedlosky* (1987a). During long-term (TP1) and short-term (TP2 and TP3) averages along 93W, EPV with sign opposite of the Coriolis parameter exists between the EUC core and the equator due to velocity gradients associated with the EUC and SEC. The average position of the EUC core is south of the equator, resulting in "wrong-sign" EPV in the southern

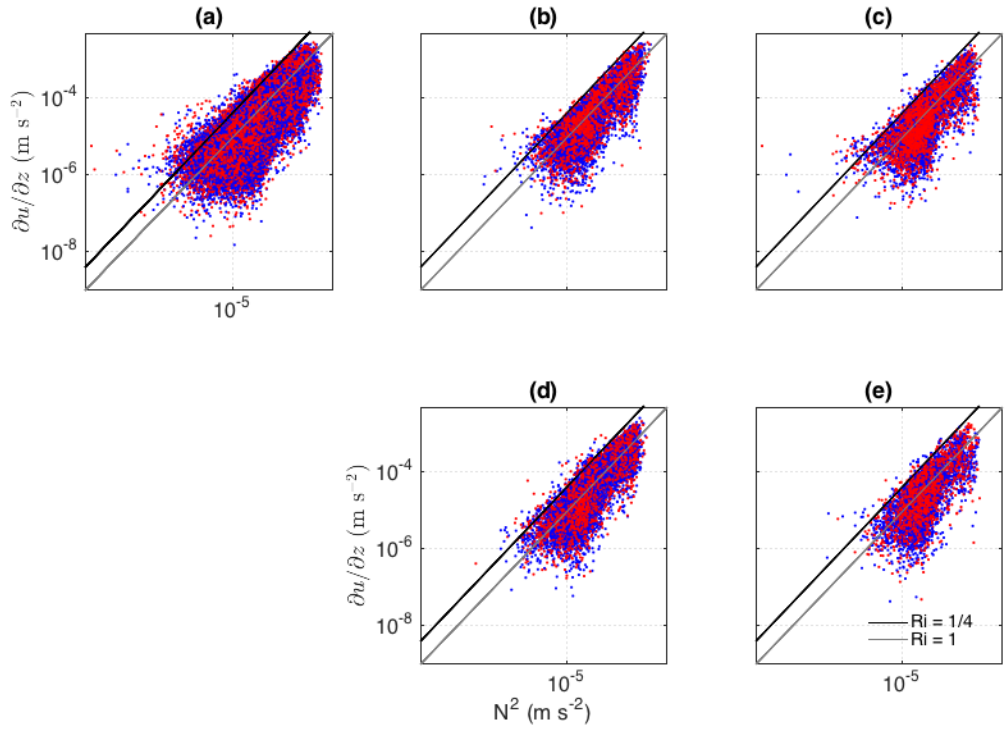

Figure 2-16: Scatter plot of N^2 and $\partial u/\partial z$ (Richardson number) for all observations during (a, d) TP1, (b, e) TP2, and (c, f) TP3 along 93W (a – c) and SD (e – f). Blue points have $fQ_d > 0$, red points have $fQ_d < 0$. All quantities are calculated from observations prior to smoothing in this figure only. The black line is $Ri = 1/4$ and gray line is $Ri = 1$.

hemisphere. This "wrong-sign" EPV extends as far south as the EUC core, between 0.7°S – 0.2°S depending on time period. Velocity measurements show the eastward EUC bifurcating into a north and south branch (Chapter 1) at a bifurcation latitude that corresponds to the meridional center of the Galápagos Archipelago. When the EUC core is located near 0.7°S, positive EPV is advected south of the Galápagos Archipelago by the south branch of the EUC. Positive EPV is not evident along SD when the EUC core is centered nearer the equator. Although no glider observations of the north branch of the EUC are available, it is expected that negative EPV is advected north of the archipelago when the EUC core is located north of the bifurcation latitude.

A qualitative comparison indicates that notable features of EPV and B sections south of the bifurcation latitude along 93W are seen along SD for TP2 and TP3. These features show advection of positive EPV across SD during TP3 and extends to general patterns in contours of EPV and the existence of local minima and maxima. The consistency between EPV and B along 93W and SD suggest that these quantities are conserved along streamlines, supporting

the assumptions of an inertial model of the EUC (*Pedlosky*, 1987a). Small discrepancies may be due to boundary effects and the surface and the north end of SD and time variability, as B is only conserved in a steady-state flow, and B and EPV are only conserved in inviscid, adiabatic flow.

The along-line gradient of EPV changes sign in the horizontal plane along 93W and SD from 2°S – 2°N for all time periods (TP1 – TP3) due to velocity gradients associated with the equatorial current system, suggesting barotropic instability. The necessary condition for baroclinic instability ($\partial Q/\partial y$ changes sign in the vertical plane) is only evident during TP2 in relatively limited regions compared to those exhibiting conditions conducive to barotropic instability. These results are consistent with prior studies concluding that TIWs are primarily a result of barotropic instability. This study is limited to the domain of 2°S – 2°N and does not consider stability of the North Equatorial Countercurrent (*Johnson et al.*, 2002).

Near the equator, the Coriolis parameter approaches zero, resulting in inertial instability in regions where horizontal shear exists and/or symmetric instability in regions with relatively high vertical shear. Glider observations indicate that inertial and symmetric instabilities are possible in all three time average sections along 93W and during TP3 along SD. Inertial/symmetric instabilities are attributed to shear associated with the EUC core and with shear between the EUC and SEC. E-folding timescales are typically between 2 – 13 days; however, these estimates are likely impacted by mixing of EPV that results from inertial/symmetric instabilities. Vertical mixing of colder subsurface waters with warmer surface waters as a result of symmetric instability has the potential to impact the anomalously cold SST of the GCP, particularly as symmetric instability is evident near the surface during TP2 and TP3.

A regional model analysis could provide insight into understanding the mechanism(s) behind persistent positive EPV south of the equator along 93W in the long-term average and quantify temporal scales of positive EPV along SD, beyond the two-month time periods presented here. Additionally, a modeling approach could complement this study by quantifying potential sources of error such as neglecting cross-line variations in temperature, salinity, and velocity and smoothing of the observed data. Future work will address these questions and address temporal variability on shorter time scales than the average sections presented here.

THIS PAGE INTENTIONALLY LEFT BLANK

Chapter 3

Three-Dimensional Distribution of Tropical Instability Waves using Argo Observations

Abstract

Tropical instability waves (TIWs) are westward-propagating, equatorially trapped instabilities with periods of 15 – 40 days and wavelengths of 700 – 2000 km that vary in intensity over periods of months. Propagation of TIWs in the equatorial Pacific Ocean has previously been observed via satellite sea surface temperature (SST), sea surface salinity (SSS), and sea surface height (SSH) measurements, as well as using subsurface measurements from Tropical Atmosphere Ocean (TAO) array measurements. TIWs may interact with the subsurface, equatorial current system, including the Pacific Equatorial Undercurrent (EUC). However, the subsurface three-dimensional distribution of TIWs has not yet been described. We apply spectral analysis methods to temperature, salinity, and potential density calculated from the *Roemmich and Gilson* (2009) gridded Argo temperature and salinity product over 10°S – 10°N latitude, $150 - 280°$ longitude, and 0–500 m depth to examine the three-dimensional signal associated with TIW propagation. The results are compared to theoretical dispersion curves, meridional modes, and vertical modes predicted for TIWs. A 1.5-layer, equatorial β-plane model is used to estimate TIW properties from an average zonal current obtained from SODA reanalysis. We find evidence of TIWs with 35 day periods and 1250 km wavelengths, in agreement with prior studies. The average meridional structure is similar to that predicted by *Lyman et al.* (2005), while the 1.5-layer model is not sufficient to capture baroclinic instability. The average vertical structure of TIWs from Argo observations is consistent with with average N^2 profiles calculated from both Argo and World Ocean Atlas (*Boyer et al.*, 2013) data.

3.1 Introduction

Tropical Instability Waves (TIWs) are equatorially-trapped, westward-propagating waves resulting from regional current shear with periods between 15 and 40 days and wavelengths between 700 and 2000 km (Figure 3-1). TIWs have been studied using numerical simulations and observations of sea surface height (SSH), salinity (SSS), temperature (SST), and meridional velocity from a variety of observational platforms including satellites, Acoustic Dopper Current Profiler (ADCP), and Tropical Atmosphere Ocean (TAO) array measurements. Studies using a range of observed variables, theoretical developments, and models at various locations report slightly different TIW properties depending on the specifics of the study. The primary aim of this study is to use observations of temperature, salinity, and potential density from Argo observations (*Riser et al.*, 2016) to determine the three-dimensional signal of TIWs across the equatorial Pacific.

In 1975, *Düing et al.* observed westward propagating, planetary scale waves in the equatorial Atlantic using both mooring and shipboard current measurements. Soon after, similar waves were observed in the equatorial Pacific region using current meters near the Galápagos Islands (*Harvey and Patzert*, 1976) and satellite SST (*Legeckis*, 1977). Many studies have since examined TIW properties using varying methods and observational datasets. Due to the horizontal spatial coverage of satellite data, many studies focus on the surface expression of TIWs in temperature, salinity, and sea level variation. *Matsuno* (1966) used single layer, quasi-geostrophic, free-surface theory to calculate dispersion curves of equatorially-trapped waves, including Rossby waves. *Farrar* (2008) used satellite SSH along with theoretical Rossby wave dispersion curves such as those calculated by *Matsuno* (1966) to show that TIWs tend to lie on or near the first-mode baroclinic Rossby wave dispersion curve. Long wave periods of 15 – 30 days are observed in SSH within about 5° of the equator (*Wunsch and Gill*, 1976), while periods between 35 and 50 days are seen closer to 10°N (*Périgaud*, 1990; *Farrar and Weller*, 2006).

Studies using both SST (e.g., *Legeckis*, 1977; *Chelton et al.*, 2000) and SSS (e.g., *Lee et al.*, 2012) show wave propagation just north and south of the equator across the equatorial Pacific. It is likely that the TIW signal in temperature and salinity appears where there is both wave propagation and a temperature or salinity gradient, resulting in advection of the observed properties. *Lee et al.* (2012) show 17-day TIWs within a few degrees of the equator

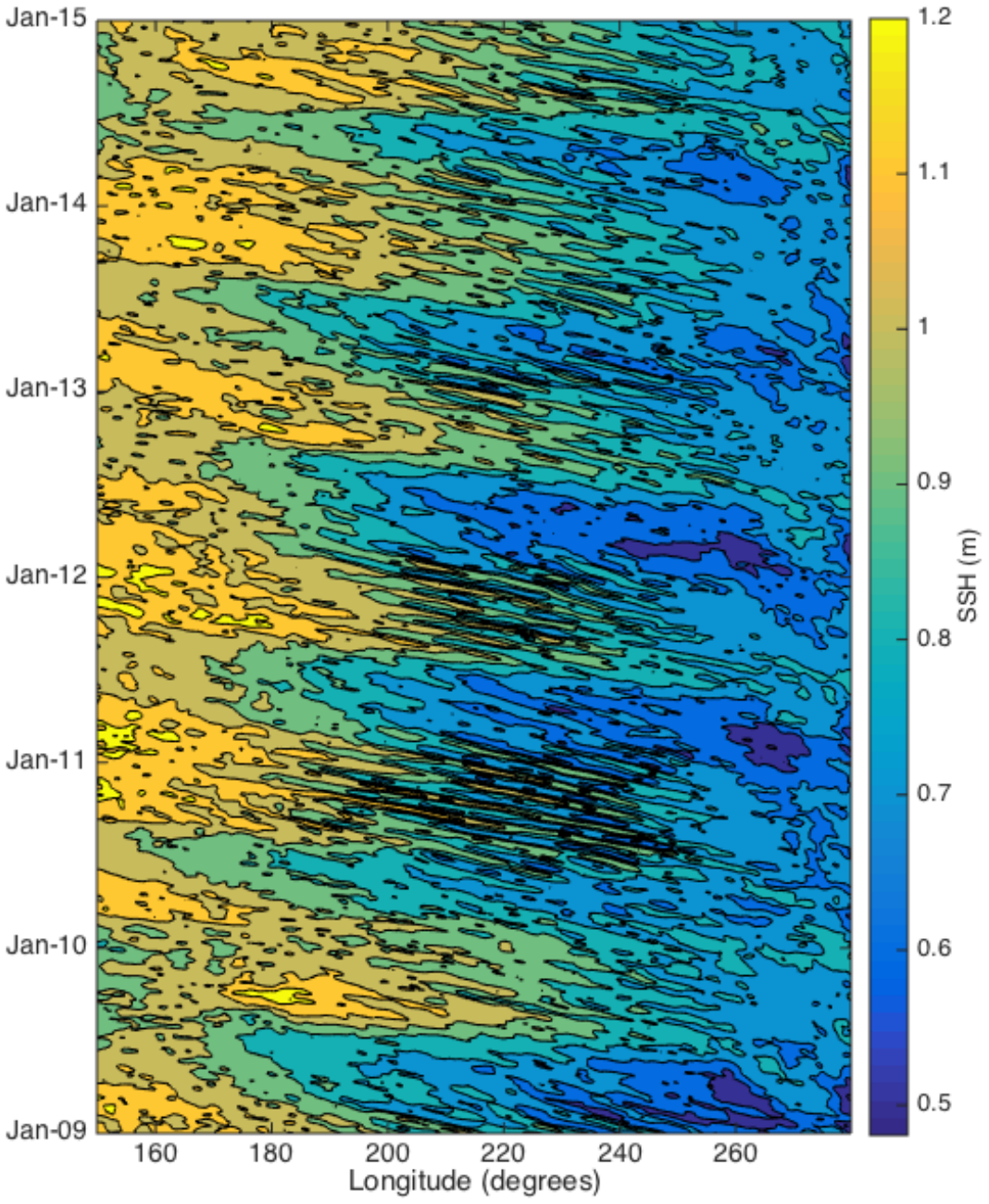

Figure 3-1: Monthly AVISO sea surface height at 5°N from 2009 – 2014.

and 33-day TIWs closer to 5°N in SSS and slight differences when compared to SST and SSH.

Meridional velocity and temperature measured by ADCPs, current meters, or TAO moorings have been used to examine TIW structure below the surface (e.g., *Qiao and Weisberg*, 1995; *McPhaden*, 1996; *Lyman et al.*, 2007). *Qiao and Weisberg* (1995) used horizontal velocity observations between 1°S – 1°N at 140°W from the Tropical Instability Wave Experiment (TIWE) to show that TIW-associated variance is maximum near the surface and decreases with depth. *McPhaden* (1996) used the TIWE array to show that maxima in temperature variance in the TIW frequency band along 140°W and between 0 and 7°N occur at the thermocline due to meridional and vertical advection. *Lyman et al.* (2007) examined TIW structure in temperature and meridional velocity along 140°W, finding surface-trapped 17-day TIWs in meridional velocity and a strong 33-day TIW signal in temperature at the thermocline. Together, these studies provide a detailed description of TIW structure; however, they are limited to 140°W.

The generation of TIWs is primarily attributed to both barotropic and baroclinic instabilities due to current shear resulting from the equatorial current system. Soon after the observations of *Düing et al.* (1975) and *Harvey and Patzert* (1976), it was theorized that westward propagating waves can be generated by barotropic instabilities from shear between surface currents, i.e. the westward South Equatorial Current (SEC) and the eastward North Equatorial Countercurrent (NECC) (*Philander*, 1976). *Philander* (1978) used a more realistic zonal current profile to show that barotropic instability resulting from shear between the SEC and NECC can generate waves with periods and wavelengths generally associated with TIWs and that baroclinicity may also play a role. *Johnson and Proehl* (2004) and *Qiao and Weisberg* (1995) used velocity data to confirm that TIWs can be generated through baroclinic instability caused by current shear between the the northern branch of the SEC (SECN) and the NECC.

Previous studies are limited by spatial data availability, either providing coverage across the Pacific basin at the surface only or subsurface observations with sparse coverage. The Argo program (*Riser et al.*, 2016) provides observations of temperature and salinity that will be used to study the structure of TIWs in all three spatial dimensions in the equatorial Pacific Ocean with the ability to resolve both TIW periods and wavelengths. Section 3.2 will describe the data used for the analysis, including Argo profiles and satellite observations.

Section 3.2.4 describes a 1.5-layer equatorial β-plane model used to numerically estimate TIW properties. Results (Section 3.3 are broken into three sections: a description of the spectral analysis methods used (Section 3.3.1), TIW structure via Argo temperature and salinity (Section 3.3.2) and via potential density (Section 3.3.3), and how the results relate to Rossby wave dynamics (Section 3.3.4). Section 3.3.5 focuses on the limitations of the approaches used in this study and strategies for future studies that could address these limitations. Section 3.4 summarizes the results and suggests future analyses.

3.2 Data and Methods

3.2.1 Optimally Interpolated Argo Data

Profiling Argo floats measure subsurface ocean temperature, salinity, and pressure and profile between the surface and 2000 m depth globally, including in the equatorial Pacific. *Roemmich and Gilson* (2009) provided a global, objectively mapped Argo dataset provided with $1^\circ \times 1^\circ$ horizontal resolution, 5-day temporal resolution, and varying vertical resolution ranging from 2.5 m at the surface to 100 m below 1500 m depth. We use gridded observations in the upper 200 m of the equatorial Pacific (10°S-10°N, $150 - 280^\circ$) from the *Roemmich and Gilson* (2009) mapped product for this analysis.

It is difficult to quantitatively estimate mapping error from the *Roemmich and Gilson* (2009) data. To address this potential limitation on regional (rather than global) scales, the number of Argo profiles in the equatorial Pacific region is considered (Figure 3-2a). Starting in 2009, the number of profiles in equatorial region tends to plateau compared to pre-2009. This is partially due to the change in Argo float hardware from Argos to Iridium communications, minimizing the time Argo floats remain at the surface. Near the equator, this translates to less exposure to wind stress transporting the floats poleward away from the equator. Since objective mapping error depends on the number of observations in a given region at a given time, this analysis will use data from 2009 – 2014, when the number of floats at the equator has increased from the pre-Iridium era. The spatial histogram of number of profiles occurring in $1^\circ \times 1^\circ$ latitude/longitude bins from 2009 – 2014 is shown in Figure 3-2b. Argo observations cover the entire equatorial Pacific with no major holes. Since TIWs have periods of less than 50 days, the use of profiles from 2009 – 2014 is sufficient, eliminating the time period where fewer Argo profiles exist while still covering a period when there is

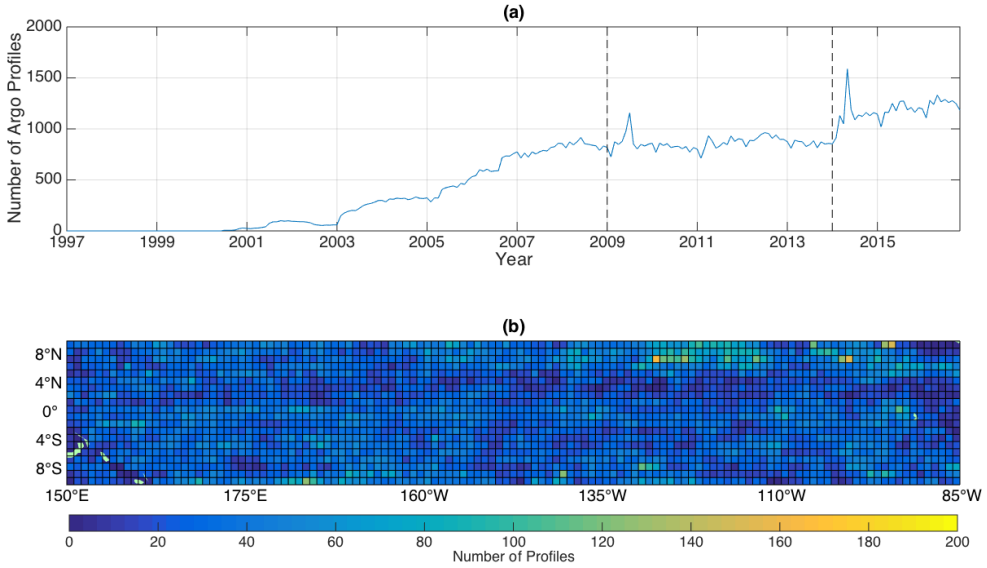

Figure 3-2: Total number of Argo profiles in the equatorial Pacific region (a) between 10°S – 10°N and $150 - 280°$ longitude from January 1997 through August 2017, binned monthly, and (b) from January 2009 through December 2014 binned into 1° longitude by 1° latitude bins as shown on the map. Dashed vertical lines in (a) indicate 2009 and 2014.

visible TIW propagation. Regions with low coverage may be minimized by the relatively large correlation scales used by *Roemmich and Gilson* (2009), which can smooth out regions or time periods with no observations with observations nearby. These correlation scales imply that the resolution of mapped data is close to 4° x 4°, or 400 km horizontal spatial resolution, which is consistent with the nominal Argo float density of 3° x 3°. The minimum wavelength resolvable using spectral analysis of observations with a horizontal resolution of 400 km is 800 km, just sufficient to resolve wavelengths of TIWs. Mapping error is discussed further in Section 3.3.5.

3.2.2 Remote Sensing Observations

Satellite observations are used to verify Argo measurements near the surface. SST observations are obtained from the Group for High Resolution Sea Surface Temperature (GHRSST). The L4 gridded, mapped, daily data have a horizontal resolution of $1/4° \times 1/4°$ and contain optimally interpolated observations from the Advanced Very High Resolution Radiometer (AVHRR), the Advanced Microwave Scanning Radiometer (AMSR), and in-situ observations (*Reynolds et al.*, 2007). These data are chosen due to their consistency with the timeframe of available Argo data and the addition of AMSR, which has improved coverage in a range

of weather conditions, albeit with lower resolution. Although the product is provided with daily resolution, the data are smoothed using a 7–day average (*Reynolds et al.*, 2007). SSH data are obtained from Aviso Ssalto/Duacs gridded multimission altimeter absolute dynamic topography mapped onto a $1/4^\circ \times 1/4^\circ$ horizontal grid provided daily. The actual temporal and horizontal resolution for this SSH product is less than the 10 day repeat cycle and the nominal 250 km spacing between the tracks for a altimeter satellite, which means this product should resolve TIW signals.

3.2.3 Reanalysis Data

The Simple Ocean Data Assimilation (SODA) reanalysis product (*Carton and Giese*, 2008) is used to calculate input parameters for the model described in Section 3.2.4. *Drenkard and Karnauskas* (2014) showed that an earlier version of SODA (2.2.6) reproduced the Pacific Equatorial Undercurrent (EUC) well when compared to TAO array mooring observations. SODA version 3.6.1 is provided with 0.1° latitude x 0.25° longitude resolution in 5 day increments and covers the 2009 – 2014 time period used here. Data are binned into 10 m vertical bins from the surface to 500 m depth. This resolution is sufficient to resolve 30 day TIW periods and 1200 km wavelengths.

3.2.4 Equatorial β-plane Wave Model

The relationship between frequency and wavenumber for Rossby waves in a spatially and temporally uniform zonal flow on an equatorial β-plane can be estimated as

$$\sigma = -\frac{\beta k}{k^2 + \dfrac{\beta}{2c(n+1)}} + Uk \tag{3.1}$$

where σ is wave frequency, k is zonal wavenumber, β is the meridional gradient of the Coriolis parameter, c is the first baroclinic phase speed, $n = 0, 1, 2...$ is the mode number, and U is constant zonal velocity. However, this approximation neglects changes in fluid depth due to geostrophic balance with the mean zonal flow. To address this limitation, we can estimate dispersion curves and growth rates for equatorial waves using a 1.5-layer numerical model that solves the equations of motion linearized about a mean zonal flow, based on *Proehl* (1998) and *Lyman et al.* (2005). We solve for wave solutions to u, v, and

p of the form $u = \tilde{u}e^{-(kx-\sigma t)}$. The lower layer is assumed to be motionless, while a mean zonal flow ($U(y)$) exists in the upper layer. The fluid is assumed to be linear, Boussinesq, incompressible and hydrostatic in an ocean with a rigid lid and flat bottom. The model formulation is described in detail in Appendix 3.A.

The mean zonal current in the upper layer is calculated from SODA reanalysis data. Zonal velocity from SODA is averaged over June 2010 (just prior to a period of strong TIW activity), 120°W – 93°W, and from the surface to the depth of the upper model layer (H_0). The resulting function $U(y)$ and related parameters are shown in Figure 3-21 (red curves).

3.3 Three-Dimensional TIW Signal via Argo Observations

3.3.1 Spectral Analysis Methods

We use spectral analysis to examine the three-dimensional structure of TIWs over 10°S – 10°N latitude, $150 - 280°$ longitude and 0 – 200 m depth. Figure 3-3 shows the evolution of *Roemmich and Gilson* (2009) mapped temperature anomaly in the equatorial Pacific. The mapped Argo data can resolve TIW-like propagation throughout the chosen time period, although results may be filtered due to the objective mapping procedures of *Roemmich and Gilson* (2009). Westward propagating signals with periods near 30 days can be seen in all panels of Figure 3-3, particularly in the high-pass filtered panel 3-3d. Notably, there is clear temporal variation in the strength of the propagating features (Figure 3-3a). The following analyses rely primarily on spectral analysis, so these ENSO modulated temporal variations (*Yu and Liu*, 2003) are not addressed in detail.

Frequency, zonal wavenumber and zonal wavenumber-frequency spectra are individually calculated at each point in the domain over individual time series for each latitude-longitude-depth coordinate for frequency spectra, over the longitude range at each latitude-depth-time coordinate for wavenumber spectra, and over time and longitude at each latitude-depth coordinate for wavenumber-frequency spectra. Spectra are calculated from the full temperature or potential density field including annual and seasonal cycles, with the mean and linear trend removed. To calculate frequency spectra, data are separated into yearly segments for segment-averaging. As an example, temperature spectra are calculated at 225° longitude and the depth of the thermocline based on Figure 3-4b. A peak at a period of 33–days (0.03 cpd frequency) can be seen in Figure 3-5b, confirming that at this location,

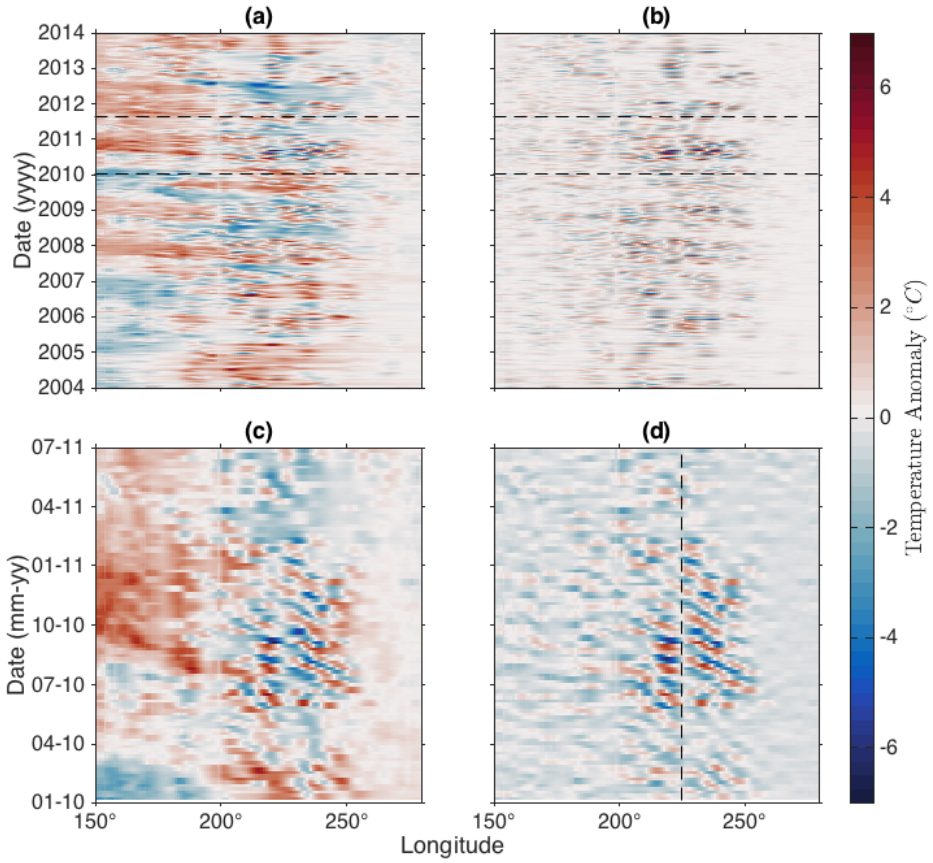

Figure 3-3: Hovmöller plots of Argo temperature anomaly at 6°N averaged over $90 - 150$ m depth. The time axis includes (a, b) the full available range of dates and (c, d) a subset of dates, denoted in dashed horizontal line in (a) and (b). No filtering has been done in panels (a) and (c). A 100-day high-pass filter has been applied to the data shown in panels (b) and (d). The dashed, vertical line in (d) indicates 225° longitude. All data are from the from the *Roemmich and Gilson* (2009) objective mapping of Argo profiles.

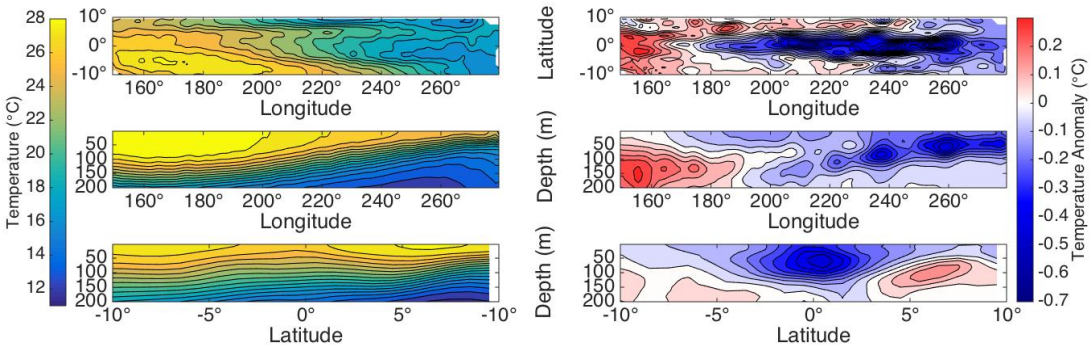

Figure 3-4: Temperature (left side) and temperature anomaly (right side) averaged over 2009 – 2014 from the objective mapping of Argo data *Roemmich and Gilson* (2009). The temperature field includes the sum of temperature anomaly, annual temperature anomaly, and temperature mean. The *Roemmich and Gilson* (2009) temperature anomaly removes seasonal and annual harmonics calculated from the 2004 – 2014 climatology.

objectively-mapped Argo data is capable of resolving 30 day TIW periods. The confidence interval indicates that this peak is marginally significant, and that at this location there is no significant 17 day period peak. It is unlikely that objectively mapped Argo data will be able to resolve TIWs with periods below 20 days due to the standard 10 day profiling interval of Argo floats unless multiple floats are located in the same region at the same time. Additionally, 17-day TIWs have been observed primarily in meridional velocity (*Lyman et al.*, 2007), which is not measured by Argo. The spectrum calculated from the full temperature field shows a significant peak near 1250 km zonal wavelengths (Figure 3-5d).

In the next sections, spectra like those in Figures 3-5b and 3-5d are calculated at each point and then integrated over frequency or wavenumber and averaged over various dimensions to visually represent the three-dimensional TIW signal.

3.3.2 Structure via Temperature and Salinity Observations

To further validate the use of Argo observations to examine TIW structure, Argo data near the surface are compared to GHRSST observations. The depth closest to the surface in the *Roemmich and Gilson* (2009) mapping is 2.5 dbar, so this is used to compare to satellite observations. Both Argo (at 2.5 dbar) and GHRSST (at the surface) show a similar spatial pattern of temperature variance (Figure 3-6) when spectral density is integrated over all frequencies. The magnitude of the total variance captured by GHRSST observations is consistently higher over the spatial domain (Figure 3-6c). Figure 3-7 shows similar spatial

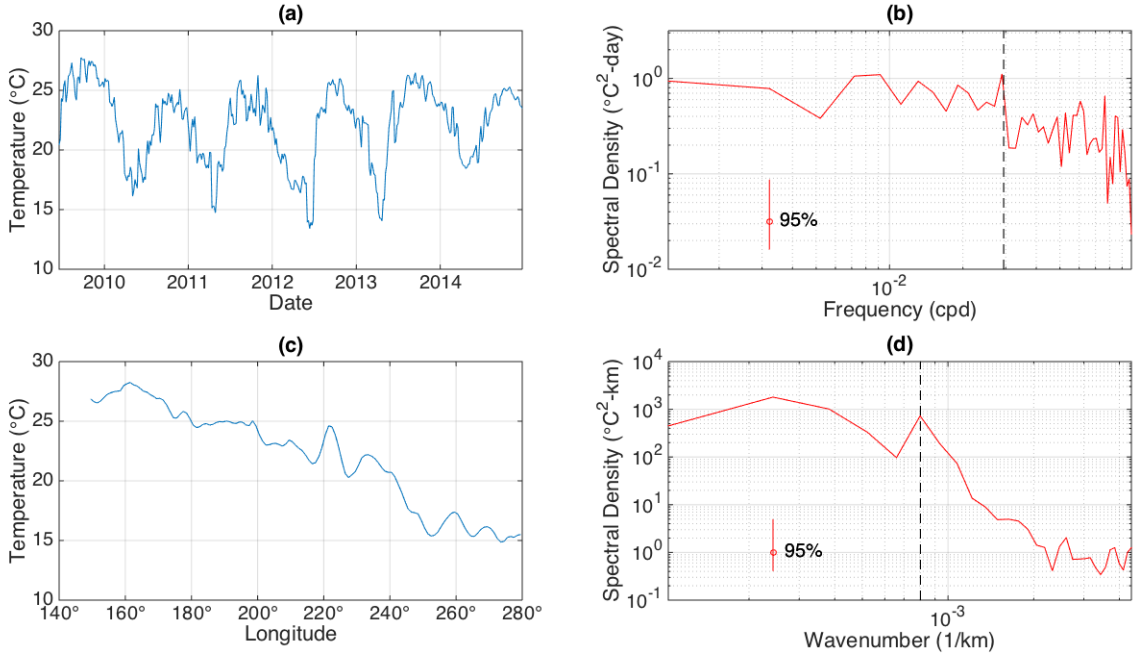

Figure 3-5: (a) Argo temperature timeseries over a subset of the 2009 – 2014 time range for 6°N, 225° longitude, and averaged over $110 - 120$ m depth, approximately the depth of the thermocline at this longitude per Figure 3-4. (b) Band-averaged frequency auto-spectral density of the time series in (a), with vertical, dashed line denoting a 34 day period. (c) Argo temperature versus longitude at 6°N and averaged over $110 - 120$ m depth. (d) Band-averaged wavenumber auto-spectral density of the temperature-longitude plot in (c), with vertical, dashed line denoting 1250 km wavelength. Confidence intervals for (b) and (d) are included.

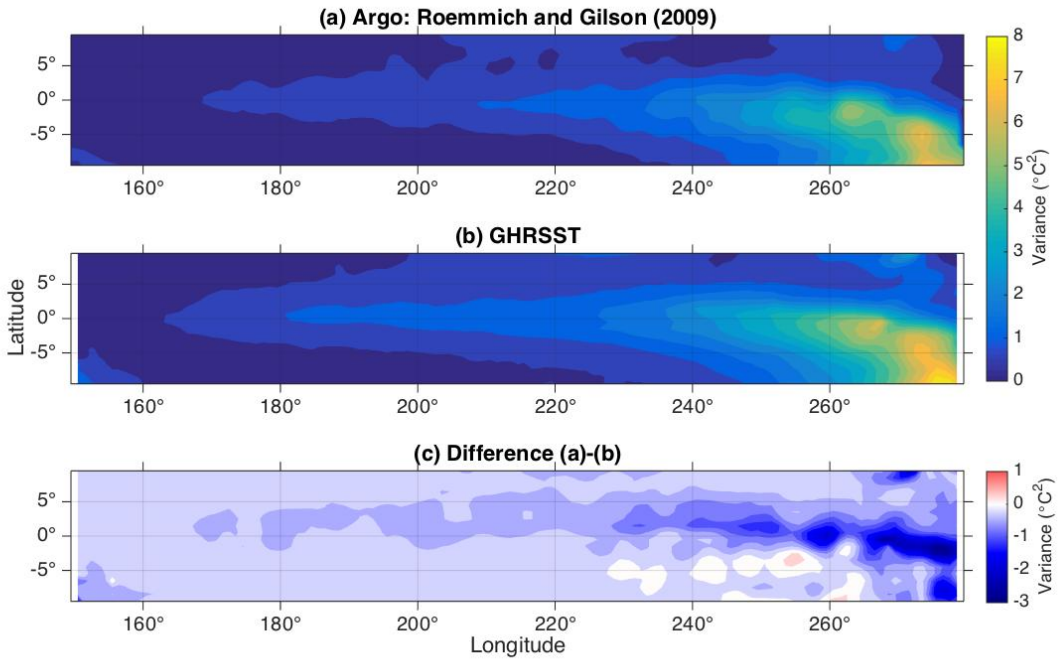

Figure 3-6: Total spectral variance of (a) *Roemmich and Gilson* (2009) Argo temperature and (b) GHRSST surface observations. Spectra are calculated at each latitude-longitude coordinate over 2009 – 2014, on the 2.5 dbar Argo pressure surface or GHRSST ocean surface, and integrated over all frequencies. The difference of the variances between the two sets of observations (a) minus (b) is shown in (c).

patterns of variance over the same spatial range in Argo temperature and GHRSST, however, spectral density is integrated over frequencies corresponding to 15 – 50 day periods only. In this specific frequency band, the variance captured by the *Roemmich and Gilson* (2009) product is nearly a factor of two higher than that of GHRSST. This discrepancy is likely due to differences in temporal resolution of observations and in mapping technique: GHRSST maps the satellite data in space and time while *Roemmich and Gilson* (2009) only map Argo data in space.

Per *McPhaden* (1996), temperature variance in the TIW band along 140°W is due to meridional and vertical advection in regions of non-zero temperature gradient. Consistent with those findings, patterns that arise in variance of Argo temperature across all longitudes are of greater magnitude than and very different from those of salinity. Advection of temperature or salinity requires the presence of both a non-zero gradient and a cross-gradient velocity. Although Argo doesn't observe current velocity, advection is supported by contours showing temperature and salinity gradient, respectively, in Figures 3-8 and 3-9. The temper-

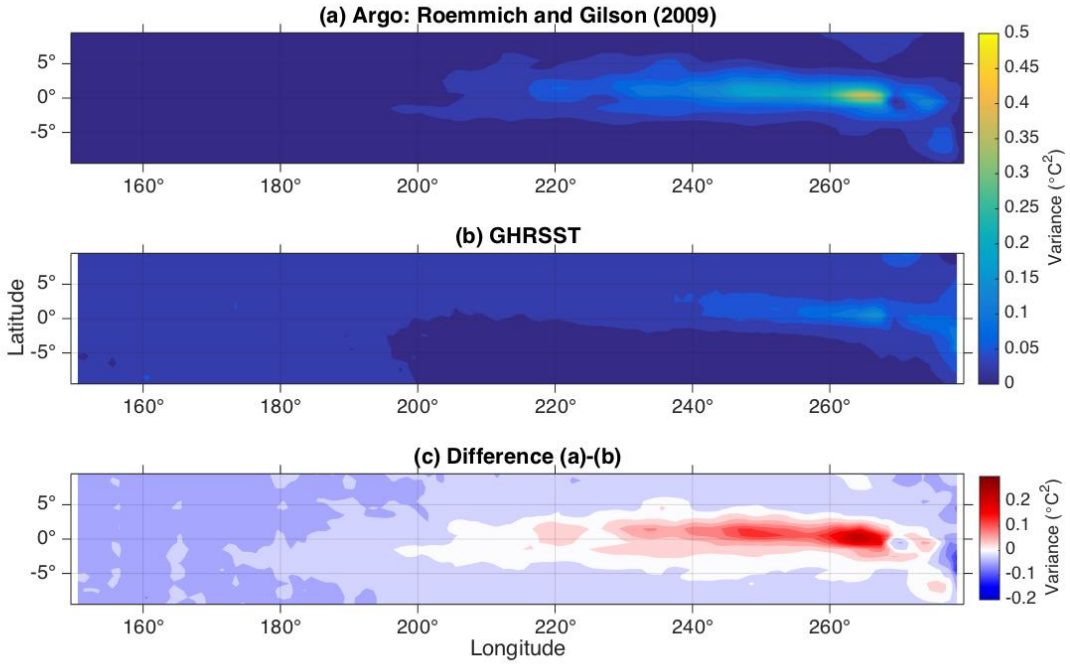

Figure 3-7: As in Figure 3-6, but for variance of only 15 – 50 day periods.

ature plots show a clear correlation between 15 – 50 day variance and temperature gradient in each of the three dimensions. The salinity plots show a less clear correlation, however, the only peaks that are significant when compared to the confidence interval are those near 280° longitude (Figures 3-9a and 3-9b) and those near the surface in Figure 3-9c. Each of these is located in a region of high salinity gradient. To examine the three-dimensional structure of TIWs, a property more directly related to TIW dynamics is preferred.

3.3.3 Structure via Potential Density

Spectra are estimated from potential density calculated using Argo objectively mapped temperature and salinity data. Temperature is the dominant property in most locations in this region, however, salinity also impacts the 15 – 50 day variance. Since the zonal record length (the width of the Pacific) is small compared to TIW wavelengths, three-dimensional structure of TIWs can only be examined using frequency spectra. However, wavenumber-frequency plots will also be used to compare properties of the propagating waves to theoretical predictions.

Variance in the TIW band is strongest in the thermocline at depths of 80 m and 120 m

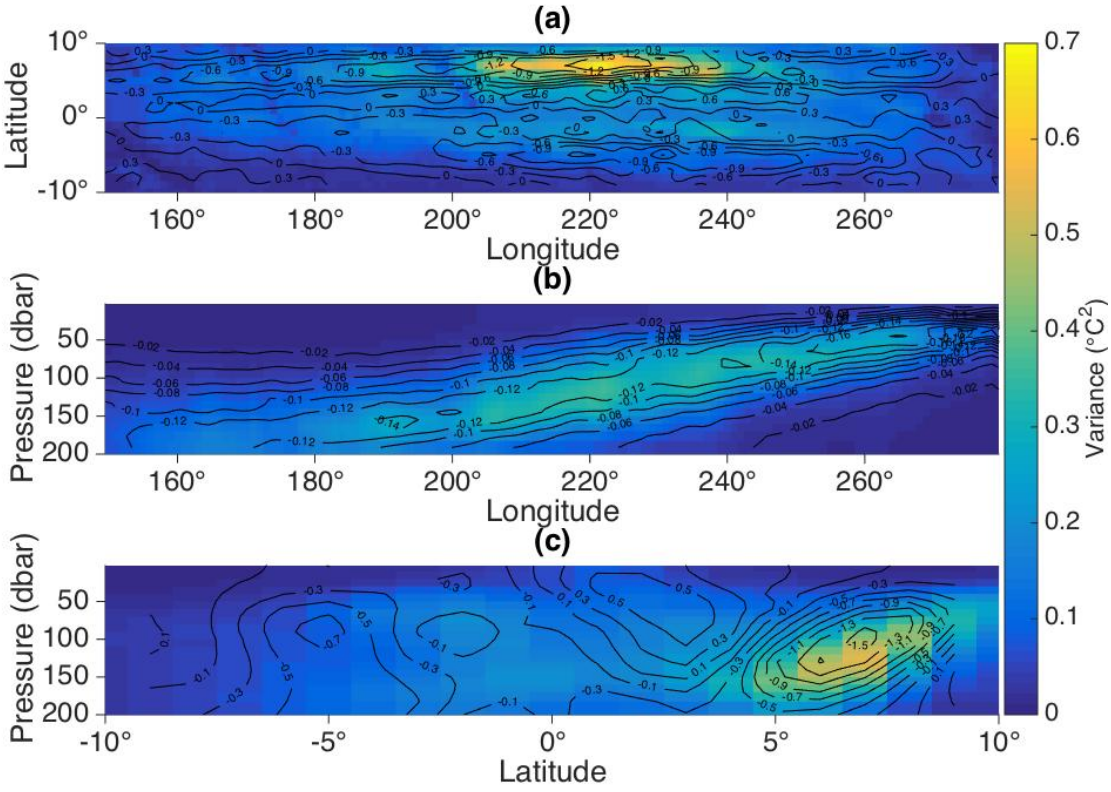

Figure 3-8: Spectral variance of Argo temperature in the 15 – 50 day band and averaged over (a) pressure, (b) latitude and (c) longitude shown in color shading. The contours (black) show temperature gradient: (a) $\partial T/\partial y$, (b) $\partial T/\partial z$, and (c) $\partial T/\partial y$ in °C per degree latitude in (a) and (c) and in °C per dbar in (b).

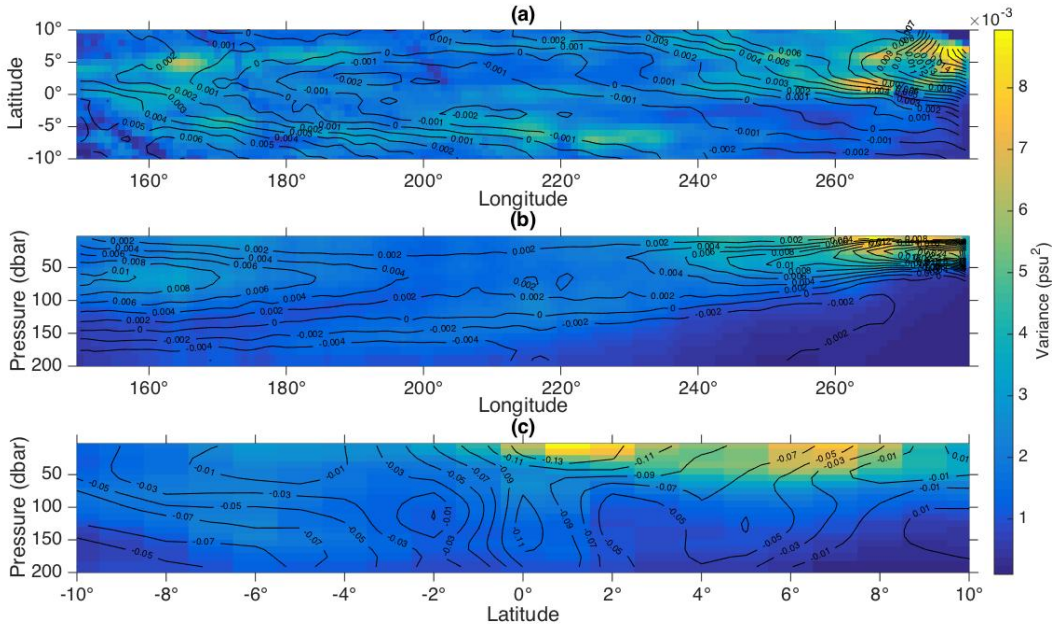

Figure 3-9: As in Figure 3-8, but for salinity spectra and gradients. The contours show meridional salinity gradient ($\partial S/\partial y$) in psu per meter.

(Figures 3-10c and 3-10d, Figure 3-12). Moving westward, the region of strongest variance of potential density in the TIW band increases in depth, consistent with the deepening of the thermocline in the western Pacific. A minimum in variance along the equator in the TIW band and maxima near 6°N and 2°S are present in panels (b) – (e). Smallest variance out of the latitudes shown occurs at the equator, while the largest variance occurs at 6°N. This is consistent with previous studies (e.g., *Périgaud*, 1990; *Farrar*, 2008, 2011) at the surface using SSH observations (Figure 3-11). This meridional asymmetry is a reflection of asymmetry in vertical and horizontal shear associated with the equatorial current system (e.g., *Philander*, 1978; *Yu et al.*, 1995; *Lyman et al.*, 2005; *Farrar*, 2008). The pressure signal of baroclinic modes also defines the associated vertical structure of horizontal velocity (*Pedlosky*, 1987c). Since the spectral signal is associated with advection of potential density in regions of high potential density gradient, this asymmetry in the baroclinic modes of horizontal velocity will appear in the spectral variance of potential density in the TIW band.

This pattern is retained at depths between 0 and 200 m, particularly between 190° and 270° longitude. Aviso SSH data shows a peak in spectral variance also between 190° and

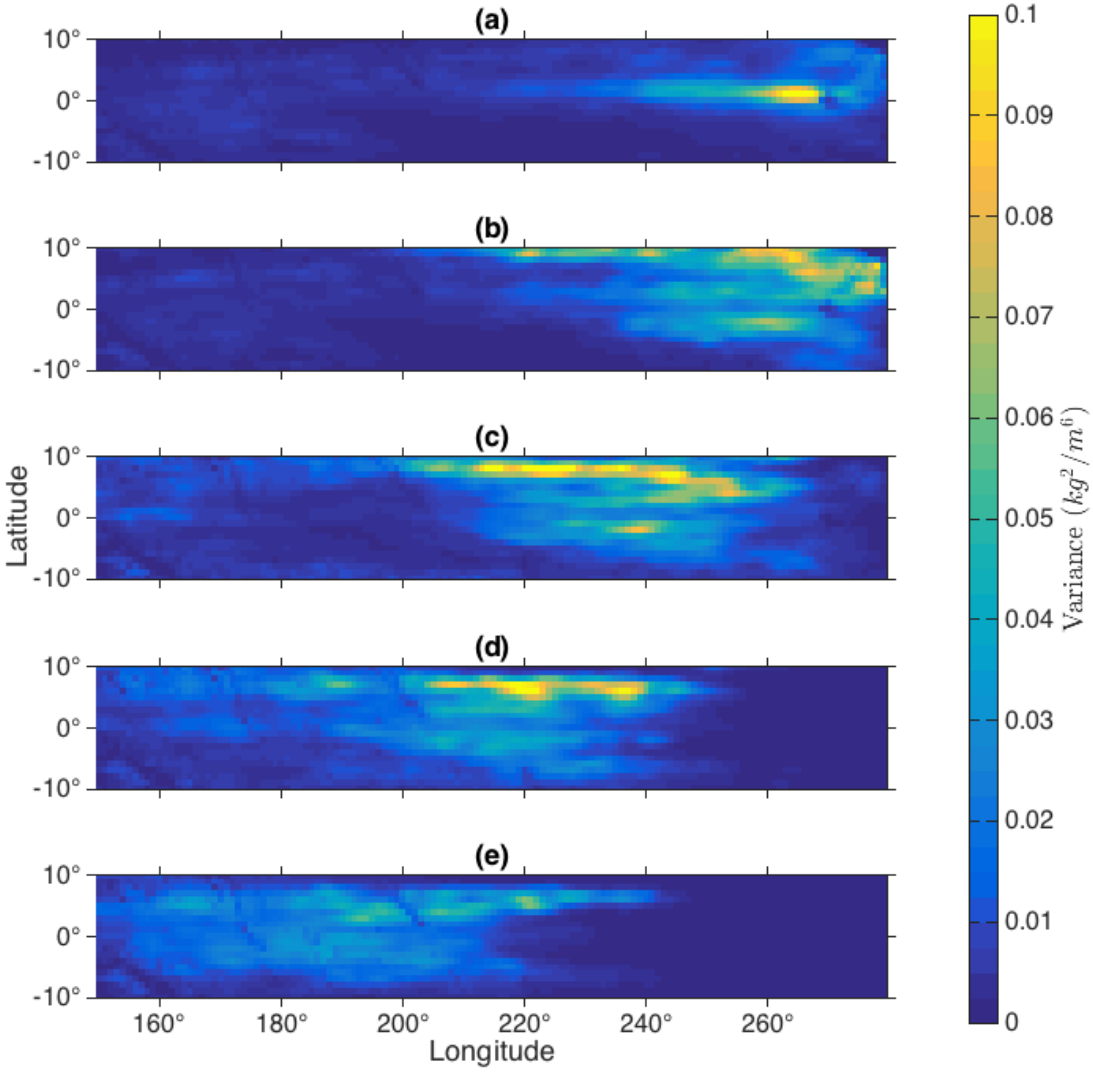

Figure 3-10: Average spectral variance of Argo potential density in the 15 – 50 day band at five different depths: (a) 2.5 m, (b) 40 m, (c) 80 m, (d) 120 m, and (e) 160 m.

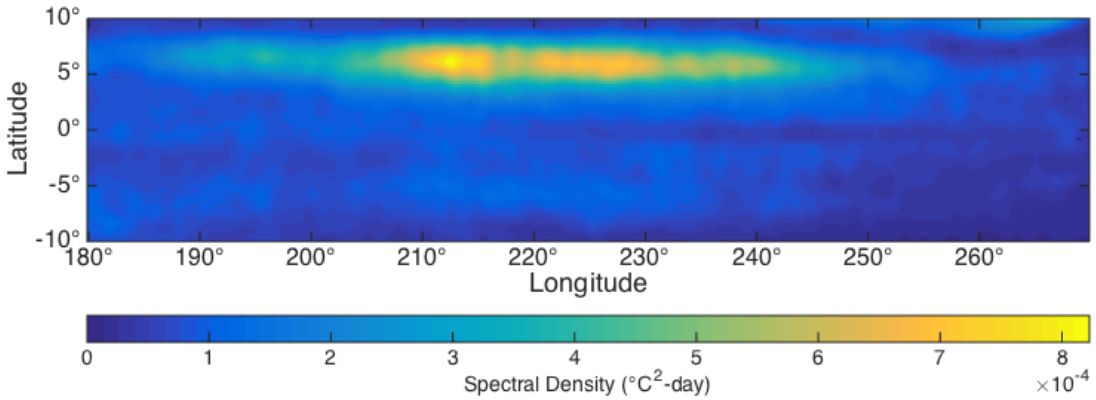

Figure 3-11: Spectral variance of AVISO SSH surface observations in the TIW period band. Spectra are calculated at each latitude-longitude coordinate over 2009 – 2014 and integrated over frequencies corresponding to 15 – 50 day periods.

270° longitude. Minima are seen at the equator, although the mapped Argo resolution shows this less clearly than the higher resolution Aviso observations (Figure 3-13b). Peaks in variance tend to follow the thermocline, with notable maxima near 6°N and 2.5°S. At 250° longitude (Figure 3-13d), the thermocline shoals enough that the variance in the TIW band reaches the surface, consistent with SST observations. Notably, there is a TIW signal north of the equator at 280° longitude, east of the Galápagos Archipelago.

3.3.4 Tropical Instability Wave Dynamics

We consider the variance distributed in both frequency and wavenumber to justify the association of 15 – 50 day variance of Argo potential density with TIW propagation. Figure 3-14 shows the mean zonal wavenumber-frequency spectrum averaged over 10°S – 10°N and 0 – 200 m depth. The peak at 0.03 cpd frequency corresponds to TIW-like wavenumbers (wavelengths near 1250 km). There is also a ridge at 0.03 cpd with zero wavenumber, consistent with a red spectrum. When high-variance latitude bands at the depth of the thermocline are considered, for example, 5°N – 8°N and 90 – 200 m, the spectral peak at TIW wavelengths becomes significantly stronger when compared to the 95% confidence interval (Figure 3-15). Variance seen in these regions is due to TIW propagation, primarily with periods between 25 and 35 days and wavelengths between 1000 and 1600 km.

Following *Farrar* (2011), theoretical dispersion curves for equatorially-trapped waves are compared with the zonal wavenumber-frequency spectra of Figures 3-14 and 3-15. In

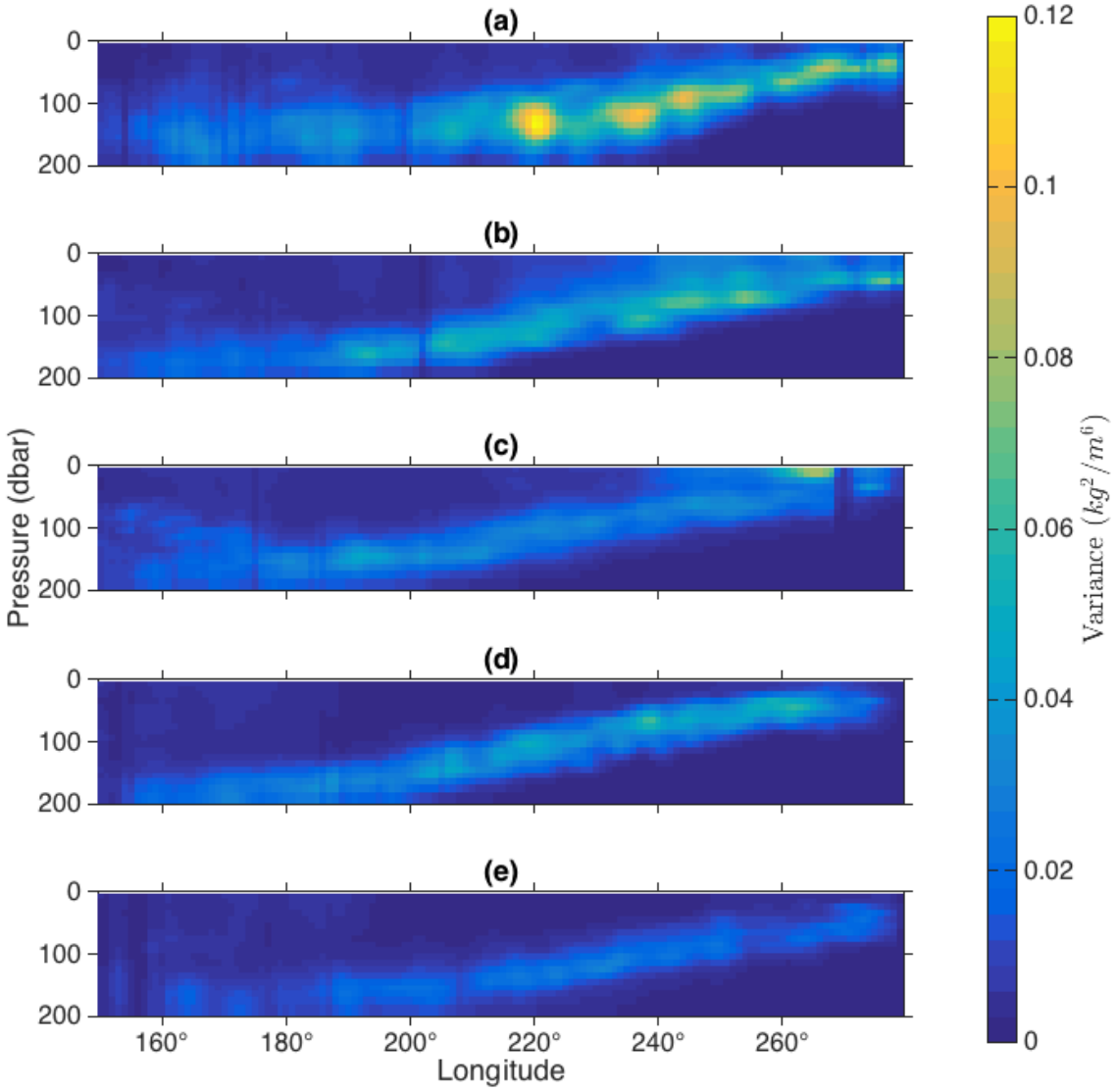

Figure 3-12: Average spectral variance of Argo potential density in the 15 – 50 day band at five different latitudes: (a) 6°N, (b) 3°N, (c) 0°, (d) 3°S, and (e) 6°S.

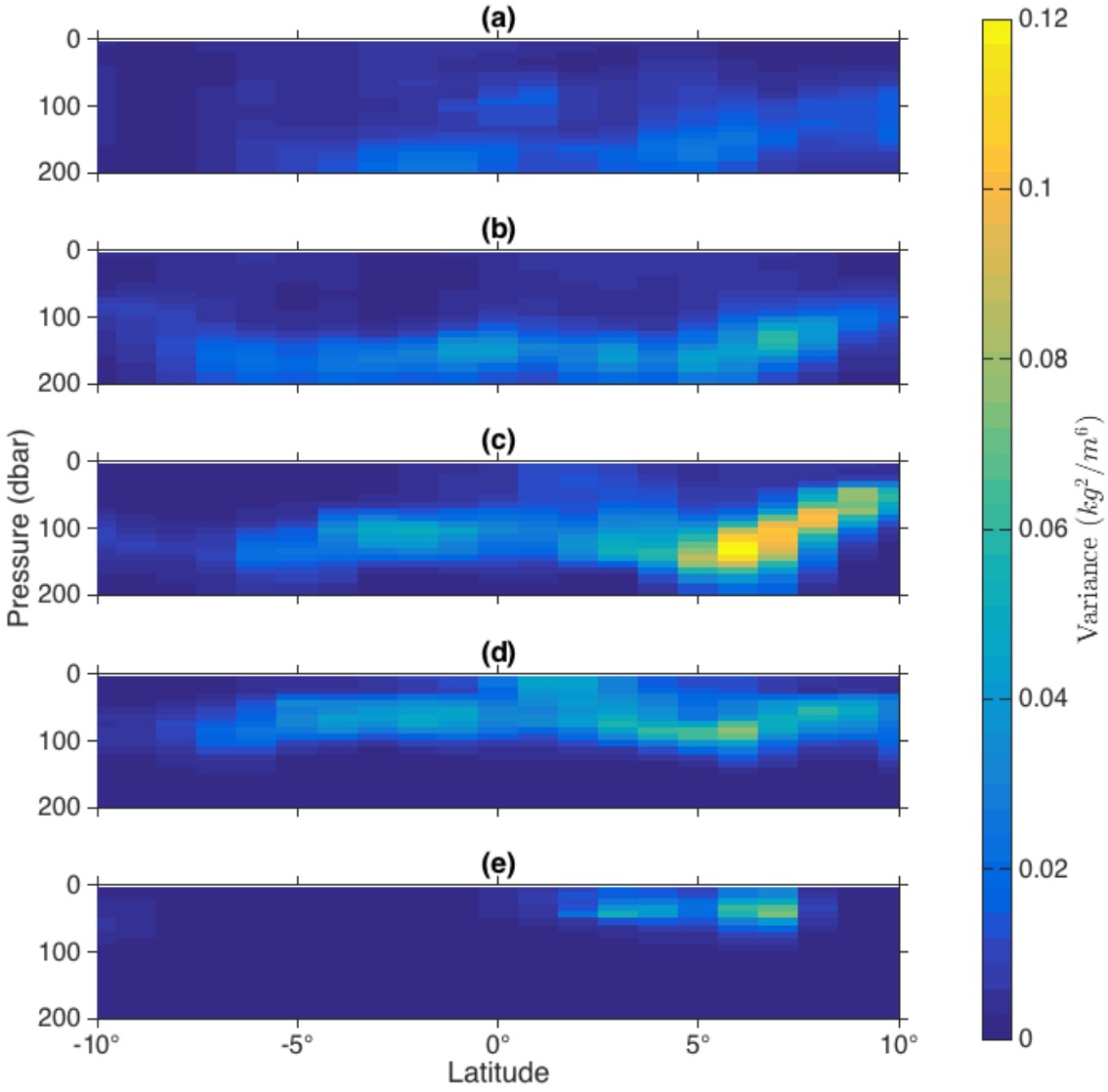

Figure 3-13: Average spectral variance of Argo potential density in the 15 – 50 day band at five different longitudes: (a) 160°, (b) 190°, (c) 220°, (d) 250°, and (e) 280°.

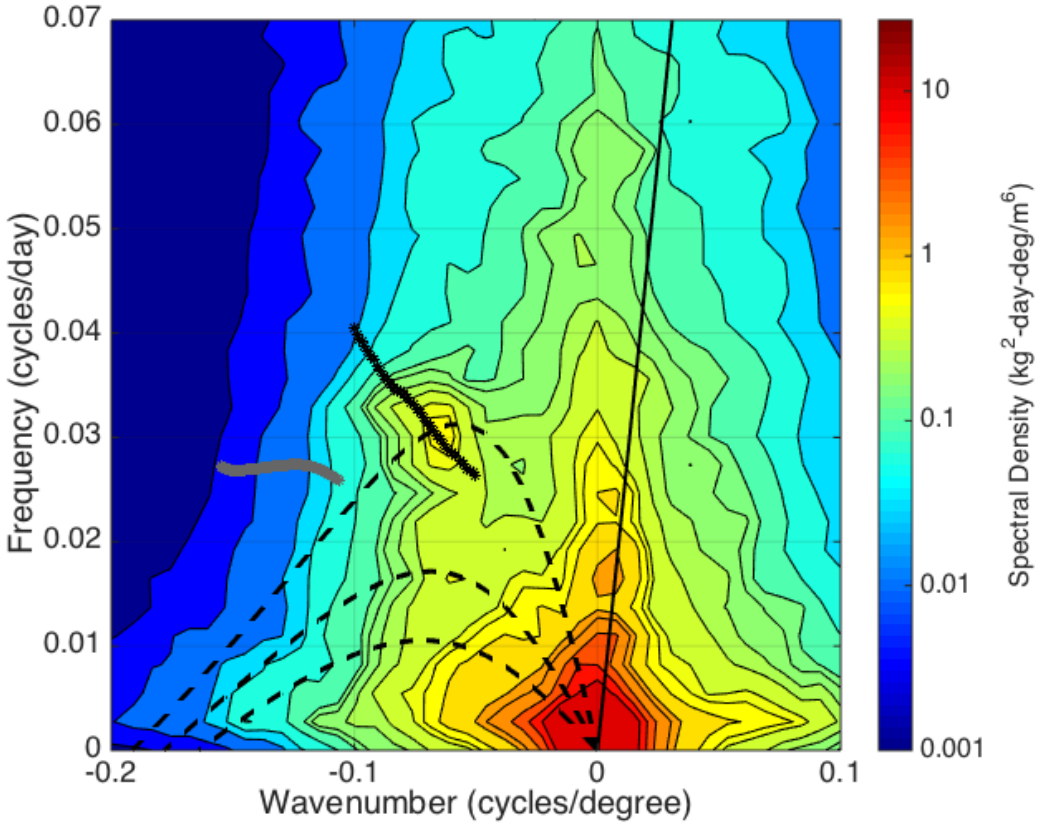

Figure 3-14: Log-log zonal wavenumber-frequency diagram of 2-D, spectral density of potential density over the domain $10°\text{S} - 10°\text{N}$, $150° - 280°$ longitude, and $0 - 200$ dbar pressure from $2009 - 2014$. Spectra are averaged over all latitudes and depths in the domain. The 95% confidence interval is indicated by two horizontal lines on the colorbar. Black, solid line is the first mode Kelvin wave. Dashed, black lines are the $n = 0, 1, 2$ modes of Equation 3.1 with $U = 0.17$ m s^{-1}. Black asterisk line is the fastest growing mode from *Lyman et al.* (2005). Gray asterisk line is the fastest growing mode from the 1.5-layer model.

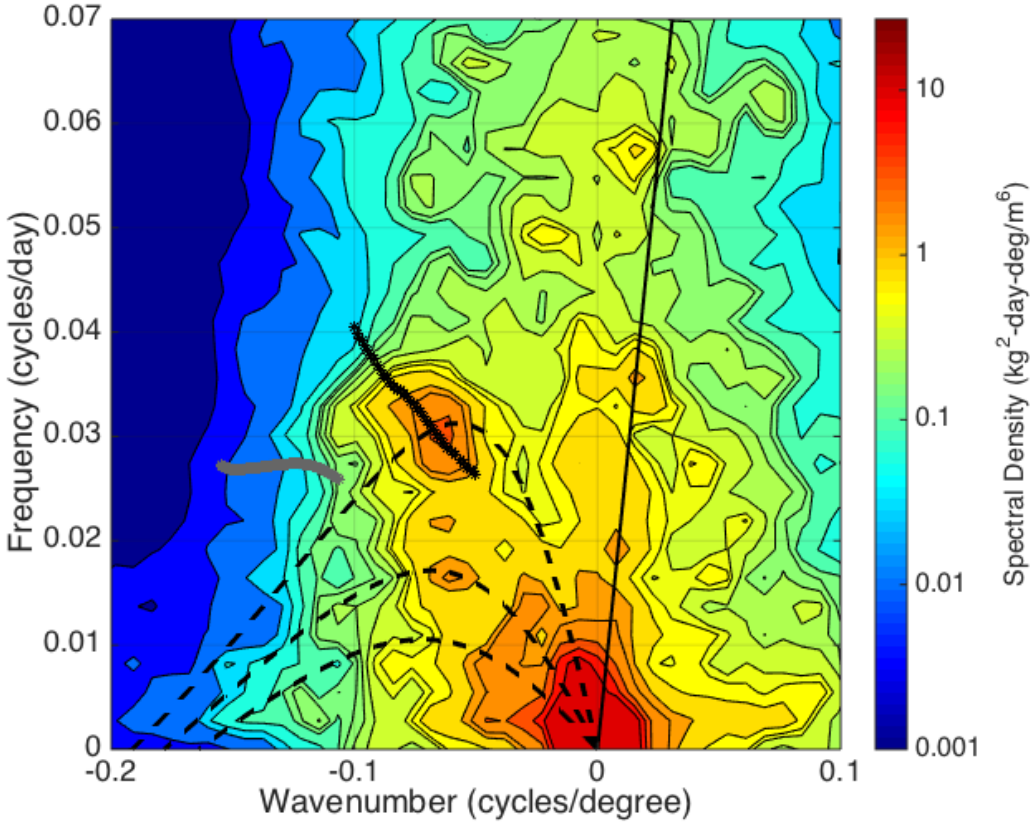

Figure 3-15: As in Figure 3-14, but averaged over $5°\text{N} - 8°\text{N}$ and $90 - 200$ dbar pressure.

this study, dispersion curves calculated via the 1.5-layer equatorial β-plane model (linearized about a mean zonal flow, $U(y)$) are compared to dispersion curves from *Lyman et al.* (2005), Rossby waves in a mean zonal flow (Equation 3.1), and the the observed wavenumber-frequency spectra.

The $n = 0$ and $n = 1$ dispersion curves based on Equation 3.1, with $U = 0.17$ m s^{-}1 align with the major peak at 33 days and 1250 km and also the secondary peak near 66 days and 1250 km. However, the mean flow over the domain at which we estimate spectra is westward, not eastward, indicating additional dynamics that incorporate the meridional variation in the equatorial current system are necessary to describe TIWs. The fastest-growing mode of the 1.5-layer model with mean zonal current obtained from SODA reanalysis occurs at wavelengths near 750 km and periods near 35 – 40 days (Figure 3-16). The discrepancy in wavelength between this estimate and that of Figures 3-14 and 3-15 is likely due to the barotropic nature of the 1.5-layer model. As the observed spectra have a peak near 1250 km and 33 days, the *Lyman et al.* (2005) estimate, incorporating baroclinic dynamics, aligns well with the spectral results from Argo data. This is consistent with the results of *Farrar* (2011) using SSH.

Lyman et al. (2005) note that the dispersion relation that results from an equatorial β-plane model are sensitive to the mean zonal background current. The 1.5-layer model is used to compare the resulting dispersion curves from the SODA average zonal current over June 2010 to that of the 2009 – 2014 average and the July 2005 average. While the June 2010 zonal current results in TIW periods of 35 – 40 days (Figure 3-16), the July 2005 current estimates periods near 50 days over similar wavelengths. The 2009 – 2014 average produces a fastest growing mode with negligibly small growth rates. While *Lyman et al.* (2005) estimate a dispersion curve for TIWs that is consistent with Argo observations, the 1.5-layer model suggests that this estimate is likely sensitive to the mean zonal flow that occurs just prior to individual time periods of TIW propagation.

Similarly, the meridional structure of the 33 day, 1250 km mode from *Lyman et al.* (2005) is comparable to that of the spectral variance of Argo potential density (Figure 3-17). Both show a minimum near the equator, a local maximum south of the equator, and a stronger maximum north of the equator. However, those maxima are shifted poleward in the Argo data compared to the model results of *Lyman et al.* (2005). As dispersion curve model results are sensitive to $U(y)$, it is possible that differences are due in part to variations in

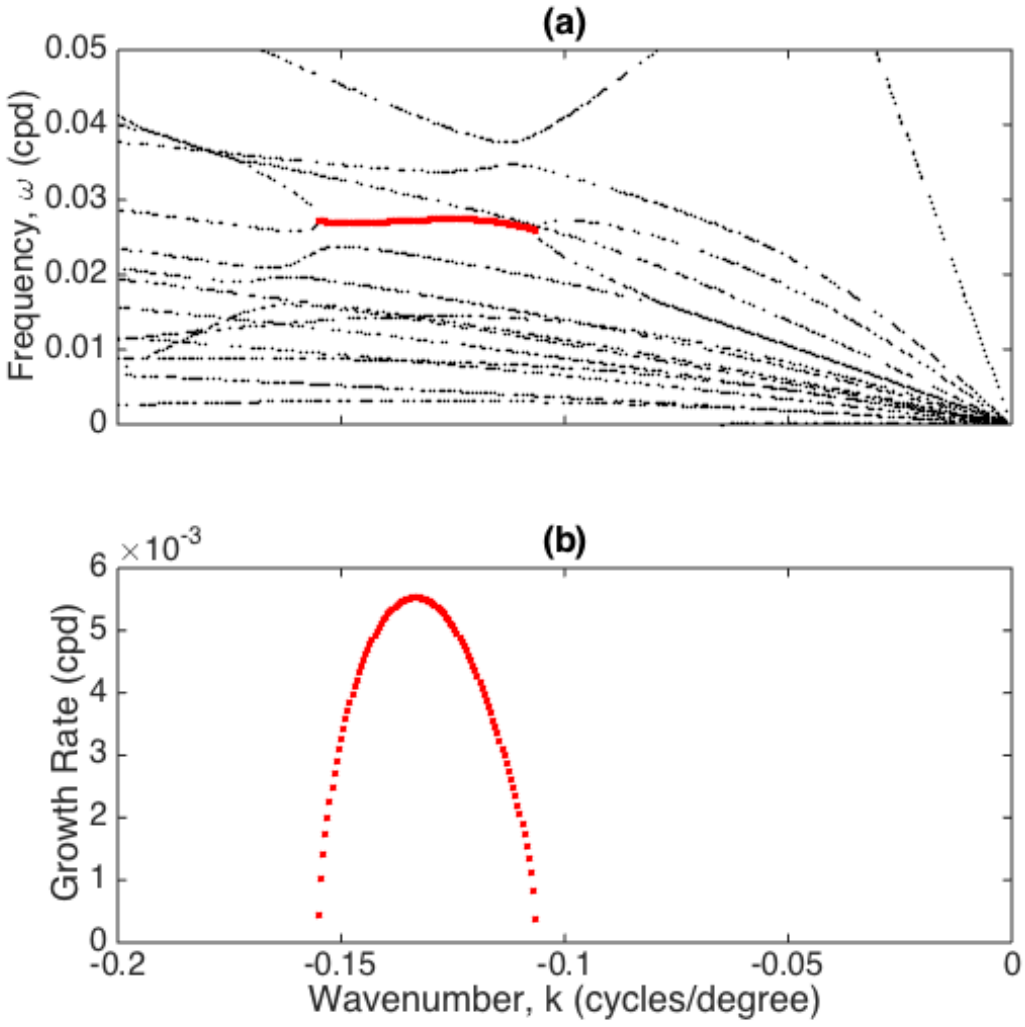

Figure 3-16: (a) Dispersion curves resulting from the 1.5-layer, equatorial β-plane model of Appendix 3.A with $U(y)$ from June 2010 SODA reanalysis. The fastest growing mode is highlighted in red. (b) Growth rate of the fastest growing mode in (a).

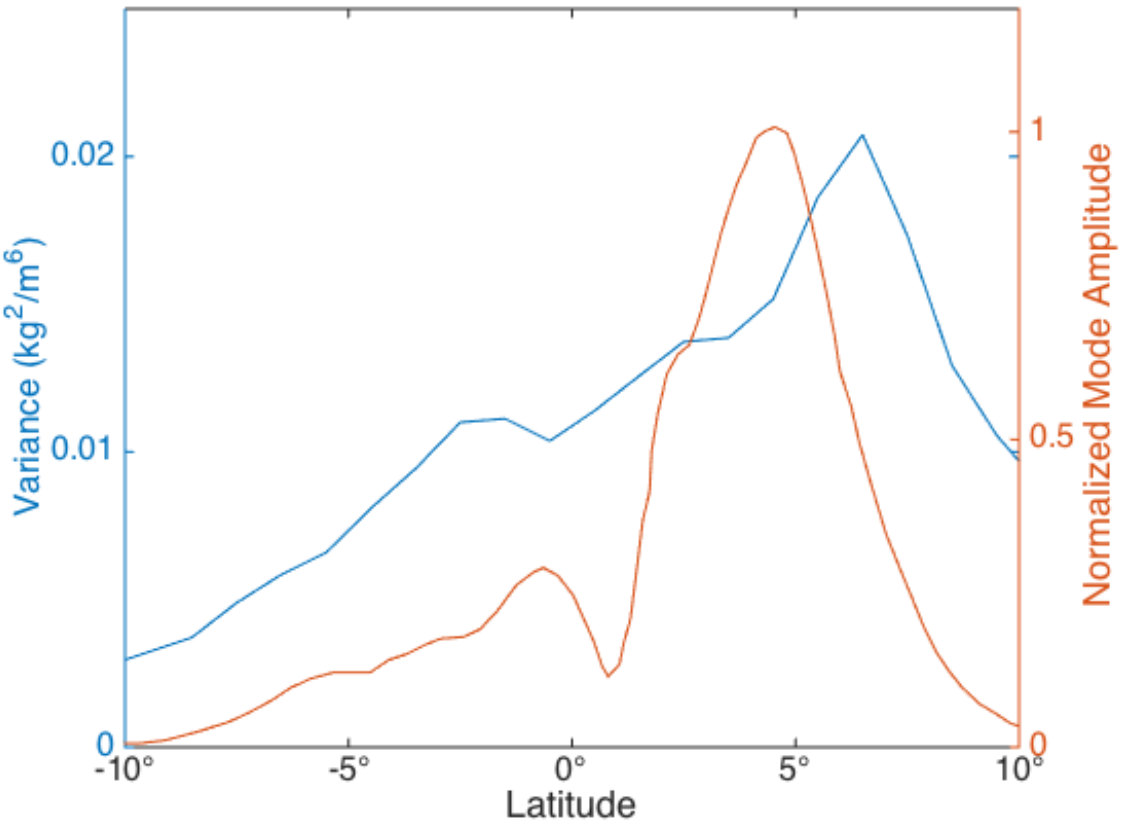

Figure 3-17: Spectral variance of Argo potential density averaged over $150° - 280°$ longitude, and $0 - 200$ dbar pressure and normalized meridional mode of the fastest growing mode from *Lyman et al.* (2005).

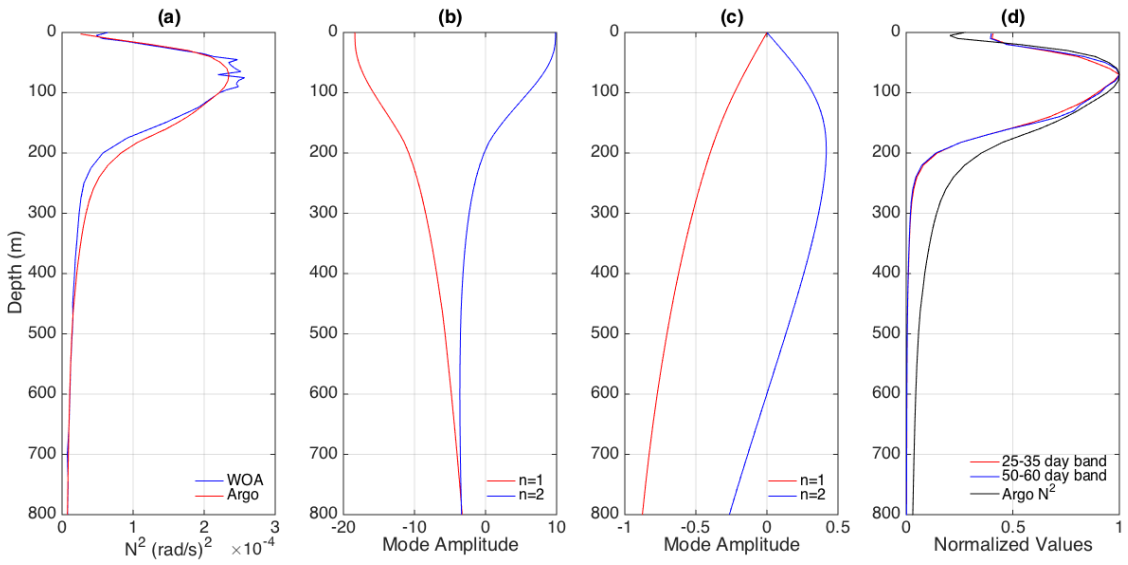

Figure 3-18: (a) N^2 calculated from WOA data (*Boyer et al.*, 2013) and Argo data *Roemmich and Gilson* (2009). First and second vertical baroclinic modes calculated from Argo data for (b) horizontal velocity and pressure and (c) vertical velocity. (d) Argo N^2 profile compared to average potential density variance in the 25 – 35 day period band and 50 – 60 day period band, consistent with two peaks with wavelengths near 1200 km in Figure 3-15. Profiles in (d) are normalized to fall between 0 and 1. All profiles are averaged over 10°S – 10°N, 150° – 280° longitude.

$U(y)$ between SODA and the zonal velocity data used in *Lyman et al.* (2005). However, the maxima in spectral variance of Argo potential density occur near maxima in potential density gradient, indicating the differences in maxima may reflect the propagation of TIWs through non-zero potential density gradients. Despite these differences, the consistency between Argo and the results of *Lyman et al.* (2005) indicate that TIWs observed between 0-200 m in Argo observations are likely due to a resonance between Rossby waves, impacted by the strong zonal equatorial current system.

The spectral TIW signal seen in potential density, temperature or salinity is caused by either horizontal or vertical advection of those properties by TIWs in regions where an associated gradient exists. The expected TIW vertical structure can be determined by calculating the first two baroclinic modes of horizontal (Figure 3-18b) and vertical (Figure 3-18c) velocity obtained from the numerical solution of the vertical structure equation described in *Pedlosky* (1987c). This calculation relies on the full-depth profile of the Brunt-Väisälä frequency (Figure 3-18a):

$$N^2 = \frac{-g}{\rho_0}\frac{\partial \rho(z)}{\partial z} \tag{3.2}$$

where N^2 is the Brunt-Väisälä frequency, g is the acceleration due to gravity, ρ_0 is the water parcel density, and $\partial\rho(z)/\partial z$ is the vertical density gradient of the water column. Argo data only covers 0 – 2000 m depth, while the WOA data extends down to 5000 m depth. The Argo mean N^2 profile is extended to the WOA maximum depth by using WOA data for 2000 – 5000 m depth. This modified Argo profile also uses WOA data for the top 10 m depth due to limitations in Argo sampling near the surface. The first two baroclinic modes in vertical and horizontal velocity using WOA and Argo data are similar despite differences in N^2 profiles near 100 m depth. The spectral variance in the first and second baroclinic Rossby wave frequency bands closely follow the normalized N^2 profile (Figure 3-18b) rather than the baroclinic modal solutions. This is possibly a result of two mechanisms: 1) observing a wave signal that depends on the advection of potential density, reflected in the vertical density gradient in Equation 3.2, or 2) vertical structure of equatorial waves is modified by the presence of a mean zonal flow (*McPhaden et al.*, 1987), with a result that is similar in shape to that of N^2. An approach that utilizes a direct dynamical connection to TIWs, such as isopycnal heave, may result in a clearer depiction of the vertical structure of TIWs that is more consistent with the baroclinic modes.

3.3.5 Resolution and Error

The *Roemmich and Gilson* (2009) mapped data does not include an objective mapping error estimate; however, *Gasparin et al.* (2015) compute an objectively mapped equatorial Pacific dataset consistent with the procedures and resolution of *Roemmich and Gilson* (2009) that includes the time domain, estimates of mapping error, and an improved objective mapping spatial covariance function (Figure 3-19). Although it is not directly applicable to the data used in this analysis, the objective mapping error can be used to provide a starting point for understanding error in the *Roemmich and Gilson* (2009) data. Mean error for the *Gasparin et al.* (2015) data over the 2004 – 2014 record, in % of variance, remains below 30% over the spatial domain of interest.

3.4 Conclusion

The *Roemmich and Gilson* (2009) objectively mapped Argo product provides a gridded set of observations convenient for spectral analysis of Tropical Instability Waves. This product

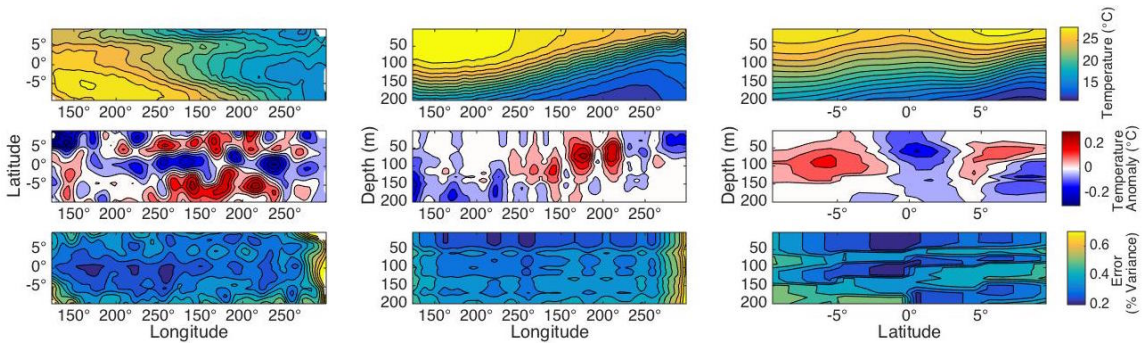

Figure 3-19: Temperature (upper plots), temperature anomaly (middle plots) and interpolation error (% of variance) from the objective mapping of Argo data (*Gasparin et al.*, 2015). The temperature field includes the sum of temperature anomaly, annual temperature anomaly, and temperature mean.

is used to observe the three-dimensional structure of TIWs using temperature, salinity, and potential density across the equatorial Pacific from the surface to 200 m depth. Spectral variance of Argo observations at the surface are consistent with SST and SSH measurements from GHRSST and Aviso (Figures 3-6 and 3-7).

The nature of Argo allows for the extent of these observations to expand to the subsurface region. Strong TIW signals are seen along the thermocline, deepening as they propagate westward (Figure 3-12). Zonal wavenumber-frequency diagrams (Figure 3-15) in regions of strong TIW signal at the depth of the thermocline show a significant spectral peak that is consistent with the dispersion curve of *Lyman et al.* (2005). The vertical profile of meridional and vertical wave amplitude follow the N^2 profile for this region. Another dynamical approach to using Argo data to observe the three-dimensional structure of TIWs would be to repeat this type of analysis using isopycnal heave, rather than potential density. The available gridded Argo datasets do not have sufficiently high vertical resolution to resolve relatively small changes in isopycnal depth, requiring the use of a new gridded product that maps individual Argo profiles onto isopycnals rather than pressure surfaces. A future study will use a similar approach to observing the vertical structure of TIWs by applying the techniques of this study to isopycnal heave rather than advection of potential density, providing a direct dynamical link between TIW propagation and observations.

3.A Equatorial β-plane Model

The equatorial β-plane model is two-dimensional in the meridional direction (y) and depth (z). Input parameters include:

- $y_{\max}$and $y_{\min}$: northern and southern boundaries of the domain in distance (km) from the equator
- $\beta(y)$: the variation of the Coriolis parameter with latitude, $\frac{\partial f}{\partial y}$
- $U(y,z)$: the mean zonal flow, $U_0(y)$ (upper layer, as a function of latitude) and $U_1 = 0$ (lower layer)
- ρ_*: mean density in the upper layer
- k: zonal wavenumber
- $H_0(y)$: initial depth used to calculate $H(y) = H_0(y) + \int_{y_{\min}}^{y_{\max}} \frac{\partial H}{\partial y} dy$, where $\frac{\partial H}{\partial y} = -\beta y U_0$ as a function of latitude

Additional problem specifications:

- $U_0(y)$ and ρ_* are calculated by integrating SODA reanalysis zonal velocity over a chosen depth (see Section 3.A.2 and Figure 3-21b).
- $w' = 0$ at top and bottom boundaries (rigid lid, flat bottom)
- Density (ρ) can be represented as $\rho_{total}(x,y,z,t) = \rho_* + \rho_0(y,z) + \epsilon\rho'(x,y,z,t)$ where ρ_0 weakly varies with y compared to z or $\rho_0(y,z) \approx \rho_0(z) + \epsilon\rho_0(y,z)$ (*Proehl*, 1998).
- $v' = 0$ at the northern and southern boundaries.
- u, v, p, and ρ below refer to the amplitude of the perturbation (wave) quantities and the prime notation is dropped. For example, the zonal velocity wave function can be written as $u'(x,y,t) = \tilde{u}(y)e^{i(kx-\sigma t)}$. After this point, u refers to the $\tilde{u}(y)$ part of the wave solution. The z-direction is not included in the perturbation solution as this is a 1.5-layer model. u, v, and p, are functions of y.
- g' refers to reduced gravity defined as

$$g' = g\frac{\rho_{\text{lower}} - \rho_{\text{upper}}}{\rho_{\text{lower}}}. \tag{3.3}$$

3.A.1 Eigenvalue Problem Derivation

The following describes the formulation of the eigenvalue problem that is solved numerically. We start with the equatorial β-plane shallow water equations, linearized about a mean zonal flow:

$$\frac{\partial u}{\partial t} + U_0\frac{\partial u}{\partial x} + \cancelto{0}{\frac{\partial U_0}{\partial x}}u + \frac{\partial U_0}{\partial y}v + \frac{\partial U_0}{\partial z}\cancelto{0}{w} - \beta yv = -\frac{1}{\rho_*}\frac{\partial p}{\partial x} \tag{3.4}$$

$$\frac{\partial v}{\partial t} + U_0\frac{\partial v}{\partial x} + \beta yu = -\frac{1}{\rho_*}\frac{\partial p}{\partial y} \tag{3.5}$$

$$\frac{\partial \rho}{\partial t} + U_0\frac{\partial \rho}{\partial x} + \frac{\partial \rho_0}{\partial y}v + \frac{\partial \rho_0}{\partial z}w = 0 \tag{3.6}$$

$$\frac{\partial u}{\partial x} + \frac{\partial v}{\partial y} + \frac{\partial w}{\partial z} = 0 \tag{3.7}$$

$$\frac{\partial p}{\partial z} = -g'\rho \tag{3.8}$$

Assuming u, v, and p are proportional to $e^{i(kx-\sigma t)}$, taking derivatives and rearranging:

$$-i\sigma u + ikU_0u + \frac{\partial U_0}{\partial y}v - \beta yv = -\frac{ik}{\rho_*}p \tag{3.9}$$

$$-i\sigma v + ikU_0v + \beta yu = -\frac{1}{\rho_*}\frac{\partial p}{\partial y} \tag{3.10}$$

$$-i\sigma\rho + ikU_0\rho + \frac{\partial \rho_0}{\partial y}v + \frac{\partial \rho_0}{\partial z}w = 0 \tag{3.11}$$

$$iku + \frac{\partial v}{\partial y} + \frac{\partial w}{\partial z} = 0 \tag{3.12}$$

$$\frac{\partial p}{\partial z} = -g'\rho \tag{3.13}$$

Solving Equation 3.13 for ρ:

$$\rho = \frac{-1}{g'}\frac{\partial p}{\partial z} \tag{3.14}$$

Substituting Equation 3.14 into Equation 3.11:

$$\frac{ikU_0}{g'}\frac{\partial p}{\partial z} + \frac{\partial \rho_0}{\partial y}v + \frac{\partial \rho_0}{\partial z}w = i\sigma\frac{\partial p}{\partial z} \tag{3.15}$$

Solving Equation 3.12 for w_z and integrating over the top layer of depth $H(y)$:

$$\frac{\partial w}{\partial z} = -iku - \frac{\partial v}{\partial y} \rightarrow w = -H\bigg(- iku - \frac{\partial v}{\partial y}\bigg) \tag{3.16}$$

Substituting Equation 3.16 into 3.15 for w:

$$\frac{ikU_0}{g'}\frac{\partial p}{\partial z} + \frac{\partial \rho_0}{\partial y}v + \frac{\partial \rho_0}{\partial z}\left[H\left(iku + \frac{\partial v}{\partial y}\right)\right] = \frac{i\sigma}{g'}\frac{\partial p}{\partial z} \tag{3.17}$$

Integrating Equation 3.17 with respect to z is equivalent to multiplying by $H(y)$ since this is 1.5-layer model with upper layer depth $H(y)$. Also, ρ_0 is weakly varying in y, so $\int_{-H}^{0} \frac{\partial \rho_(y,z)}{\partial z} \approx \rho_*$. Integration and multiplying through by g':

$$ikU_0 p + g'H\frac{\partial \rho_0}{\partial y}v + \rho_* g'H\left(iku + \frac{\partial v}{\partial y}\right) = i\sigma p \tag{3.18}$$

The second term in Equation 3.18 can be written using integration by parts in y and noting that ρ_0 is weakly varying in y:

$$\int \frac{\partial \rho_0}{\partial y}\frac{\partial H}{\partial y}dy = H\frac{\partial \rho_0}{\partial y} - \int H\cancelto{0,\sim\epsilon^2}{\frac{\partial^2 \rho_0}{\partial y^2}}dy \tag{3.19}$$

which can be written as:

$$H\frac{\partial \rho_0}{\partial y} = \rho_*\frac{\partial H}{\partial y}. \tag{3.20}$$

Equation 3.18 can then be written as:

$$ikU_0 p + g'H\rho_*\frac{\partial H}{\partial y}v + \rho_* g'H\left(iku + \frac{\partial v}{\partial y}\right) = i\sigma p \tag{3.21}$$

Rearranging Equations 3.9, 3.10, and 3.21 and multiplying all equations by $-i$:

$$kU_0 u + i\left(\beta y - \frac{\partial U_0}{\partial y}\right)v + \frac{k}{\rho_*}p = \sigma u \tag{3.22}$$

$$-i\beta y u + kU_0 v - \frac{i}{\rho_*}\frac{\partial p}{\partial y} = \sigma v \tag{3.23}$$

$$\rho_* g'Hku - ig'\rho_*\left[\frac{\partial H}{\partial y}v + H\left(\frac{\partial v}{\partial y}\right)\right] + kU_0 p = \sigma p \tag{3.24}$$

Parameter	Value
ρ_1	1025.0 kg m^{-3}
ρ_2	1028.0 kg m^{-3}
g'	0.029 m s^{-2}
H_0	240 m

Table 3.1: Input parameters for 1.5-layer, equatorial wave model

Written in matrix form:

$$\begin{bmatrix} kU_0 & i\left(\beta y - \frac{\partial U_0}{\partial y}\right) & \frac{k}{\rho_*} \\ -i\beta y & kU_0 & -\frac{i}{\rho_*}\frac{\partial}{\partial y} \\ \rho_* g' H k & -ig'\rho_*\left[\frac{\partial H}{\partial y} + H\left(\frac{\partial}{\partial y}\right)\right] & kU_0 \end{bmatrix} = \sigma \begin{bmatrix} u \\ v \\ p \end{bmatrix} \tag{3.25}$$

The model consists of solving this eigenvalue problem for a specified $U(y)$. A offset v-grid is chosen in order to remain consistent with boundary conditions $v = 0$ at $y_{\max}$ and $y_{\min}$, with u and p coincident, and v located in the middle of u, p points (Figure 3-20). This gives N grid points for v and $N+1$ grid points for u and p. The boundary conditions, $v = 0$ at the northern and southern boundaries, are implemented outside the domain at ghost v grid points. The resultant eigenvalues consist of a real part and imaginary part, where the real part corresponds to the wave frequency and the imaginary part to the growth rate of each meridional mode. The resultant eigenvectors consist of $3N+2$ elements, corresponding to the wave amplitude $u(y)$, $v(y)$, and $p(y)$ eigenvectors concatenated together. These give the meridional structure of the wave solutions to the system corresponding to each wave frequency.

3.A.2 Model Input Parameters

The model is run with meridional boundaries at 10°S and 10°N with a meridional resolution of 1°. Potential density is calculated from SODA reanalysis data. Time and longitude ranges over which potential density is averaged are chosen to correspond to regions of high TIW activity. The longitude range of 120°W – 93°W extends from near the middle of the region of high spectral energy in the 30-day band to just west of the Galápagos Archipelago. The time period of June 2010 corresponds to the beginning of a strong TIW period, chosen via qualitative assessment of Figure 3-1.

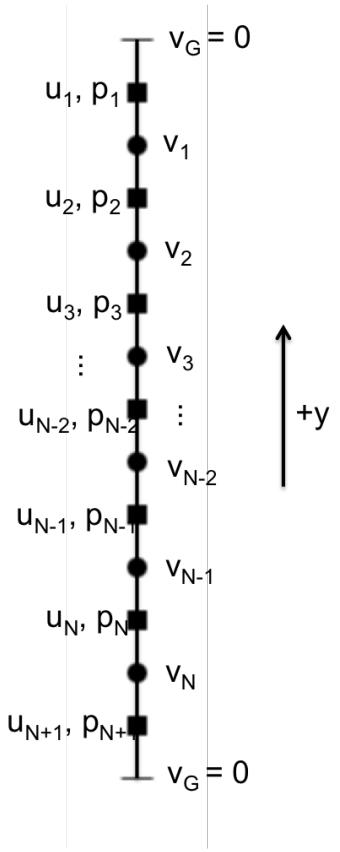

Figure 3-20: Grid used to solve the equatorial β plane eigenvalue problem with $v = 0$ at the y boundaries. The number of v grid points is N, and the number of u, p grid points is $N + 1$. Squares indicate v grid points and circles correspond to u and p points. The boundary conditions are implemented using ghost points outside the domain at $v_G = 0$.

We estimate upper and lower layer density (ρ_1 and ρ_2) by taking the average potential density over the latitude range used in the model, the chosen time period and longitude range, and over the nominal depth of the appropriate layer ($0 - H_0$ and $H_0 -$ bottom for the upper and lower layers, respectively). These are used to calculate reduced gravity (Equation 3.3).

To check the validity of these parameters, the radius of deformation is calculated at both the equator (Equation 3.27) and at the limits of the meridional domain, 10°S and 10°N (Equation 3.26), with $L = 10°$ latitude and β calculated at either the equator or 10° latitude.

$$R_{rn} = \frac{g' H_0}{\beta L} \tag{3.26}$$

$$R_{eq} = \sqrt{\frac{c}{2\beta}} \tag{3.27}$$

Given the parameters in Table 3.1, the calculated deformation radii are $R_{rn} = 110$ km and $R_{eq} = 320$ km, consistent with the World Ocean Atlas values for the associated latitudes (*Boyer et al.*, 2013).

The gradient of $U(y)$ is calculated by taking the finite difference of adjacent $U(y)$ at u, p grid points (Figure 3-21d). These are linearly interpolated to find $U(y)$ at v grid points. The gradient of $H(y)$ is calculated from geostrophic balance applied to the mean zonal flow per Equation 3.29.

$$\beta y U = -\frac{1}{\rho_1} \frac{\partial P}{\partial y} \tag{3.28}$$

where P is the pressure in the first layer in the unperturbed state. Substituting $P = \rho_* g H$ into Equation 3.28:

$$\frac{\partial H}{\partial y} = -\frac{\beta y U}{g} \tag{3.29}$$

and after rearranging, we obtain $H_1(y)$:

$$H(y) = \int_{y_{\min}}^{y} -\frac{\beta y U}{g} dy + H_0. \tag{3.30}$$

3.A.3 Numerical Methods

The eigenvalue problem defined by Equation 3.25 is solved at each zonal wavenumber (k) using MATLAB 2012b's eig.m function. Each term in Equation 3.25 actually represents a

sub matrix with dimensions $N \times N$ (middle row, v) or $N+1 \times N+1$ (top and bottom rows, u and p), due to their y-dependence. The eigenvalues and eigenvectors, although associated with each other, are not explicitly sorted in any particular order. In order to associate the maximum growth rate curve with an eigenvector, the results of eig.m are sorted to maintain consistency from one k step to another.

Boundary conditions are implemented within the finite difference approximations at the ends of the meridional domain where $v = 0$. In Equation 3.25, p rows contain a $\partial v/\partial y$ term. Away from the northern and southern limits of the domain, that term is expressed at each u, p gird point using the form of Equation 3.31.

$$\frac{\partial v}{\partial y} \approx \frac{v_n - v_{n-1}}{\Delta y} \tag{3.31}$$

At the boundaries, $v_0 = 0$ and $v_{N+1} = 0$, where v has $n = 1, 2, 3...N-1, N$ elements and v_0, v_{N+1} are ghost points and lie outside of the domain. For p_1 and p_{N+1}, the $\partial v/\partial y$ terms become Equations 3.32 and 3.33, respectively.

$$\frac{\partial v}{\partial y}_{\text{north}} \approx \frac{0 - v_1}{\Delta y} \tag{3.32}$$

$$\frac{\partial v}{\partial y}_{\text{south}} \approx \frac{v_N - 0}{\Delta y} \tag{3.33}$$

Similarly, the v rows of Equation 3.25 contain a $\partial p/\partial y$ term. Since all v grid points lie between u, p grid points, no boundary conditions are necessary and the derivative can be approximated at all v grid points using Equation 3.34.

$$\frac{\partial p}{\partial y} \approx \frac{p_n - p_{n-1}}{\Delta y} \tag{3.34}$$

For non-derivative terms multiplied by a quantity on a different grid (for example, the $-i\beta y$ term of the second row on the v grid, multiplied by u), the mean of the values of the surrounding offset grid points is taken, as in Equation 3.35 at grid point v_n.

$$-i\beta y u|_{vn} \approx -i\beta y \left(\frac{u_n + u_{n+1}}{2} \right) \tag{3.35}$$

At the edges of the domain, v ghost points are used as in the differentiation case (Equation 3.31).

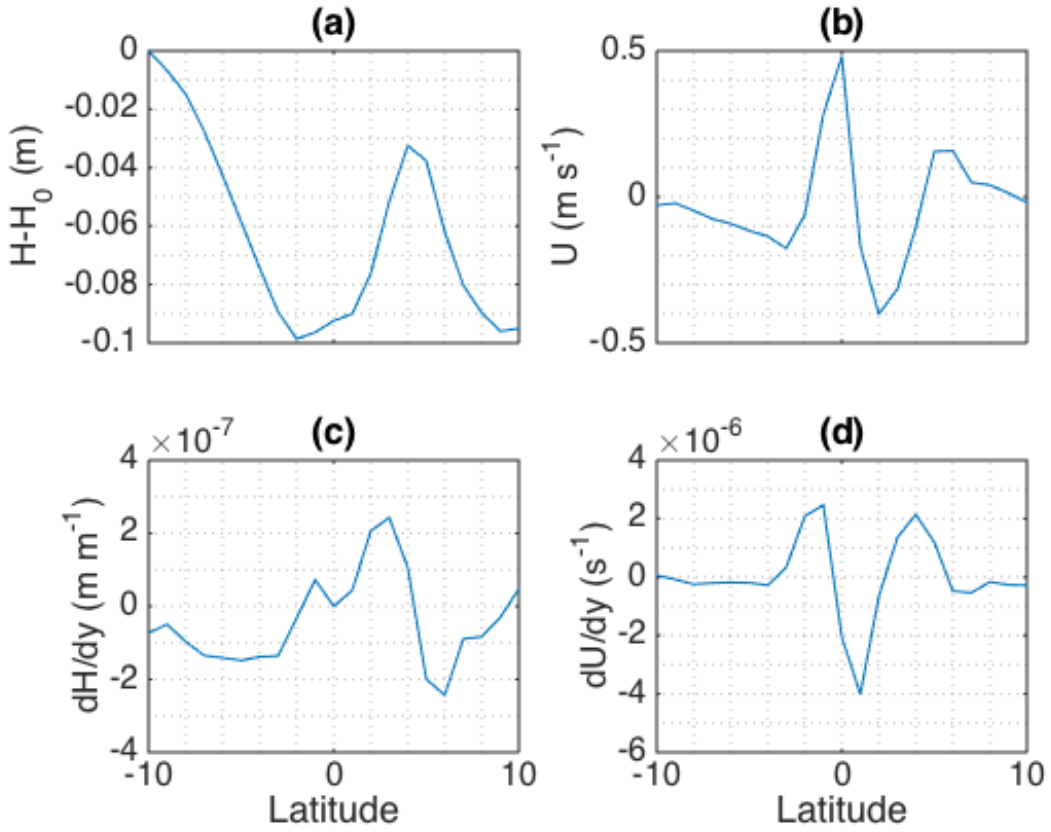

Figure 3-21: Model input parameters for the equatorial β plane eigenvalue problem: (a) Variation from $H_0 = 240$ m in the mean first layer depth ($H(y)$), (b) mean zonal current, $U(y)$ as calculated from SODA, (c) variation of the mean first layer depth with latitude, $\frac{\partial H}{\partial y}(y)$, and (d) variation of the mean zonal current with latitude, $\frac{\partial U}{\partial y}(y)$. The zero mean zonal current case is shown in blue, and the mean zonal current calculated from SODA is shown in red.

3.A.4 Equatorial β-plane Wave Model Validation

The mean zonal current is initially taken to be zero (Figure 3-21, blue curves), to confirm that the model reproduces well known solutions to the $U(y) = 0$ equatorial wave problem (e.g., *Matsuno*, 1966). Analytic solutions to Equations 3.9 – 3.13 closely match the eigenvalue solution with $U(y) = 0$ (Figure 3-22). Brunt-Väisälä frequency profiles calculated using both Argo data and the World Ocean Atlaas data (*Boyer et al.*, 2013) are compared in Figure 3-18a. The profiles are sufficiently close to expect similar results for modal phase speeds from vertical mode calculations.

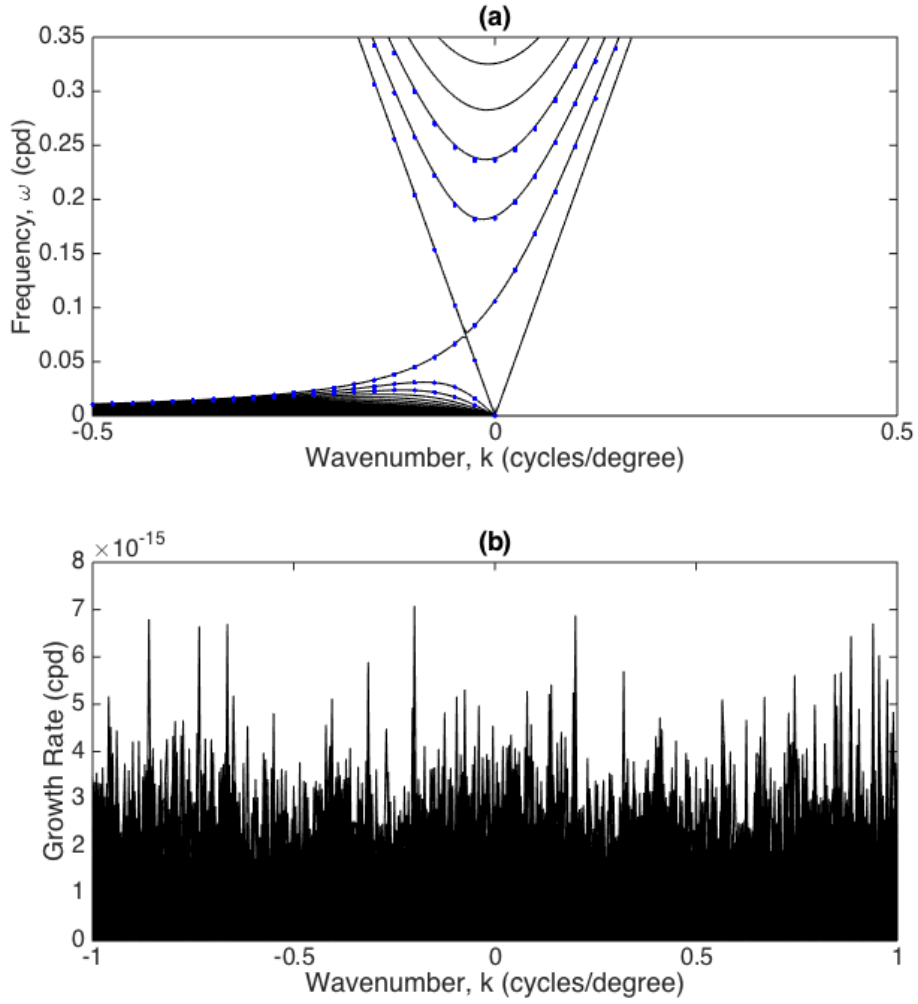

Figure 3-22: Dispersion curve and growth rate plots from the solution of the u, v, p eigenvalue problem with $U(y) = 0$ are shown in black line. Blue stars indicate well-known analytic solutions to the $U(y) = 0$ problem for the $n = 0, 1, 2$ cases. The growth rate for this case is zero to within machine precision.

Conclusion

Summary of Findings

The Galápagos Cold Pool, just west of the Galápagos Archipelago, is a region of cold SST maintained by upwelling associated with the equatorial current system. GCP variability is potentially impacted by changes in the EUC and SEC, and the passage of TIWs. Prior to the ROGER program, high-resolution, subsurface observations of temperature, salinity, and velocity over a multi-year period were not available in this region. While ocean gliders are commonly used to measure subsurface temperature, salinity, and pressure, Spray gliders used during ROGER additionally measured horizontal currents relative the the gliders which, combined with the horizontal surface displacement over the dive, provides vertical profiles of absolute horizontal velocity for each dive (*Todd et al.*, 2017). These observations eliminate the need to rely on estimates of geostrophic velocity from density measurements at the equator where geostrophy fails, and include ageostrophic currents. The deployment of ROGER gliders during 2013 – 2016 provides unprecedented, high spatial resolution, subsurface observations of a range of ocean processes in an interesting, dynamic region. The unique capabilities of Spray gliders allow us to observe the path of the EUC as it reaches the Galápagos Archipelago, estimate horizontal transport and upwelling, consider the conservation of Ertel Potential Vorticity and a Bernoulli function, and characterize instabilities diagnosed from the average Ertel potential vorticity field. We then use the gridded Argo product from *Roemmich and Gilson* (2009) to examine spectral variance of TIWs in three-dimensions.

In Chapter 1, glider measurements of current velocity during the two-month time period of April – May 2016 show that the EUC bifurcates into two branches that advect EUC water north and south of the Galápagos Archipelago (Figures 1-5 and 4-1). These branches have similar velocity magnitude and similar volume transport. Depth-integrated horizontal

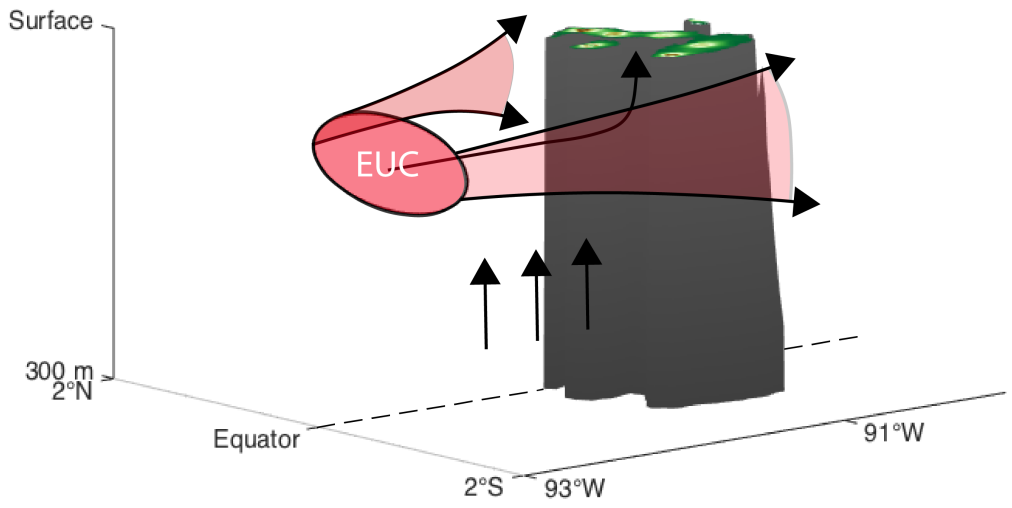

Figure 4-1: Schematic of upwelling and the bifurcation of the EUC in the region west of the Galápagos Archipelago.

transport is 3.6 ± 0.7 Sv out of the volume (V_{gl}), indicating net upwelling over the upper 300 m. At each depth level, net horizontal transport is not generally zero (Figure 1-7b). Integrating net horizontal transport from the surface results in an estimate of average vertical velocity over A_{gl}. A local maximum of $(1.7 \pm 0.6) \times 10^{-5}$ m s^{-1} exists at a depth of 25 m. This value is comparable to general equatorial upwelling within 2° latitude of the equator. As our estimate of vertical velocity is an average over A_{gl}, we expect higher values of vertical velocity in the region very close to the Galápagos Archipelago where SST reaches a minimum (Figure 1-1). Upwelling reaches a maximum value of $(8.0 \pm 1.6) \times 10^{-5}$ m s^{-1} near 300 m. This implies that water upwelled into V_{gl} at 300 m depth is a result of wind- and current-driven dynamics relating to the net divergence in the upper 300 m.

We estimate the bifurcation latitude of the EUC to be 0.4°S during April – May 2016 from volume transport as a function of salinity class in Chapter 1. In Chapter 2, this value is estimated to be 0.32°S during March – April 2015. As these estimates are close to the latitude of the center of the Galápagos Archipelago (0.4°S), it is likely that the bifurcation of the EUC into two branches is primarily topographically driven by the position of archipelago. As the EUC meanders about an average meridional position, transport south or north of the archipelago varies depending on the position of the EUC with respect to the bifurcation

latitude. When the average position of the EUC is south of the bifurcation latitude, the south branch of the EUC transports a greater amount of water originating from the EUC south of the archipelago.

Velocity, temperature, and salinity sections enable us to construct high-resolution relative vorticity sections just west of the Galápagos Archipelago, which provide estimates of EPV (Chapter 2) that include both the geostrophic and ageostrophic contributions to velocity. *Stevens* (1983) show that a Guassian jet centered just off the equator can result in EPV having sign opposite to that of the Coriolis parameter between the core of the jet and the equator. This model can be considered an approximate representation of the EUC, which has an average meridional position of about 0.2°S (*Johnson et al.*, 2001). In Chapter 2, time-average sections of EPV estimated from glider measurements indicate EPV with sign opposite to that of the Coriolis parameter in the region between the EUC and the equator during three-year and two-month averages. This is primarily a result of velocity gradients that exist between the EUC and SEC.

Pedlosky (1987a) show that a 2.5-layer, inertial model explains the eastward-flowing EUC. In the inertial model, EPV and a Bernoulli function are conserved along streamlines, as the model assumes inviscid, adiatic, steady-state flow. Estimates of EPV and the Bernoulli function sections along 93W and SD from glider observations, resulting from the average position and shape of the EUC, suggest that EPV and the Bernoulli function are advected north or south of the Galápagos Archipelago when the EUC bifurcates into two branches. Similar patterns are noted between 93W and SD for both quantities, qualitatively indicating EPV and the Bernoulli function are conserved along streamlines, consistent with the inertial theory of the EUC developed by *Pedlosky* (1987a). Glider measurements of temperature and salinity are not available for the north branch of the EUC; however, we observe advection of EPV having sign opposite to that of the Coriolis parameter south of the archipelago during the April – May 2016 time frame. At this time, the average position of the EUC core is near 0.7°S. When the meridional position of the EUC core is south of the bifurcation latitude, some EPV with sign opposite to that of the Coriolis parameter that exists between the EUC core and the equator is advected south of the archipelago.

The cross-stream gradient of the EPV field can be used to diagnose whether a necessary condition for barotropic or baroclinic instability is met along 93W and SD. Barotropic and baroclinic instability are considered mechanisms that generate TIWs, generated by

shear associated with the equatorial current system. Spray glider observations provide a unique opportunity to observe the cross-stream EPV gradient and apply these observations to barotropic and baroclininc instability. The necessary condition for barotropic instability, that $\partial Q/\partial y$ changes sign in the horizontal plane, is met during all three time periods along 93W and SD, suggesting that barotropic instability may be responsible for TIWs within the meridional domain 2°S – 2°N. The necessary condition for baroclininc instability, that $\partial Q/\partial y$ changes sign in the vertical plane, is met in limited regions during TP2, but is less apparent than barotropic instability.

Conditions conducive to inertial and/or symmetric instability can persist on time scales of months to years as long as the meridional position of the EUC core is sufficiently south (or north) of the equator, resulting in EPV with sign opposite to that of the Coriolis parameter. If the position of the EUC core is south of the bifurcation latitude, inertial and/or symmetric instability may also exist within in the region of the south branch of the EUC. Near the equator, the Coriolis parameter approaches zero and conditions conducive to inertial and symmetric instability can result from relatively small horizontal and vertical shears, respectively. Estimates of EPV from three-year and two-month averages of glider measurements suggest that conditions conducive to inertial and symmetric instabilities associated with the EUC and the south branch of the EUC can persist over months or years with e-folding timescales between 2 – 13 days. Vertical mixing due to symmetric instability near the surface may impact the GCP, by mixing relatively warm surface waters with the colder subsurface waters of the EUC. EPV estimates from glider measurements necessarily neglect cross-track gradients, as gliders only obtain along-track measurements. The south branch of the EUC is located along the boundary with the Galápagos Archipelago, where cross-track gradients may not be negligible. Additionally, friction may play an important role that is not accounted for in this analysis. Incorporating these factors could potentially result in conditions stable to inertial/symmetric instability, particularly along the south branch of the EUC.

In Chapter 3, we find the period and wavelength associated with TIWs from spectral variance of Argo temperature, salinity, and potential density to be 35 days and 1250 km, respectively (Figure 3-15). These values are consistent with those predicted by *Lyman et al.* (2005), who attributes TIWs to a resonance between Rossby waves. A 1.5-layer, equatorial β-plane model resolves unstable behavior, but the fastest growing mode has a period of 40

days and a wavelength of 750 km. The meridional structure of spectral variance of potential density in the TIW band is similar to the meridional structure predicted by *Lyman et al.* (2005); however, maxima in spectral variance occur farther poleward in Argo observations compared to maxima predicted by *Lyman et al.* (2005). This may be partially attributed high potential density gradients where maxima are observed and to the sensitivity of the model to the mean zonal flow, which varies depending on the equatorial current system. Spectral variance in the TIW band extends to 200 m depth and potentially deeper, following the N^2 profile observed by Argo. This implies that TIWs have the potential to impact upwelling just west of the Galápagos Archipelago directly or via interaction with the EUC.

Implications of Results

The GCP is likely maintained by upwelling, vertical mixing, or a combination of these. Glider observations show that the two branches of the EUC transport approximately all of the volume around the Galápagos Archipelago. There is sufficient uncertainty in the branch transports so that the EUC likely supplies anomalously cold SST of the GCP. Convergence of the EUC as it approaches the archipelago results in enhanced positive vertical velocity above the EUC core and decreased vertical velocity below the EUC core. Vertical spreading of the two branches of the EUC also results in divergence below the EUC core and increased upwelling below 75 m. Near the surface, conditions conducive to symmetric instability may result in vertical mixing that can impact SST associated with the GCP by mixing warmer surfer waters with the cooler subsurface waters of the EUC. Conditions conducive to symmetric instability are not apparent during TP1, suggesting that vertical mixing (along-isopycnal mixing with titled isopycnals) due to symmetric instability is not responsible for the long-term existence of the GCP. As inertial instability results in horizontal mixing, it also is unlikely to play a primary role in the existence of the GCP. Both symmetric and inertial instability could, however, impact the horizontal extent of the GCP.

The minimum average SST resolved by GHRSST data is near 22°C, which corresponds with an isotherm depth of about 20 m at the latitude of the minimum SST value. Equatorial Ekman transport and upwelling above the EUC core could account for the existence of the GCP during this time period, since water only needs to travel a vertical distance of 20 m between 93W and the GCP to reach the surface. The minimum average value of SST is likely

the result of smoothing and the limited spatial resolution of satellite observations, so may be lower than observed. However, the estimated vertical velocity profile indicates upwelling in the entire upper 300 m, consistent with the regional ocean model results of *Karnauskas et al.* (2007), so an additional mechanism driving upwelling must be present. The section of average meridional velocity along 93W shows a meridional divergence that extends to 300 m depth. This divergence cannot simply by balanced by convergence of the EUC as it slows during it's approach to the Galápagos Archipelago since the EUC is confined to the upper 150 m. The meridional divergence suggests that an additional, unknown mechanism results in upwelling between 93W and the archipelago, with the effects of the equatorial current system superimposed on it.

Sections of EPV and Bernoulli function appear to be qualitatively conserved between 93W and SD away from boundary currents. Since conservation of both quantities requires inviscid, adiabatic flow, the inertial model of *Pedlosky* (1987a) is supported by glider observations. Models including friction tend to resolve the asymmetry in the average meridional position of the EUC, suggesting that the structure of the EUC as an eastward flowing current confined to the equator is an inertial process, while including frictional terms improves the ability of the model to resolve details of the circulation.

Variability in the GCP and the equatorial current system between 2°S and 2°N is not considered here. Differences in zonal velocity, EPV, and Bernoulli functions between TP1–TP3 indicate a high amount of variability in all three quantities. This includes variability in the meridional position of the EUC core prior to bifurcation due to the topographic barrier of the Galápagos Archipelago. Changes in wind stress result in meanders of the EUC about an average latitude of about 0.5°S, which has the potential to cause the EUC to meander to either side of the bifurcation latitude. The relative sizes of volume transport of the north and south branches of the EUC are expected to depend on the position of the EUC with respect to the bifurcation latitude (Figure 4-1). The eastern Pacific cold tongue may be impacted by changes in the branches of the EUC, as it reaches the Galápagos Archipelago from the east (*Kessler*, 2006).

TIWs are an additional source of variability of the GCP, due to baroclinic or barotropic instabilities that arise from shear within the equatorial current system. The along-track gradient of EPV meets a necessary condition for barotropic instability in the upper 100 m along 93W and SD during all three time periods, while the necessary condition for baroclinic

instability is met only in more limited regions during TP2. TIWs originating from these instabilities as far east as SD could induce upwelling and downwelling during their westward propagation through the region. Glider observations could be used in conjunction with SST observations to examine either a TIW-related signal is apparent in the GCP.

Future Work

To further understand the mechanisms behind upwelling at the GCP, a regional ocean model analysis could be compared to the results of glider observations. The vertical velocity estimate obtained here reflects the equatorial current system during the two-month April – May 2016 time period. The trade winds are at a seasonal minimum during spring, and spring 2016 coincided with the end of the strong 2015 – 2016 El Niño, so this time period may not be representative of a long-term average. A model analysis would also provide insight into the temporal variability of the subsurface GCP, which was not measured directly during ROGER. Model results could be validated through comparison with three years of glider observations along 93W.

Temporal variability of SST associated with the GCP could be compared to variability of the EUC from glider observations over 2013 – 2016. This would provide insight into the relationship between the strength and position of the EUC, and the distribution and magnitude of the GCP. A comparison of these metrics with a surface wind product would indicate the relationship between wind- and current-driven upwelling in maintaining the GCP.

A regional ocean model analysis could provide an estimate of the cross-track terms that were neglected in estimating EPV, in order to better understand the error associated with the glider EPV estimate. A simple equatorial channel model could be used to examine the temporal evolution of the EUC with respect to inertial and symmetric instabilities, and perhaps provide an explanation for the persistence of EPV with sign opposite to that of the Coriolis parameter over a three-year average. Lastly, the 1.5-layer model described in Chapter 3 should be expanded to a full 2-layer equatorial β-plane model to better capture the mechanisms that result in TIW propagation. This expanded model could be used to quantify the conditions that result in TIWs and the dependence of TIWs on the prescribed mean zonal flow.

Future work focuses on quantifying temporal variability and using model analyses to provide broader temporal and spatial context for the high-resolution glider results presented here. While this thesis provides insight into the path of the EUC around the Galápagos Archipelago and mechanisms behind the GCP on two-month and three-year averages, the equatorial current system is highly variable and has the ability to impact the GCP through a range of mechanisms that will be better understood with further study.

Bibliography

Bjerknes, J. (1969), Atmospheric Teleconnections from the Equatorial Pacific 1, *Monthly Weather Review*, *97*(3), 163–172.

Boyer, T. P., J. I. Antonov, O. K. Baranova, C. Coleman, H. E. Garcia, A. Grodsky, D. R. Johnson, R. A. Locarnini, A. V. Mishonov, T. D. O'Brien, C. R. Paver, J. R. Reagan, D. Seidov, I. V. Smolyar, and M. M. Zweng (2013), World Ocean Database 2013, NOAA Atlas NESDIS 72, S. Levitus, Ed., A. Mishonov.; Silver Spring, MD, 209 pp.

Carton, J. A., and B. S. Giese (2008), A Reanalysis of Ocean Climate Using Simple Ocean Data Assimilation (SODA), *Monthly Weather Review*, *136*(8), 2999–3017.

Charney, J. G. (1959), Non-linear theory of a wind-driven homogeneous layer near the equator, *Deep Sea Research (1953)*, *6*, 303–310.

Charney, J. G., and S. L. Spiegel (1971), Structure of Wind-Driven Equatorial Currents in Homogeneous Oceans, *Journal of Physical Oceanography*, *1*(3), 149–160.

Chelton, D. B., F. J. Wentz, C. L. Gentemann, R. A. de Szoeke, and M. G. Schlax (2000), Satellite microwave SST observations of transequatorial tropical instability waves, *Geophysical Research Letters*, *27*(9), 1239–1242.

Christensen, N. (1971), Observations of the Cromwell Current near the Galapagos Islands, *Deep-Sea Research and Oceanographic Abstracts*, *18*(1).

Cromwell, T., R. B. Montgomery, and E. D. Stroup (1954), Equatorial Undercurrent in Pacific Ocean Revealed by New Methods., *Science (New York, N.Y.)*, *119*(3097), 648–9.

Cushman-Roisin, B., and J.-M. Beckers (2011), *Introduction to geophysical fluid dynamics : physical and numerical aspects*, 2 ed., 828 pp., Academic Press.

Drenkard, E. J., and K. B. Karnauskas (2014), Strengthening of the Pacific Equatorial Undercurrent in the SODA Reanalysis: Mechanisms, Ocean Dynamics, and Implications, *Journal of Climate*, *27*(6), 2405–2416.

Düing, W., P. Hisard, E. Katz, J. Meincke, L. Miller, K. V. Moroshkin, G. Philander, A. A. Ribnikov, K. Voigt, and R. Weisberg (1975), Meanders and long waves in the equatorial Atlantic, *Nature*, *257*(5524), 280–284.

Dunkerton, T. J. (1981), On the Inertial Stability of the Equatorial Middle Atmosphere, *Journal of the Atmospheric Sciences*, *38*(11), 2354–2364.

Ertel, H. (1942), Ein neuer hydrodynamischer Erhaltungssatz, *Die Naturwissenschaften*, *30*(36), 543–544.

Farrar, J. T. (2008), Observations of the Dispersion Characteristics and Meridional Sea Level Structure of Equatorial Waves in the Pacific Ocean, *Journal of Physical Oceanography*, *38*(8), 1669–1689.

Farrar, J. T. (2011), Barotropic Rossby Waves Radiating from Tropical Instability Waves in the Pacific Ocean, *Journal of Physical Oceanography*, *41*(6), 1160–1181.

Farrar, J. T., and R. A. Weller (2006), Intraseasonal variability near 10°N in the eastern tropical Pacific Ocean, *Journal of Geophysical Research*, *111*(C5), C05,015.

Fiedler, P. C., and L. D. Talley (2006), Hydrography of the eastern tropical Pacific: A review, *Progress in Oceanography*, *69*(2-4), 143–180.

Firing, E., R. Lukas, J. Sadler, and K. Wyrtki (1983), Equatorial Undercurrent Disappears During 1982-1983 El Niño, *Science*, *222*(4628), 1121–1123.

Fofonoff, N. P., and R. B. Montgomery (1955), The Equatorial Undercurrent in the Light of the Vorticity Equation, *Tellus*, *7*(4), 518–521.

Gasparin, F., D. Roemmich, J. Gilson, and B. Cornuelle (2015), Assessment of the Upper-Ocean Observing System in the Equatorial Pacific: The Role of Argo in Resolving Intraseasonal to Interannual Variability*, *Journal of Atmospheric and Oceanic Technology*, *32*(9), 1668–1688.

Gill, A. E. (1982), *Atmosphere-Ocean Dynamics*, Academic Press.

Gouriou, Y., and J. Toole (1993), Mean circulation of the upper layers of the western equatorial Pacific Ocean, *Journal of Geophysical Research*, *98*(C12), 22,495.

Gula, J., M. J. Molemaker, and J. C. McWilliams (2015), Gulf Stream Dynamics along the Southeastern U.S. Seaboard, *Journal of Physical Oceanography*, *45*(3), 690–715.

Haine, T. W. N., and J. Marshall (1998), Gravitational, Symmetric, and Baroclinic Instability of the Ocean Mixed Layer, *Journal of Physical Oceanography*, *28*(4), 634–658.

Harvey, R. R., and W. C. Patzert (1976), Deep Current Measurements Suggest Long Waves in the Eastern Equatorial Pacific, *Science*, *193*(4256).

Hayes, S. P., L. J. Mangum, J. Picaut, A. Sumi, and K. Takeuchi (1991), TOGA-TAO: A Moored Array for Real-time Measurements in the Tropical Pacific Ocean, *Bulletin of the American Meteorological Society*, *72*(3), 339–347.

Helmholtz (1868), XLIII. On discontinuous movements of fluids, *The London, Edinburgh, and Dublin Philosophical Magazine and Journal of Science*, *36*(244), 337–346.

Houvenaghel, G. T. (1978), Oceanographic Conditions in the Galapagos Archipelago and Their Relationship with Life onthe Islands, in *Upwelling Ecosystems*, edited by R. Boje and M. Tomczak, pp. 181–200, Springer.

Jakoboski, J. K., R. E. Todd, W. B. Owens, K. B. Karnauskas, and D. L. Rudnick (2019), Bifurcation and Upwelling of the Equatorial Undercurrent West of the Galápagos Archipelago, *Submitted to Journal of Physical Oceanography*.

Johnson, E. S., and D. S. Luther (1994), Mean zonal momentum balance in the upper and central equatorial Pacific Ocean, *Journal of Geophysical Research*, *99*(C4), 7689.

Johnson, E. S., and J. A. Proehl (2004), Tropical Instability Wave Variability in the Pacific and Its Relation to Large-Scale Currents, *Journal of Physical Oceanography*, *34*(10), 2121–2147.

Johnson, G. C., and M. J. McPhaden (1999), Interior Pycnocline Flow from the Subtropical to the Equatorial Pacific Ocean*, *Journal of Physical Oceanography*, *29*(12), 3073–3089.

Johnson, G. C., M. J. McPhaden, G. D. Rowe, and K. E. McTaggart (2000), Upper equatorial Pacific Ocean current and salinity variability during the 1996-1998 El Niño-La Niña cycle, *Journal of Geophysical Research: Oceans*, *105*(C1), 1037–1053.

Johnson, G. C., M. J. McPhaden, and E. Firing (2001), Equatorial Pacific Ocean Horizontal Velocity, Divergence, and Upwelling, *Journal of Physical Oceanography*, *31*(3), 839–849.

Johnson, G. C., B. M. Sloyan, W. S. Kessler, and K. E. McTaggart (2002), Direct measurements of upper ocean currents and water properties across the tropical Pacific during the 1990s, *Progress in Oceanography*, *52*, 31–61.

Karnauskas, K. B., R. Murtugudde, and A. J. Busalacchi (2007), The Effect of the Galápagos Islands on the Equatorial Pacific Cold Tongue, *Journal of Physical Oceanography*, *37*(5), 1266–1281.

Karnauskas, K. B., R. Murtugudde, and A. J. Busalacchi (2008), The Effect of the Galápagos Islands on ENSO in Forced Ocean and Hybrid Coupled Models, *Journal of Physical Oceanography*, *38*(11), 2519–2534.

Karnauskas, K. B., R. Murtugudde, and A. J. Busalacchi (2010), Observing the Galápagos–EUC Interaction: Insights and Challenges, *Journal of Physical Oceanography*, *40*(12), 2768–2777.

Karnauskas, K. B., R. Murtugudde, and W. B. Owens (2014), Climate and the Global Reach of the Galápagos Archipelago, in *The Galápagos: A Natural Laboratory for the Earth Sciences*, chap. 11, pp. 215–231, John Wiley & Sons, Inc.

Karnauskas, K. B., S. Jenouvrier, C. W. Brown, and R. Murtugudde (2015), Strong sea surface cooling in the eastern equatorial Pacific and implications for Galapagos Penguin conservation, *Geophysical Research Letters*, *42*(15), 6432–6437.

Kelly, S. M. (2016), The Vertical Mode Decomposition of Surface and Internal Tides in the Presence of a Free Surface and Arbitrary Topography, *Journal of Physical Oceanography*, *46*(12), 3777–3788.

Kessler, W. S. (2006), The circulation of the eastern tropical Pacific: A review, *Progress in Oceanography*, *69*(2-4), 181–217.

Kessler, W. S., L. M. Rothstein, and D. Chen (1998), The Annual Cycle of SST in the Eastern Tropical Pacific, Diagnosed in an Ocean GCM, *Journal of Climate*, *11*(5), 777–799.

Knauss, J. A. (1959), Measurements of the Cromwell current, *Deep Sea Research*, *6*, 265–286.

Knauss, J. A. (1966), Further measurements and observations of the Cromwell Current, *Journal of Marine Research*, *24*(2), 205–240.

Knauss, J. A., and J. E. King (1958), Observations of the Pacific Equatorial Undercurrent, *Nature*, *182*, 601–602.

Kundu, P. K., I. M. Cohen, D. R. Dowling, and G. Tryggvason (2015), *Fluid mechanics*, 6 ed., 921 pp., Academic Press.

Lau, K. M., and S. Yang (2015), Tropical Meteorology and Climate | Walker Circulation, *Encyclopedia of Atmospheric Sciences*, pp. 177–181.

Lee, T., G. Lagerloef, M. M. Gierach, H.-Y. Kao, S. Yueh, and K. Dohan (2012), Aquarius reveals salinity structure of tropical instability waves, *Geophysical Research Letters*, *39*(12).

Legeckis, R. (1977), Long Waves in the Eastern Equatorial Pacific Ocean: A View from a Geostationary Satellite, *Science*, *197*(4309).

Leslie, W. R., and K. B. Karnauskas (2014), The Equatorial Undercurrent and TAO Sampling Bias from a Decade at SEA, *Journal of Atmospheric and Oceanic Technology*, *31*(9), 2015–2025.

Liu, Y., L. Xie, J. M. Morrison, D. Kamykowski, and W. V. Sweet (2014), Ocean Circulation and Water Mass Characteristics around the Galápagos Archipelago Simulated by a Multiscale Nested Ocean Circulation Model, *International Journal of Oceanography*, *2014*, 1–16.

Lukas, R. (1986), The termination of the Equatorial Undercurrent in the eastern Pacific, *Progress in Oceanography*, *16*(2), 63–90.

Lukas, R., and E. Firing (1984), The geostrophic balance of the Pacific Equatorial Undercurrent, *Deep Sea Research Part A, Oceanographic Research Papers*, *31*(1), 61–66.

Lyman, J. M., D. B. Chelton, R. A. DeSzoeke, and R. M. Samelson (2005), Tropical Instability Waves as a Resonance between Equatorial Rossby Waves, *Journal of Physical Oceanography*, *35*(2), 232–254.

Lyman, J. M., G. C. Johnson, and W. S. Kessler (2007), Distinct 17- and 33-Day Tropical Instability Waves in Subsurface Observations, *Journal of Physical Oceanography*, *37*(4), 855–872.

Matsuno, T. (1966), Quasi-geostrophic motions in the equatorial area, *Journal of the Meteorological Society of Japan*, *44*(February), 25–43.

McCreary, J., and P. Lu (1994), Interaction between the Subtropical and Equatorial Ocean Circulations: The Subtropical Cell, *Journal of Physical Oceanography*, *24*(2), 466–497.

McPhaden, M. J. (1996), Monthly period oscillations in the Pacific North Equatorial Countercurrent, *Journal of Geophysical Research*, *101*(C3), 6337.

McPhaden, M. J., J. A. Proehl, and L. M. Rothstein (1987), On the Structure of Low-Frequency Equatorial Waves, *Journal of Physical Oceanography*, *17*(9), 1555–1559.

Molemaker, M. J., J. C. McWilliams, and W. K. Dewar (2015), Submesoscale Instability and Generation of Mesoscale Anticyclones near a Separation of the California Undercurrent, *Journal of Physical Oceanography*, *45*(3), 613–629.

Mooers, C. N. K. (1975), Several effects of a baroclinic current on the cross-stream propagation of inertial-internal waves, *Geophysical Fluid Dynamics*, *6*(3), 245–275.

National Centers for Environmental Information (2016), Documentation for The Group for High Resolution Sea Surface Temperature (GHRSST) data archived at NCEI (NCEI Accession 0123222). Version 2.2.

Palacios, D. M. (2004), Seasonal patterns of sea-surface temperature and ocean color around the Galápagos: Regional and local influences, *Deep-Sea Research Part II: Topical Studies in Oceanography*, *51*(1-3), 43–57.

Pedlosky, J. (1987a), An Inertial Theory of the Equatorial Undercurrent, *Journal of Physical Oceanography*, *17*(11), 1978–1985.

Pedlosky, J. (1987b), Instability Theory, in *Geophysical Fluid Dynamics*, pp. 490–623, Springer New York, New York, NY.

Pedlosky, J. (1987c), Ageostrophic Motion, in *Geophysical Fluid Dynamics*, pp. 624–688, Springer New York, New York, NY.

Perez, R. C., and W. S. Kessler (2009), Three-Dimensional Structure of Tropical Cells in the Central Equatorial Pacific Ocean, *Journal of Physical Oceanography*, *39*(1), 27–49.

Périgaud, C. (1990), Sea level oscillations observed with Geosat along the two shear fronts of the Pacific North Equatorial Countercurrent, *Journal of Geophysical Research*, *95*(C5), 7239.

Philander, S. G. H. (1973), Equatorial Undercurrent: Measurements and Theories, *Reviews of Geophysics*, *11*(3), 513.

Philander, S. G. H. (1976), Instabilities of zonal equatorial currents, *Journal of Geophysical Research*, *81*(21), 3725–3735.

Philander, S. G. H. (1978), Instabilities of zonal equatorial currents, 2, *Journal of Geophysical Research*, *83*(C7), 3679.

Proehl, J. A. (1998), The role of meridional flow asymmetry in the dynamics of tropical instability, *Journal of Geophysical Research: Oceans*, *103*(C11), 24,597–24,618.

Qiao, L., and R. H. Weisberg (1995), Tropical instability wave kinematics: Observations from the Tropical Instability Wave Experiment, *Journal of Geophysical Research*, *100*(C5), 8677.

Qiao, L., and R. H. Weisberg (1996), The Zonal Momentum Balance of the Equatorial Undercurrent in the Central Pacific, *Journal of Physical Oceanography*, *27*, 1094–1119.

Reynolds, R. W., T. M. Smith, C. Liu, D. B. Chelton, K. S. Casey, and M. G. Schlax (2007), Daily High-Resolution-Blended Analyses for Sea Surface Temperature, *Journal of Climate*, *20*(22), 5473–5496.

Riser, S. C., H. J. Freeland, D. Roemmich, S. Wijffels, A. Troisi, M. Belbeoch, D. Gilbert, J. Xu, S. Pouliquen, A. Thresher, P.-Y. Le Traon, G. Maze, B. Klein, M. Ravichandran, F. Grant, P.-M. Poulain, T. Suga, B. Lim, A. Sterl, P. Sutton, K.-A. Mork, P. J. Velez-Belchi, I. Ansorge, B. King, J. Turton, M. Baringer, and S. R. Jayne (2016), Fifteen years of ocean observations with the global Argo array, *Nature Clim. Change*, *6*(2), 145–153.

Roemmich, D., and J. Gilson (2009), The 2004-2008 mean and annual cycle of temperature, salinity, and steric height in the global ocean from the Argo Program, *Progress in Oceanography*, *82*(2), 81–100.

Roundy, P. E., and G. N. Kiladis (2006), Observed Relationships between Oceanic Kelvin Waves and Atmospheric Forcing, *Journal of Climate*, *19*(20), 5253–5272.

Rudnick, D. L., and S. T. Cole (2011), On sampling the ocean using underwater gliders, *Journal of Geophysical Research*, *116*(C8), C08,010.

Rudnick, D. L., R. E. Davis, and J. T. Sherman (2016), Spray underwater glider operations, *Journal of Atmospheric and Oceanic Technology*, *33*(6), 1113–1122.

Rudnick, D. L., K. D. Zaba, R. E. Todd, and R. E. Davis (2017), A climatology of the California Current System from a network of underwater gliders, *Progress in Oceanography*, *154*, 64–106.

Rudnick, D. L., J. T. Sherman, and A. P. Wu (2018), Depth-average velocity from Spray underwater gliders, *Journal of Atmospheric and Oceanic Technology*, *35*, 1665–1673.

Schubert, W., E. Ruprecht, R. Hertenstein, R. N. Ferreira, R. Taft, C. Rozoff, P. Ciesielski, and H.-C. Kuo (2004), English translations of twenty-one of Ertel's papers on geophysical fluid dynamics, *Meteorologische Zeitschrift*, *13*(6), 527–576.

Sherman, J., R. E. Davis, W. B. Owens, and J. Valdes (2001), The autonomous underwater glider, *Oceanic Engineering, IEEE Journal of*, *26*(4), 437–446.

Smyth, W. D., J. N. Moum, L. Li, and S. A. Thorpe (2013), Diurnal Shear Instability, the Descent of the Surface Shear Layer, and the Deep Cycle of Equatorial Turbulence, *Journal of Physical Oceanography*, *43*(11), 2432–2455.

Stevens, D. E. (1983), On Symmetric Stability and Instability of Zonal Mean Flows Near the Equator, *Journal of the Atmospheric Sciences*, *40*(4), 882–893.

Sweet, W. V., J. M. Morrison, D. Kamykowski, B. A. Schaeffer, S. Banks, and A. McCulloch (2007), Water mass seasonal variability in the Galápagos Archipelago, *Deep Sea Research Part I: Oceanographic Research Papers*, *54*(12), 2023–2035.

Thomas, L. N., J. R. Taylor, R. Ferrari, and T. M. Joyce (2013), Symmetric instability in the Gulf Stream, *Deep Sea Research Part II: Topical Studies in Oceanography*, *91*, 96–110.

Thomson, W. (1871), XLVI. Hydrokinetic solutions and observations, *The London, Edinburgh, and Dublin Philosophical Magazine and Journal of Science*, *42*(281), 362–377.

Thyng, K., C. Greene, R. Hetland, H. Zimmerle, and S. DiMarco (2016), True Colors of Oceanography: Guidelines for Effective and Accurate Colormap Selection, *Oceanography*, *29*(3), 9–13.

Todd, R. E., D. L. Rudnick, J. Sherman, W. B. Owens, and L. George (2017), Absolute velocity estimates from autonomous underwater gliders equipped with Doppler current profilers, *Journal of Atmospheric and Oceanic Technology*, *34*, 309–333.

Visbeck, M. (2002), Deep Velocity Profiling Using Lowered Acoustic Doppler Current Profilers: Bottom Track and Inverse Solutions, *Journal of Atmospheric and Oceanic Technology*, *19*(5), 794–807.

Weisberg, R. H., and L. Qiao (2000), Equatorial Upwelling in the Central Pacific Estimated from Moored Velocity Profilers, *Journal of Physical Oceanography*, *30*, 105–124.

Wunsch, C., and A. E. Gill (1976), Observations of equatorially trapped waves in Pacific sea level variations, *Deep Sea Research and Oceanographic Abstracts*, *23*(5), 371–390.

Wyrtki, K. (1966), Oceanography of the eastern equatorial Pacific Ocean, *Oceanography and Marine Biology Annual Review 4*, pp. 33–68.

Wyrtki, K. (1974), Equatorial Currents in the Pacific 1950 to 1970 and Their Relations to the Trade Winds, *Journal of Physical Oceanography*, *4*(3), 372–380.

Wyrtki, K. (1981), An Estimate of Equatorial Upwelling in the Pacific, *Journal of Physical Oceanography*, *11*(9), 1205–1214.

Wyrtki, K., and B. Kilonsky (1984), Mean Water and Current Structure during the Hawaii-to-Tahiti Shuttle Experiment, *Journal of Physical Oceanography*, *14*(2), 242–254.

Wyrtki, K., and G. Meyers (1977), Variability of the thermal structure in the central equatorial Pacific Ocean, *Tech. rep.*, University of Hawaii.

Yu, J.-Y., and T. W. Liu (2003), A linear relationship between ENSO intensity and tropical instability wave activity in the eastern Pacific Ocean, *Geophysical Research Letters*, *30*(14), 1735.

Yu, Z., J. P. McCreary, and J. A. Proehl (1995), Meridional Asymmetry and Energetics of Tropical Instability Waves, *Journal of Physical Oceanography*, *25*(12), 2997–3007.

Yu, Z., P. S. Schopf, and J. P. McCreary (1997), On the Annual Cycle of Upper-Ocean Circulation in the Eastern Equatorial Pacific, *Journal of Physical Oceanography*, *27*(2), 309–324.